

**INVESTIGATION OF THE FORMATION OF  
 $\text{La}_{1-x}\text{Sr}_x\text{Co}_{1-y}\text{Fe}_y\text{O}_{3-d}$  CATHODE MATERIALS AND  
THEIR INTERACTION WITH ELECTROLYTE  
SUBSTRATES FOR POTENTIAL IT-SOFC  
APPLICATIONS**

**A Thesis Submitted to  
the Graduate School of Engineering and Sciences of  
İzmir Institute of Technology  
in Partial Fulfillment of the Requirements for the Degree of**

**MASTER OF SCIENCE**

**in Mechanical Engineering**

**by  
Can SINDIRAÇ**

**July 2013  
İZMİR**

We approve the thesis of **Can SINDIRAÇ**

**Examining Committee Members:**

---

**Prof. Dr. Sedat AKKURT**

Department of Mechanical Engineering, İzmir Institute of Technology

---

**Prof. Dr. Muhsin ÇİFTÇİOĞLU**

Department of Chemical Engineering, İzmir Institute of Technology

---

**Assist. Prof. Dr. Engin ÖZÇİVİCİ**

Department of Mechanical Engineering, İzmir Institute of Technology

**8 July 2013**

---

**Prof. Dr. Sedat AKKURT**

Supervisor, Department of Mechanical Engineering  
İzmir Institute of Technology

---

**Prof. Dr. Metin TANOĞLU**

Head of the Department of  
Mechanical Engineering

---

**Prof. Dr. R. Tuğrul SENGER**

Dean of the Graduate School of  
Engineering and Sciences

## **ACKNOWLEDGEMENTS**

First and foremost, I would like to thank and express my deepest gratitude to Prof. Dr. Sedat AKKURT for all of his advises, motivation, support and encouragement through thesis. Without his effort and all advises, this study would not have been successful. But above all I am thankful to his advises for life, I have been fortunate to have Prof. AKKURT as my advisor and I should admit that he is much more than a supervisor for me and it is an honor to work with him.

I would like to express my special thanks to Meral KARACA, Ezel BOYACI and Sinem BEZİRCİLİOĞLU for all their help and their support to improve my thesis, despite their busy time table. Their help were unforgettable for me.

Furthermore I would also like to acknowledge with much appreciation the crucial role of the staff of İYTE MAM, especially Sinem HORTOOĞLU, Gökhan ERDOĞAN, Duygu OĞUZ KILIÇ and Canan GÜNEY.

My thanks and appreciations also go to my colleagues and my friends all over the world who send me their best wishes always for my thesis. Especially, I am thankful to Gözde ÇINAR for her unforgettable helps and supports to me.

Finally, I wish to thank my beloved parents, Özhan SINDIRAÇ and Fatma Filiz SINDIRAÇ for their support and encouragement throughout my whole life. Without their everlasting support, I would never be as I am.

## ABSTRACT

### INVESTIGATION OF THE FORMATION OF $\text{La}_{1-x}\text{Sr}_x\text{Co}_{1-y}\text{Fe}_y\text{O}_{3-d}$ CATHODE MATERIALS AND THEIR INTERACTION WITH ELECTROLYTE SUBSTRATES FOR POTENTIAL IT-SOFC APPLICATIONS

Cathode layers of IT-SOFC (Intermediate Temperature Solid Oxide Fuel Cell) materials are investigated to find out the reactions leading to the formation of  $\text{La}_{0.6}\text{Sr}_{0.4}\text{Co}_{0.8}\text{Fe}_{0.2}\text{O}_3$  and  $\text{La}_{0.6}\text{Sr}_{0.4}\text{Co}_{0.2}\text{Fe}_{0.8}\text{O}_3$  on the surface of either  $\text{ZrO}_2$  or CGO (Cerium-Gadolinium Oxide) electrolyte substrates. Precursor salt powders were blended, compressed and placed on discs of sintered ceramic electrolytes before being heated in a laboratory furnace at  $800^\circ\text{C}$  for 1h. Almost all combinations of LSCF salt mixtures were prepared and analyzed by SEM-EDS, XRD and DTA-TGA to see if all solid state reactions are completed and what new phases eventually formed in LSCF combinations. Most of the transformation was complete after  $1050^\circ\text{C}$  heat treatment to yield oxides. According to XRD analysis it was observed that La plays a significant role to enable the formation of new phases. In the absence of La, other salts had significant difficulty to react to form new phases. Also, Sr tends to swap its chloride with nitrate of other salts in salt mixtures after drying in oven. SEM-EDS analysis of the interface between the electrolyte and LSCF showed that there was weak mutual diffusion of the constituent elements between the cathode layer and the electrolyte. The cathode layer was usually in porous form but was found to spread well over the substrate. Uneven diffusion of La, Sr, Co or Fe into the substrate had little influence on the stoichiometry of the resulting coating layer. Unlike 6428 samples, it was possible to form stoichiometric LSCF in 6482 samples.

## ÖZET

### La<sub>1-x</sub>Sr<sub>x</sub>Co<sub>1-y</sub>Fe<sub>y</sub>O<sub>3-d</sub> KATOT MALZEMELERİNİN OLUŞUMU VE ELEKTROLİT ALTLIKLARLA POTENSİYEL ETKİLEŞİMİNİN IT-SOFC UYGULAMALARI İÇİN İNCELENMESİ

Bu çalışma, Orta Sıcaklık Katı Oksit Yakıt Hücrelerinde (IT-SOFC) katot malzemesi olarak kullanılan La<sub>0.6</sub>Sr<sub>0.4</sub>Co<sub>0.8</sub>Fe<sub>0.2</sub>O<sub>3</sub> ve La<sub>0.6</sub>Sr<sub>0.4</sub>Co<sub>0.2</sub>Fe<sub>0.8</sub>O<sub>3</sub>'nin oluşumunu sağlayan reaksiyonlar ve bu karışımların ZrO<sub>2</sub> ve CGO elektrolit altlıklarla olan ilişkileri incelenmiştir. Öncül tuzlar ezilerek karıştırılıp disk şeklinde pellet haline getirildikten sonra önceden sinterlenmiş seramik altığın üzerine konuldu ve ikisi 800°C'de 1 saat fırında birlikte ısıtılarak ısıl işlem uygulanıldı. Katı hal reaksiyonlarının tamamlandığında oluşan malzemeleri görmek amacıyla, LSCF malzemesini oluşturabilecek hemen hemen tüm kombinasyonlar oluşturulup bu örnekler SEM-EDS, XRD ve TGA-DTA analizleriyle incelendi ve 1050°C derecedeki ısıl işlemde sonra faz değişimlerinin çoğunun bittiği görüldü. XRD analizlerine göre, La elementi, diğer tuzların reaksiyona girmelerini önemli bir şekilde tetiklemekte ve eksikliğinde birbirleriyle reaksiyonlarının oldukça azaldığı görülmüştür. Ayrıca Sr tuzunun 55°C'de kuruduktan sonra diğer tozlarla karışıma girdiği zaman klorürünü verirken diğer tuzlardan nitrat aldığı gözlemlenmiştir. SEM ve EDS analizleri göstermiştir ki, hem elektrolit altlıktan katota hem de katottan elektrolite arayüzeyden karşılıklı zayıf bir difüzyon gerçekleşmektedir. Katot katmanı genellikle gözenekli yapıda olup çoğunlukla elektroliti tamamen kapladı. La, Sr, Co ve Fe elementlerinin katot malzemesinin oluştururken ısıl işlem sırasında elektrolit tabakasına difuze olmaları sonucunda arzu edilen LSCF oranlarında bozulmalar olmuştur. Tüm bu deneylerin sonucunda La<sub>0.6</sub>Sr<sub>0.4</sub>Co<sub>0.8</sub>Fe<sub>0.2</sub>O<sub>3</sub>'nin oluşumu tam istenilen oranda sağlanırken, La<sub>0.6</sub>Sr<sub>0.4</sub>Co<sub>0.2</sub>Fe<sub>0.8</sub>O<sub>3</sub>'nin oluşumunda istenilen oran tam olarak sağlanamamıştır.

# TABLE OF CONTENTS

LIST OF FIGURES .....	ix
LIST OF TABLES .....	xiv
CHAPTER 1. INTRODUCTION .....	1
CHAPTER 2. LITERATURE SEARCH.....	4
2.1. Fuel Cells .....	4
2.2. Fuel Cell Types .....	7
2.2.1. Solid Oxide Fuel Cells (SOFC) .....	8
2.2.1.1 Stack Design .....	11
2.2.1.2 Electrolytes .....	11
2.2.1.3 Cathodes.....	13
2.2.1.4. Anodes .....	14
2.2.1.5. Interconnect .....	15
2.3. Synthesis Methods for Cathode Layer Materials.....	15
2.3.1. Solid State Method.....	15
2.3.2. The Combustion Method .....	16
2.3.3. Pechini Method .....	16
2.3.4. Spray-Drying Method .....	17
2.3.5. ESD Method .....	17
2.4. Thermal Decomposition Reactions of LSCF precursor Salts.....	18
CHAPTER 3. EXPERIMENTAL.....	20
3.1. Materials and Equipments Used in the Experiments .....	20
3.1.1. Precursor Salt Powders for Cathode .....	20
3.1.2. Powders Used in the Preparation of the Electrolyte Substrate .....	21
3.2. Experimental Plan.....	21
3.2.1. Preparation of the Substrate .....	23
3.2.2. Preparation of the Cathode .....	25
3.2.3. Solid-State Reaction Process .....	28

3.3. Characterization .....	29
3.3.1. Scanning Electron Microscopy .....	29
3.3.2. X-Ray Diffraction Analysis .....	29
3.3.3. Differential Thermal Analysis (DTA/ TGA) .....	29
 CHAPTER 4. RESULTS AND DISCUSSION.....	 31
4.1. SEM Analyses.....	31
4.1.1 SEM Analyses of As-Received Precursor Salts .....	31
4.1.2. Diffusion Couple Heating Experiments.....	33
4.1.2.1. SEM and EDS Analysis of Heated TZ-3Y Electrolyte- Cathode Pair Samples .....	34
4.1.2.2. SEM and EDS Analysis of Heated CGO Electrolyte-Cathode Pair Samples .....	41
4.2. X-Ray Diffraction Analysis .....	50
4.2.1. XRD Analysis of As-Received Precursor Salts .....	50
4.2.2. XRD Analysis of Mixture of Precursor Salts XRD charts of as-synthesized mixtures were obtained from samples that were dried at 55 <sup>0</sup> C in an oven. The profiles presented characteristic peaks of the salts compounds as expected. ....	52
4.2.3. XRD Analysis of Heated Precursor Salt Mixtures XRD charts of as-synthesized mixtures that were heated in a furnace via a heating schedule as shown in Figure 3.6 are given in this section. ....	57
4.3. Thermal Characterization of Precursors Salts .....	64
4.3.1. Thermal Characterization of As-Received Precursors Salts.....	64
4.3.2. Thermal Characterization of As-Synthesized Precursors Salts ...	69
4.4. General Interpretation and Discussion.....	74
 CHAPTER 5.CONCLUSION .....	 76
 REFERENCES .....	 78
 APPENDICES	
APPENDIX A. SEM-EDS RESULTS OF MIXTURES HEATED ON TOP OF	

ZIRCONIA SUBSTRATE .....	83
APPENDIX B. SEM-EDS RESULTS OF MIXTURES HEATED ON TOP OF CGO SUBSTRATE .....	88

# LIST OF FIGURES

<u>Figure</u>	<u>Page</u>
Figure 1.1. A typical schematic picture of an SOFC .....	1
Figure 2.1. Sketch of William Grove's 1839 fuel cell [20].....	5
Figure 2.2. Schematic picture of a fuel cell .....	5
Figure 2.3. Comparison of emissions of internal combustion engine and fuel cell.....	6
vehicles . .....	6
Figure 2.4. Classification of fuel cells .....	7
Figure 2.5. Schematic picture of an SOFC .....	8
Figure 2.6. Schematic diagram of reactions in SOFCs based on oxygen-ion conductors .....	9
Figure 2.7 Schematic representation of structure of perovskite (ABO <sub>3</sub> ).....	10
Figure 2.8. Configuration for a tubular design SOFC .....	11
Figure 2.9. Vacancy transport in YSZ .....	12
Figure 2.10. Reduction reaction on the surface of a cathode made of LSM-YSZ.....	13
Figure 2.11. Oxidation reaction on the surface of an anode made of Ni-YSZ [35] .....	15
Figure 2.12. Schematic drawing of the ESD setup [12] .....	18
Figure 3.1. Particle size distribution of TZ-3Y.....	21
Figure 3.2. Flowchart of the experimental work followed in this thesis. ....	23
Figure 3.3. CGO Samples of pressed ceramic electrolyte discs: (a) before and (b) after sintering. TZ-3Y pellets which pressed for using as ceramic electrolyte discs: (c) before and (d) after sintering. ....	24
Figure 3.4. Devices used in experiments for making CGO and TZ-3Y pellets: (a) Agate Mortar, (b) Hydraulic manual pres (Yıldız Hidrolik Pres, X5), (c) Stainless steel die with $\Phi=25$ mm diameter , (d) Stainless steel die with $\Phi=15$ mm diameter, (e) Box furnace used for heat treatment (Nabertherm), (f) Polishing machine Presi, Mecapol P230.....	25
Figure 3.5. Samples of pressed discs before sintering process (5) L+C , (6) S+C , (7) F+C , (8) L+F , (9) S+F , (10) LSCF , (11) L+S+C , (12) L+S , (13) L+S+F, (14) L+F+C , (15) S+F+C, (16) L <sub>6</sub> S <sub>4</sub> C <sub>8</sub> F <sub>2</sub> , (17) L <sub>6</sub> S <sub>4</sub> C <sub>2</sub> F <sub>8</sub> . ....	27
Figure 3.6. Heating schedule for LSCF precursors. ....	28
Figure 3.7. Devices used in the experiments (a) Hot mounting press (b) Low speed diamond saw used for cutting samples (c) Polishing machine .....	28
Figure 4.1. SEM image of as-received precursor salt (La(NO <sub>3</sub> ) <sub>3</sub> .6H <sub>2</sub> O) at different magnifications.....	32

Figure 4.2. SEM image of as-received precursor salt ( $\text{SrCl}_2 \cdot 6\text{H}_2\text{O}$ ) at different magnifications.....	32
Figure 4.3. SEM image of third as-received precursor salt ( $\text{Co}(\text{NO}_3)_2 \cdot 6\text{H}_2\text{O}$ ) at different magnifications.....	32
Figure 4.4. SEM image of fourth as-received precursor salt ( $\text{Fe}(\text{NO}_3)_3 \cdot 9\text{H}_2\text{O}$ ) at different magnifications.....	33
Figure 4.5. SEM image of the interface between $\text{La}(\text{NO}_3)_3 \cdot 6\text{H}_2\text{O} + \text{SrCl}_2 \cdot 6\text{H}_2\text{O} + \text{Co}(\text{NO}_3)_2 \cdot 6\text{H}_2\text{O} + \text{Fe}(\text{NO}_3)_3 \cdot 9\text{H}_2\text{O}$ mixture and zirconia pellets after heat treatment. ....	36
Figure 4.6. Mapping analysis of the interface between $\text{La}(\text{NO}_3)_3 \cdot 6\text{H}_2\text{O} + \text{SrCl}_2 \cdot 6\text{H}_2\text{O} + \text{Co}(\text{NO}_3)_2 \cdot 6\text{H}_2\text{O} + \text{Fe}(\text{NO}_3)_3 \cdot 9\text{H}_2\text{O}$ mixture and zirconia pellets after heat treatment. ....	36
Figure 4.7. SEM image of the interface between $\text{La}(\text{NO}_3)_3 \cdot 6\text{H}_2\text{O} + \text{SrCl}_2 \cdot 6\text{H}_2\text{O} + \text{Co}(\text{NO}_3)_2 \cdot 6\text{H}_2\text{O}$ mixture and zirconia pellets after heat treatment. ....	37
Figure 4.8. Mapping analysis of the interface between $\text{La}(\text{NO}_3)_3 \cdot 6\text{H}_2\text{O} + \text{SrCl}_2 \cdot 6\text{H}_2\text{O} + \text{Co}(\text{NO}_3)_2 \cdot 6\text{H}_2\text{O}$ mixture and zirconia pellets after heat treatment. ....	37
Figure 4.9. SEM image of the interface between $\text{La}(\text{NO}_3)_3 \cdot 6\text{H}_2\text{O} + \text{Co}(\text{NO}_3)_2 \cdot 6\text{H}_2\text{O} + \text{Fe}(\text{NO}_3)_3 \cdot 9\text{H}_2\text{O}$ mixture and Zirconia pellets after heat treatment. ....	38
Figure 4.10. Mapping analysis of the interface between $\text{La}(\text{NO}_3)_3 \cdot 6\text{H}_2\text{O} + \text{Co}(\text{NO}_3)_2 \cdot 6\text{H}_2\text{O} + \text{Fe}(\text{NO}_3)_3 \cdot 9\text{H}_2\text{O}$ mixture and Zirconia pellets after heat treatment. ....	38
Figure 4.11. SEM image of the interface between $\text{SrCl}_2 \cdot 6\text{H}_2\text{O} + \text{Co}(\text{NO}_3)_2 \cdot 6\text{H}_2\text{O} + \text{Fe}(\text{NO}_3)_3 \cdot 9\text{H}_2\text{O}$ mixture and zirconia pellets after heat treatment.....	38
Figure 4.12. Mapping analysis of the interface between $\text{SrCl}_2 \cdot 6\text{H}_2\text{O} + \text{Co}(\text{NO}_3)_2 \cdot 6\text{H}_2\text{O} + \text{Fe}(\text{NO}_3)_3 \cdot 9\text{H}_2\text{O}$ mixture and zirconia pellets after heat treatment.....	39
Figure 4.13. SEM image of the interface between $\text{La}_{0.6}\text{Sr}_{0.4}\text{Co}_{0.8}\text{Fe}_{0.2}\text{O}_3$ mixture and zirconia pellets after heat treatment. ....	39
Figure 4.14. Mapping analysis of the interface between $\text{La}_{0.6}\text{Sr}_{0.4}\text{Co}_{0.8}\text{Fe}_{0.2}\text{O}_3$ mixture and zirconia pellets after heat treatment. ....	40
Figure 4.15. SEM image of the interface between $\text{La}_{0.6}\text{Sr}_{0.4}\text{Co}_{0.2}\text{Fe}_{0.8}\text{O}_3$ mixture and zirconia pellets after heat treatment. ....	40
Figure 4.16. Mapping analysis of the interface between $\text{La}_{0.6}\text{Sr}_{0.4}\text{Co}_{0.2}\text{Fe}_{0.8}\text{O}_3$ mixture and zirconia pellets after heat treatment.....	41
Figure 4.17. SEM image of the interface between $\text{La}(\text{NO}_3)_3 \cdot 6\text{H}_2\text{O} + \text{SrCl}_2 \cdot 6\text{H}_2\text{O} + \text{Co}(\text{NO}_3)_2 \cdot 6\text{H}_2\text{O} + \text{Fe}(\text{NO}_3)_3 \cdot 9\text{H}_2\text{O}$ mixture and CGO pellets after	

heat treatment.....	43
Figure 4.18. Mapping analysis of the interface between $\text{La}(\text{NO}_3)_3 \cdot 6\text{H}_2\text{O}$ + $\text{SrCl}_2 \cdot 6\text{H}_2\text{O}$ + $\text{Co}(\text{NO}_3)_2 \cdot 6\text{H}_2\text{O}$ + $\text{Fe}(\text{NO}_3)_3 \cdot 9\text{H}_2\text{O}$ mixture and CGO pellets after heat treatment. ....	44
Figure 4.19. SEM image of the interface between $\text{La}(\text{NO}_3)_3 \cdot 6\text{H}_2\text{O}$ + $\text{SrCl}_2 \cdot 6\text{H}_2\text{O}$ + $\text{Co}(\text{NO}_3)_2 \cdot 6\text{H}_2\text{O}$ mixture and CGO pellets after heat treatment. ....	44
Figure 4.20. Mapping analysis of the interface between $\text{La}(\text{NO}_3)_3 \cdot 6\text{H}_2\text{O}$ + $\text{SrCl}_2 \cdot 6\text{H}_2\text{O}$ + $\text{Co}(\text{NO}_3)_2 \cdot 6\text{H}_2\text{O}$ mixture and CGO pellets after heat treatment. ....	45
Figure 4.21. SEM image of the interface between $\text{La}(\text{NO}_3)_3 \cdot 6\text{H}_2\text{O}$ + $\text{Co}(\text{NO}_3)_2 \cdot 6\text{H}_2\text{O}$ + $\text{Fe}(\text{NO}_3)_3 \cdot 9\text{H}_2\text{O}$ mixture and CGO pellets after heat treatment. ....	45
Figure 4.22. Mapping analysis of the interface between $\text{La}(\text{NO}_3)_3 \cdot 6\text{H}_2\text{O}$ + $\text{Co}(\text{NO}_3)_2 \cdot 6\text{H}_2\text{O}$ + $\text{Fe}(\text{NO}_3)_3 \cdot 9\text{H}_2\text{O}$ mixture and CGO pellets after heat treatment.....	46
Figure 4.23. SEM image of the interface between $\text{La}(\text{NO}_3)_3 \cdot 6\text{H}_2\text{O}$ + $\text{SrCl}_2 \cdot 6\text{H}_2\text{O}$ mixture and CGO pellets after heat treatment. ....	46
Figure 4.24. Mapping analysis of interface between $\text{La}(\text{NO}_3)_3 \cdot 6\text{H}_2\text{O}$ + $\text{SrCl}_2 \cdot 6\text{H}_2\text{O}$ mixture and CGO pellets after heat treatment. ....	47
Figure 4.25. SEM image of the interface between $\text{La}(\text{NO}_3)_3 \cdot 6\text{H}_2\text{O}$ + $\text{SrCl}_2 \cdot 6\text{H}_2\text{O}$ + $\text{Fe}(\text{NO}_3)_2 \cdot 9\text{H}_2\text{O}$ mixture and CGO pellets after heat treatment. ....	47
Figure 4.26. Mapping analysis of interface between $\text{La}(\text{NO}_3)_3 \cdot 6\text{H}_2\text{O}$ + $\text{SrCl}_2 \cdot 6\text{H}_2\text{O}$ + $\text{Fe}(\text{NO}_3)_2 \cdot 9\text{H}_2\text{O}$ mixture and CGO pellets after heat treatment. ....	48
Figure 4.27. SEM image of the interface between $\text{La}_{0.6}\text{Sr}_{0.4}\text{Co}_{0.8}\text{Fe}_{0.2}\text{O}_3$ mixture and CGO pellets after heat treatment.....	48
Figure 4.28. Mapping analysis of the interface between $\text{La}_{0.6}\text{Sr}_{0.4}\text{Co}_{0.8}\text{Fe}_{0.2}\text{O}_3$ mixture and CGO pellets after heat treatment. ....	49
Figure 4.29. SEM image of the interface between $\text{La}_{0.6}\text{Sr}_{0.4}\text{Co}_{0.2}\text{Fe}_{0.8}\text{O}_3$ mixture and CGO pellets after heat treatment.....	49
Figure 4.30. Mapping analysis of the interface between $\text{La}_{0.6}\text{Sr}_{0.4}\text{Co}_{0.2}\text{Fe}_{0.8}\text{O}_3$ mixture and CGO pellets after heat treatment.....	50
Figure 4.31. XRD chart for $\text{La}(\text{NO}_3)_3 \cdot 6\text{H}_2\text{O}$ .....	51
Figure 4.32. XRD chart for $\text{SrCl}_2 \cdot 6\text{H}_2\text{O}$ .....	51
Figure 4.33. XRD chart for $\text{Co}(\text{NO}_3)_2 \cdot 6\text{H}_2\text{O}$ .....	51
Figure 4.34. XRD chart for $\text{Fe}(\text{NO}_3)_3 \cdot 9\text{H}_2\text{O}$ .....	52
Figure 4.35. XRD chart for $\text{La}(\text{NO}_3)_3 \cdot 6\text{H}_2\text{O}$ + $\text{Co}(\text{NO}_3)_2 \cdot 6\text{H}_2\text{O}$ mixture.....	52

Figure 4.36. XRD chart for $\text{SrCl}_2 \cdot 6\text{H}_2\text{O} + \text{Co}(\text{NO}_3)_2 \cdot 6\text{H}_2\text{O}$ mixture.....	53
Figure 4.37. XRD chart for $\text{Co}(\text{NO}_3)_2 \cdot 6\text{H}_2\text{O} + \text{Fe}(\text{NO}_3)_3 \cdot 9\text{H}_2\text{O}$ mixture. ....	53
Figure 4.38. XRD chart for $\text{La}(\text{NO}_3)_3 \cdot 6\text{H}_2\text{O} + \text{Fe}(\text{NO}_3)_3 \cdot 9\text{H}_2\text{O}$ as-synthesized mixture. ....	53
Figure 4.39. XRD chart for $\text{SrCl}_2 \cdot 6\text{H}_2\text{O} + \text{Fe}(\text{NO}_3)_3 \cdot 9\text{H}_2\text{O}$ mixture. ....	54
Figure 4.40. XRD chart for $\text{La}(\text{NO}_3)_3 \cdot 6\text{H}_2\text{O} + \text{SrCl}_2 \cdot 6\text{H}_2\text{O} + \text{Co}(\text{NO}_3)_2 \cdot 6\text{H}_2\text{O} + \text{Fe}(\text{NO}_3)_3 \cdot 9\text{H}_2\text{O}$ mixture. ....	54
Figure 4.41. XRD chart for $\text{La}(\text{NO}_3)_3 \cdot 6\text{H}_2\text{O} + \text{SrCl}_2 \cdot 6\text{H}_2\text{O} + \text{Co}(\text{NO}_3)_2 \cdot 6\text{H}_2\text{O}$ mixture. ....	55
Figure 4.42. XRD chart for $\text{La}(\text{NO}_3)_3 \cdot 6\text{H}_2\text{O} + \text{Co}(\text{NO}_3)_2 \cdot 6\text{H}_2\text{O} + \text{Fe}(\text{NO}_3)_3 \cdot 9\text{H}_2\text{O}$ mixture. ....	55
Figure 4.43. XRD chart for $\text{La}(\text{NO}_3)_3 \cdot 6\text{H}_2\text{O} + \text{SrCl}_2 \cdot 6\text{H}_2\text{O}$ mixture. ....	55
Figure 4.44. XRD chart for $\text{La}(\text{NO}_3)_3 \cdot 6\text{H}_2\text{O} + \text{SrCl}_2 \cdot 6\text{H}_2\text{O} + \text{Fe}(\text{NO}_3)_3 \cdot 9\text{H}_2\text{O}$ mixture. ....	56
Figure 4.45. XRD chart for $\text{SrCl}_2 \cdot 6\text{H}_2\text{O} + \text{Fe}(\text{NO}_3)_3 \cdot 9\text{H}_2\text{O} + \text{Co}(\text{NO}_3)_2 \cdot 6\text{H}_2\text{O}$ mixture. ....	56
Figure 4.46. XRD chart for $\text{La}_{0.6}\text{Sr}_{0.4}\text{Co}_{0.8}\text{Fe}_{0.2}\text{O}_3$ mixture. ....	57
Figure 4.47. XRD chart for $\text{La}_{0.6}\text{Sr}_{0.4}\text{Co}_{0.2}\text{Fe}_{0.8}\text{O}_3$ mixture. ....	57
Figure 4.48. XRD chart for $\text{La}(\text{NO}_3)_3 \cdot 6\text{H}_2\text{O} + \text{Co}(\text{NO}_3)_2 \cdot 6\text{H}_2\text{O}$ mixture after heat treatment.....	58
Figure 4.50. XRD chart for $\text{Fe}(\text{NO}_3)_3 \cdot 9\text{H}_2\text{O} + \text{Co}(\text{NO}_3)_2 \cdot 6\text{H}_2\text{O}$ mixture after heat treatment.....	59
Figure 4.51. XRD chart for $\text{La}(\text{NO}_3)_3 \cdot 6\text{H}_2\text{O} + \text{Fe}(\text{NO}_3)_3 \cdot 9\text{H}_2\text{O}$ mixture after heat treatment.....	59
Figure 4.52. XRD chart for $\text{SrCl}_2 \cdot 6\text{H}_2\text{O} + \text{Fe}(\text{NO}_3)_3 \cdot 9\text{H}_2\text{O}$ mixture after heat treatment. ....	59
Figure 4.53. XRD chart for $\text{La}(\text{NO}_3)_3 \cdot 6\text{H}_2\text{O} + \text{SrCl}_2 \cdot 6\text{H}_2\text{O} + \text{Fe}(\text{NO}_3)_3 \cdot 9\text{H}_2\text{O} + \text{Co}(\text{NO}_3)_2 \cdot 6\text{H}_2\text{O}$ mixture after heat treatment. ....	60
Figure 4.54. XRD chart for $\text{La}(\text{NO}_3)_3 \cdot 6\text{H}_2\text{O} + \text{SrCl}_2 \cdot 6\text{H}_2\text{O} + \text{Co}(\text{NO}_3)_2 \cdot 6\text{H}_2\text{O}$ mixture after heat treatment. ....	61
Figure 4.55. XRD chart for $\text{La}(\text{NO}_3)_3 \cdot 6\text{H}_2\text{O} + \text{Co}(\text{NO}_3)_2 \cdot 6\text{H}_2\text{O} + \text{Fe}(\text{NO}_3)_3 \cdot 9\text{H}_2\text{O}$ mixture after heat treatment. ....	61
Figure 4.56. XRD chart for $\text{La}(\text{NO}_3)_3 \cdot 6\text{H}_2\text{O} + \text{SrCl}_2 \cdot 6\text{H}_2\text{O}$ mixture after heat treatment. ....	61
Figure 4.57. XRD chart for $\text{La}(\text{NO}_3)_3 \cdot 6\text{H}_2\text{O} + \text{SrCl}_2 \cdot 6\text{H}_2\text{O} + \text{Fe}(\text{NO}_3)_3 \cdot 9\text{H}_2\text{O}$ mixture after heat treatment. ....	62
Figure 4.58. XRD chart for $\text{SrCl}_2 \cdot 6\text{H}_2\text{O} + \text{Co}(\text{NO}_3)_2 \cdot 6\text{H}_2\text{O} + \text{Fe}(\text{NO}_3)_3 \cdot 9\text{H}_2\text{O}$ mixture after heat treatment. ....	62

Figure 4.59. XRD chart for $\text{La}_{0.6}\text{Sr}_{0.4}\text{Co}_{0.8}\text{Fe}_{0.2}\text{O}_3$ stoichiometry mixture after heat treatment. ....	63
Figure 4.60. XRD chart for $\text{La}_{0.6}\text{Sr}_{0.4}\text{Co}_{0.2}\text{Fe}_{0.8}\text{O}_3$ stoichiometry mixture after heat treatment.....	63
Figure 4.61. DTA (black) / TGA (red) analysis of $\text{La}(\text{NO}_3)_3 \cdot 6\text{H}_2\text{O}$ precursor salt. ....	65
Figure 4.63. DTA (black) / TGA (red) analysis $\text{Co}(\text{NO}_3)_2 \cdot 6\text{H}_2\text{O}$ precursor salt.....	67
Figure 4.64. DTA (black) / TGA (red) analysis $\text{Fe}(\text{NO}_3)_3 \cdot 9\text{H}_2\text{O}$ precursor salt.....	68
Figure 4.65. TGA analyses of $\text{La}(\text{NO}_3)_3 \cdot 6\text{H}_2\text{O}$ (black), $\text{SrCl}_2 \cdot 6\text{H}_2\text{O}$ (red), $\text{Co}(\text{NO}_3)_2 \cdot 6\text{H}_2\text{O}$ (green) and $\text{Fe}(\text{NO}_3)_3 \cdot 9\text{H}_2\text{O}$ (pink) precursor salts. ....	68
Figure 4.66. TGA analyses of mixtures with two ingredients. ....	71
Figure 4.67. TGA analyses of mixtures with three ingredients. ....	72
Figure 4.68. TGA analysis of mixture of $\text{La}(\text{NO}_3)_3 \cdot 6\text{H}_2\text{O} + \text{SrCl}_2 \cdot 6\text{H}_2\text{O} +$ $\text{Co}(\text{NO}_3)_2 \cdot 6\text{H}_2\text{O} + \text{Fe}(\text{NO}_3)_3 \cdot 9\text{H}_2\text{O}$ in different stoichiometry. ....	73

## LIST OF TABLES

<u>Table</u>	<u>Page</u>
Table 2.2. Decomposition reactions of $\text{La}(\text{NO}_3)_3 \cdot 6\text{H}_2\text{O}$ .....	18
Table 2.3. Decomposition reactions of $\text{SrCl}_2 \cdot 6\text{H}_2\text{O}$ .....	19
Table 2.4. Decomposition reactions of $\text{Co}(\text{NO}_3)_2 \cdot 6\text{H}_2\text{O}$ .....	19
Table 2.5. Decomposition reactions of $\text{Fe}(\text{NO}_3)_3 \cdot 9\text{H}_2\text{O}$ .....	19
Table 3.1. Particle size distribution of CGO.....	21
Table 3.2. Experimental conditions for cathode samples that were studied in this thesis. ....	26
Table 4.1. EDS analysis results of heated sample pairs.....	34
Table 4.2. EDS analysis results of heated sample pairs.....	41
Table 4.3. Last dehydration temperature, temperature at last weight loss and final weight of precursor salts. ....	69

# CHAPTER 1

## INTRODUCTION

Generation of clean, efficient and environment-friendly energy is now one of the biggest challenges for all engineers and scientists. Fuel cells are promising, efficient, energy-saving electrochemical devices that convert the chemical energy directly into electrical energy [1]. Solid oxide fuel cells (SOFCs) are the most efficient devices for conversion of chemical fuels directly into electrical power. Fuel cells are environment-friendly, since no combustion is required unlike conventional power plants [2].

In principle, a fuel cell operates like a battery. Unlike a battery, a fuel cell does not run down or require recharging. Fuel cells are almost endlessly rechargeable. It will produce energy as long as fuel is supplied. In this thesis, SOFC system was studied. An SOFC consists of two porous electrodes (anode and cathode), an electrolyte made of a dense solid oxide ceramic material between the electrodes (Figure 1.1). In a typical fuel cell, hydrogen is fed to the anode (negative electrode), and oxygen (or air) is fed to the cathode (positive electrode). At the negative anode, hydrogen is being oxidized, while at the positive cathode, oxygen is reduced. Ions are transported through the electrolyte from anode side to the cathode. Hydrogen ( $H_2$ ) and oxygen ( $O_2$ ) flow through the electrode and are converted into water ( $H_2O$ ) and heat while generating energy. [3]

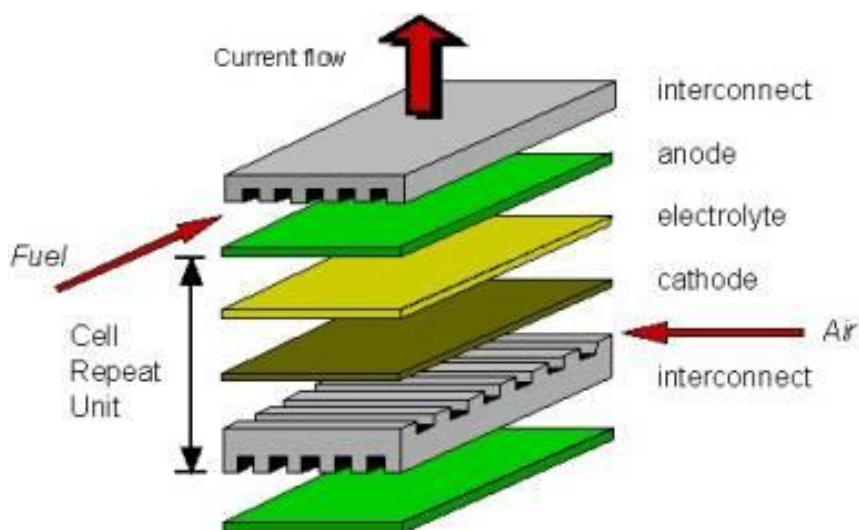


Figure 1.1. A typical schematic picture of an SOFC [4].

SOFCs have several advantages such as a high efficiency, multi-fuel capability over the other fuel cells [5]. However, the high temperature of SOFCs causes both physical and chemical corrosion of the SOFCs cell materials [6]. Huge number of activities deal with the improvement of fuel cell materials with the aim of reducing the solid oxide fuel cell (SOFC) operating temperature down from 1000°C to below 800°C. This type of SOFC is called intermediate temperature solid oxide fuel cells (IT-SOFC). The most important advantages of decreasing temperatures are reducing cost of the system and increasing lifetime of the total system [7]. Moreover, IT-SOFCs have more rapid start up and shut down processes and also, corrosion rates are significantly reduced in IT-SOFC systems [8]. However, decreasing the operating temperature causes lower cell performance due to less active electrode and poor conductive electrolyte. The key issue to improve the electrochemical performance is to reduce cathodic polarization resistance and to minimize ohmic resistance resulting from electrolyte. These mainly depend on both electro catalytic activity of the cathodes and ionic conductivity and thickness of the electrolyte [9]. The improvement of new electrolytes with high ionic conductivity as well as efforts to reduce the thickness of the electrolyte are studied to decrease the ohmic resistance [10]. Cerium gadolinium oxide (CGO) [11] [12], Ytria-stabilized zirconia (YSZ) [3] [13] are some examples of electrolyte materials which were tested for the purpose of minimizing the ohmic losses. The choice of the cathode material is strongly dependent on the type of electrolyte material. [14]. The most common cathode material used is Sr doped LaMnO<sub>3</sub> (LSM). There is a huge amount of research about new cathode materials in recent years. One of the recent examples is La<sub>1-x</sub>Sr<sub>x</sub>Co<sub>1-y</sub>Fe<sub>y</sub>O<sub>3-δ</sub> cathode material. The anode of state-of-the-art SOFCs is a cermet made of metallic nickel and a yttria stabilized zirconia skeleton (Ni-ZrO<sub>2</sub> cermet) [15].

There are several different synthesis methods that have been developed for preparation of cathode layer, such as combustion method, solid-state method, and some solution chemistry methods, for example, sol-gel process, pechini method, coprecipitation technique process [16]. Conventionally, a precursor salt solution is prepared from different salts to yield a final composition of LSCF after being coated on the heated surface of the electrolyte by ESD method [17]. But little is known in the literature about the reactions that take place during rapid heating of the salt solution which evaporates upon contact with the electrolyte substrate. The deposition of La<sub>1-x</sub>Sr<sub>x</sub>Co<sub>1-y</sub>Fe<sub>y</sub>O<sub>3-δ</sub> (LSCF) cathode material on CGO and yttria doped 3% mol zirconia (TZ-3Y) electrolyte are studied in this work. This thesis aims to investigate the thermal

decomposition and reforming reactions leading to the development of mixed oxide cathode layer with the final 6428 or 6482 LSCF composition.

A modified solid state method is chosen for the purpose of formation of LSCF ceramic. Cathode materials in compacted powder form are placed on top of the dense ceramic electrolyte at room temperature before being heated in an electric laboratory furnace for heat treatment. In addition to this, all precursor salts are examined to find out their behavior either alone or in mixture form. The purpose is to understand the course of reactions leading to the formation of the final LSCF ceramic cathode material.

In the second chapter of this thesis, some information in the literature about the SOFC materials are explained. The experimental procedure is mentioned in Chapter 3. The results of the experiments and their discussion are given in Chapter 4. Conclusions are stated in the last chapter.

## CHAPTER 2

### LITERATURE SEARCH

#### 2.1. Fuel Cells

Conventional power plants convert chemical energy into electrical energy in three steps. The first one is the production of heat by burning fuel, the second step is conversion of heat energy into mechanical energy and the last step is conversion of mechanical energy into electrical energy. The efficiency of the second step is limited (by the Second Law of Thermodynamics) to the Carnot efficiency, since the conversion of heat into mechanical energy occurs in a closed-cycle heat engine. An efficiency of about 41% can be reached by modern systems [16].

A fuel cell is an energy conversion device that produces electricity and heat directly, from a gaseous fuel by electrochemical combination of the fuel with an oxidant. Thus, it achieves theoretical efficiency which is significantly higher than that of conventional methods of power generation [17].

British physicist and lawyer, Sir William R. Grove demonstrated the basic operating principle of fuel cells in 1839. By connecting a hydrogen anode and an oxygen cathode, he gained an electric current with the experimental set-up shown in Figure 2.1 [18]. Research on fuel cells started around 1900s and then on the 21st August 1965, the Gemini 5 was the first spacecraft using a polymer membrane fuel cell (PEMFC) instead of the battery. NASA projects on fuel cells in the USA was an important step in this area [19]. There are two reasons for using fuel cells in space, first there is no harmful gas in the end of the reaction and secondly water is produced as a by-product of the reaction, which astronauts need in space.

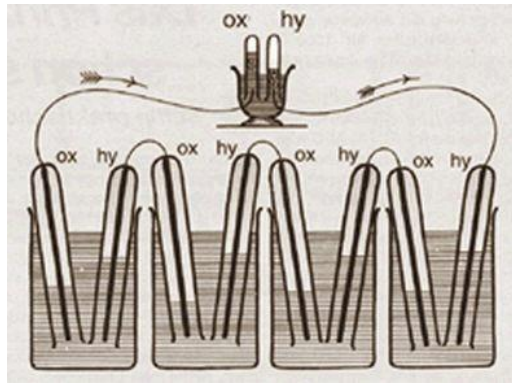


Figure 2.1. Sketch of William Grove's 1839 fuel cell [20].

A typical fuel cell system can be seen schematically in Figure 2.2. Parts of a typical fuel cell are the anode (negative side), which supplies electrons, and the cathode (positive side) which absorbs electrons. Both electrodes must be separated by an electrolyte.

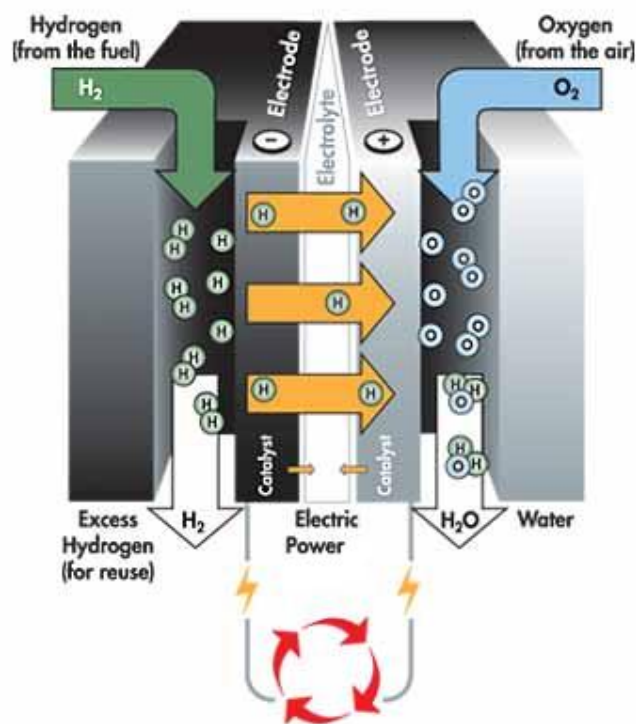


Figure 2.2. Schematic picture of a fuel cell [21].

A fuel cell resembles a battery in many respects. The operating principles of fuel cells are similar to those of batteries, i.e., electrochemical combination of ingredients to generate electricity, a combination made of a gaseous fuel (hydrogen) and an oxidant

gas (oxygen from the air) through electrodes and via an ion conducting electrolyte. [22]. However, unlike a battery, a fuel cell never needs recharging and does not run down. It continues to produce electricity as long as it is supplied by two of earth's most common elements – oxygen and hydrogen [21]. Hydrogen can be obtained from common fuels such as hydrocarbon, alcohols or coal. Oxygen is the most common oxidant because it is economically gained from air [23].

Advantages of fuel cells are;

I) High conversion efficiency: The main feature of a fuel cell is its high conversion efficiency from fuel to electricity (45 to 60%). Using waste heat can bring the system efficiency over 85%. Because they convert their energy directly into electricity, they can be two times more efficient than conventional internal combustion engines.

II) Environmentally friendly: Production of undesirable materials such as  $\text{NO}_x$ ,  $\text{SO}_x$  are either negligible or undetectable for fuel cell systems (Figure 2.3) [17].

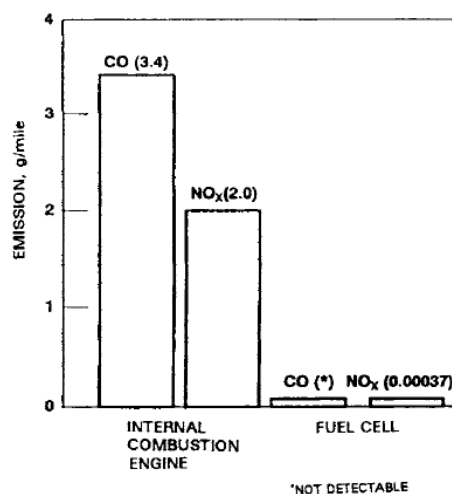


Figure 2.3. Comparison of emissions of internal combustion engine and fuel cell vehicles [23].

III) Modularity: Fuel cell size can easily be increased or decreased. The efficiency of a fuel cell is relatively independent of size. Fuel cells are lighter and can operate 10 times longer than conventional batteries [17] [21] [23] [25].

IV) Fuel flexibility: A fuel cell system can include a fuel reformer that generates hydrogen from a different range of sources including fossil fuels such as natural gas, propane and coal, alcohol fuels such as methanol, and from hydrogen compounds

containing no carbon such as ammonia or borohydride. In addition, biomass, methane, landfill gas or anaerobic digester gas from wastewater treatment plants may be used as fuel sources [17] [21] [25] [26] [27].

Other important advantages of fuel cells are constant efficiency at low load, low maintenance cost and very few moving parts (or none) and working quiet or completely silent [21].

## 2.2. Fuel Cell Types

There are different types of fuel cells, generally classified by the kind of the electrolyte and/or catalyst used. Figure 2.4 shows the major types of fuel cells along with electrolyte used, operating temperature and electrode reactions. The electrolyte used determines different operating conditions required such as heat and pressure [28].

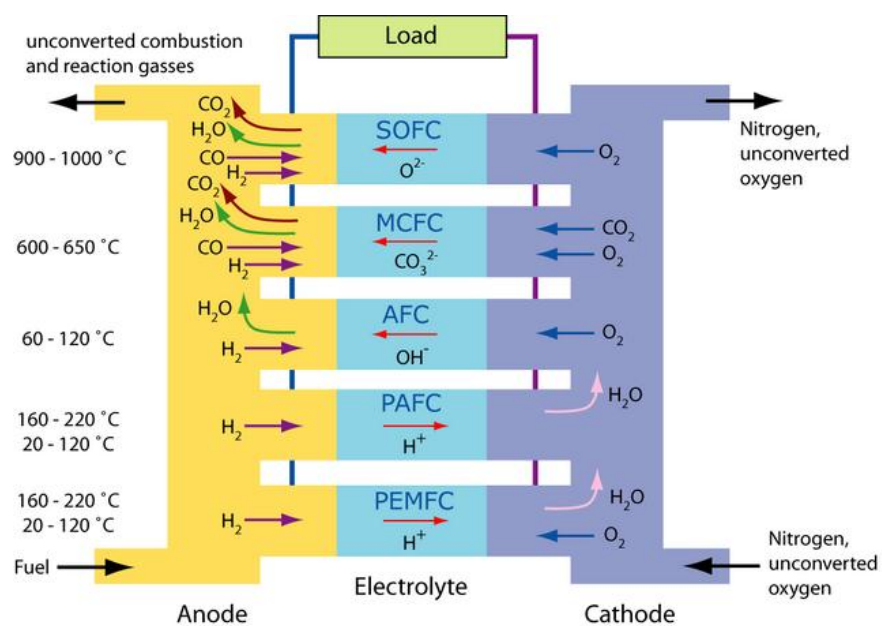


Figure 2.4. Classification of fuel cells [21]

Each fuel cell type possesses its own set of benefits. The principal ones are the alkaline fuel cell (AFC), proton exchange membrane (PEMFC) fuel cell, direct methanol fuel cell (DMFC), molten carbonate fuel cell (MCFC), phosphoric acid fuel cell (PAFC), and solid oxide fuel cell (SOFC). Fuel cell types are named by their

electrolyte. One important exception to this is the “direct methanol fuel cell”, which is defined by the fuel used [3].

### 2.2.1. Solid Oxide Fuel Cells (SOFC)

Solid oxide fuel cells (SOFCs) have potential to be the most efficient and cost-effective system for direct conversion of a wide variety of fuels to electricity [29]. As can be seen in Figure 2.5, only five components are needed to put such a cell together: the electrolyte made of a solid oxide ceramic material, two porous electrodes the anode and the cathode and two interconnect wires [1].

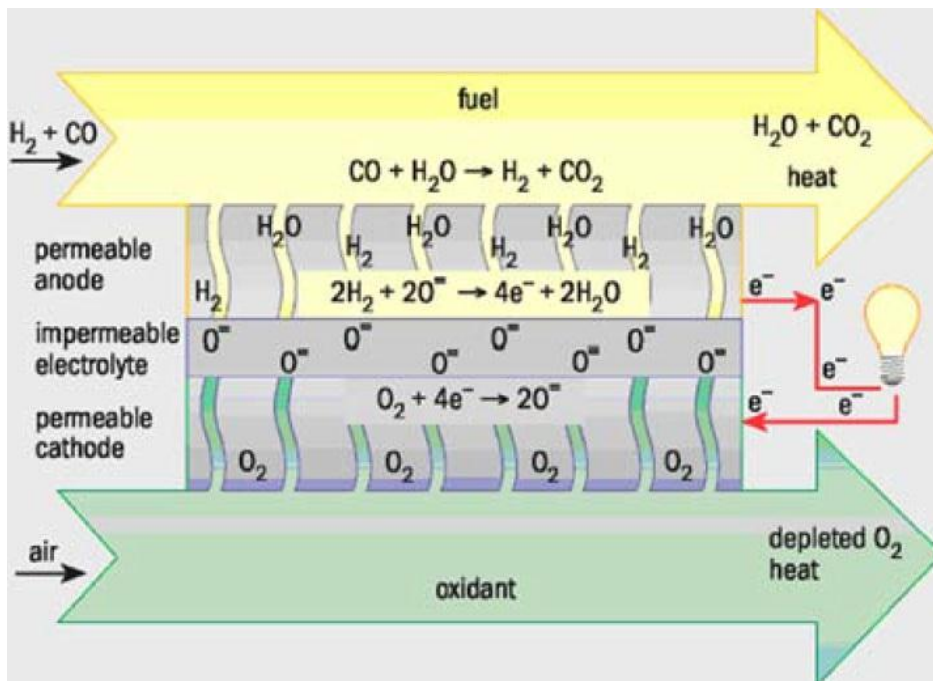


Figure 2.5. Schematic picture of an SOFC [24].

The fuel cell materials of components must possess sufficient chemical and structural stability, minimal reactivity and interdiffusion among different components, and matching thermal expansion among different components [2].

The operation of the solid oxide fuel cell is straightforward: Oxygen supplied at the cathode (air electrode) reacts with incoming electrons from the external circuit to form oxygen ions, which migrate to the anode (fuel electrode) through oxygen ions conducting electrolyte. Thanks to cathode and anode porous materials, oxygen ions

migrate from the cathode to the anode. At the anode, oxide ions react with H<sub>2</sub> (and/or CO) in the fuel to produce H<sub>2</sub>O (and/or CO<sub>2</sub>), liberating electrons. Electrons flow from the anode through the external circuit to the cathode and by this way a direct electric current is generated [2]. The operation of SOFC is summarized in the Figure 2.6.

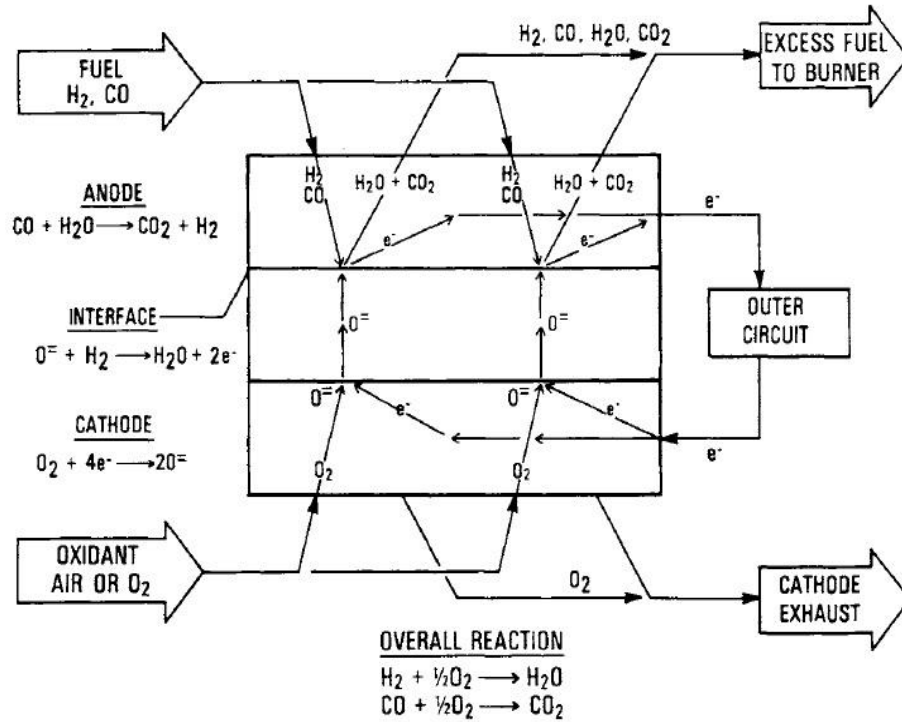


Figure 2.6. Schematic diagram of reactions in SOFCs based on oxygen-ion conductors [17]

Perovskite oxides which are the common type of oxide used in SOFCs for electrical conduction. Perovskite type oxides of general formula is ABO<sub>3</sub>, A is a large cation, B is a small cation [1]. These perovskites are used as cathode materials for ceramic fuel cells [23]. Schematic representation of the structure of perovskite is shown in Figure 2.7.

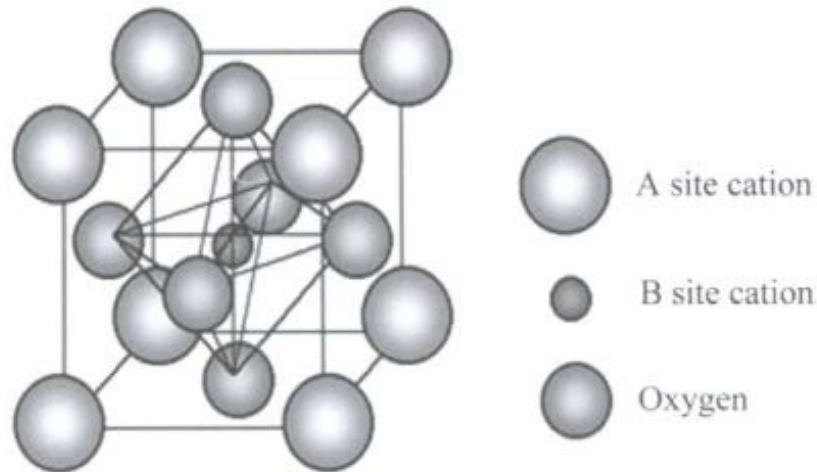


Figure 2.7 Schematic representation of structure of perovskite ( $ABO_3$ )

Main advantages of SOFC technologies over other fuel cell technologies:

- Although other types of fuel cell have to rely on a clean supply of hydrogen for their operation, SOFC can use a wide range of different fuels like natural gas, liquefied petroleum gas, biogas etc. in addition to pure hydrogen.
- SOFC has particularly high efficiency. Electrical efficiency of up to 70% is achievable.
- SOFC is made from commonly available materials and does not require expensive precious metals as catalysts [30].

Solid oxide fuel cells (SOFCs) are also quiet, vibration-free operation, reliability, modularity and very low levels of polluting emissions such as  $NO_x$ ,  $SO_x$ ,  $CO_2$  [2].

Most important disadvantage of high temperature SOFC is high material costs, especially for interconnect and construction materials. Therefore, the development of intermediate-temperature SOFCs (IT-SOFCs) has been started at 500-800°C to solve this problem. Most important benefit of IT-SOFC is operation at less than 700°C which means that low cost construction materials can be used. Another important advantage of lower temperature operation offers the more rapid start up and shut down procedures and significantly reduced corrosion rates [8][57].

Despite all these benefits, ohmic losses in the electrolyte increase dramatically as the operating temperature is reduced. There are voltage losses while oxygen ions transport from the cathode to the electrolyte by ionic resistivity and transition of electrons through the cathode to the anode by electronic resistivities. The electrolyte

causes more ohmic losses, especially IT-SOFCs with thick electrolyte. Ionic resistivity of the electrolyte is greater than electronic resistivity of the cathode and the anode. The solution of this problem is reducing the thickness of electrolyte in IT-SOFC and choosing electrolyte material which has high ionic conductivity [1].

### 2.2.1.1 Stack Design

The fuel cell stack is the heart of a fuel cell power system. A single fuel cell produces less than 1.16 volts - barely enough electricity for even the smallest applications. A typical fuel cell stack may consist of hundreds of fuel cells. [21].

Two possible design configurations for SOFCs have come out: a planar design (Figure 1.1) and a tubular design (Figure 2.8). In the planar design, the components are gathered in flat stacks, with air and fuel flowing through channels built into the cathode and anode. In the tubular design, components are gathered in the form of a hollow tube, air flows through the inside of the tube and fuel flows around the exterior.

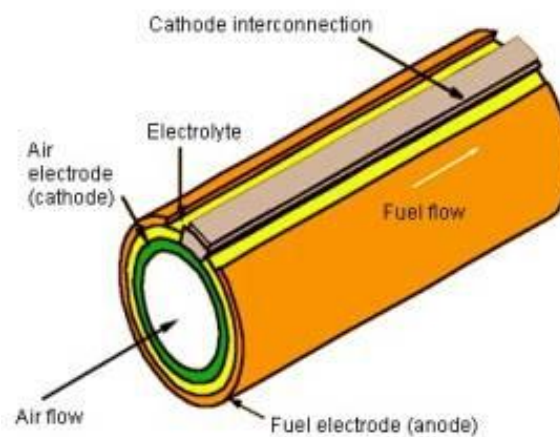


Figure 2.8. Configuration for a tubular design SOFC [4].

### 2.2.1.2 Electrolytes

The main function of the SOFC electrolyte is to conduct ions between the anode and cathode. The electrolyte carries the ions from one electrode to the other electrode and complete the electrical circuit in the fuel cell. Thus, the electrolyte must have high ionic conductivity. Its ionic conductivity must be as high as possible to minimize ohmic losses. Despite this, the electrolyte must possess low electronic conductivity to prevent

voltage losses because of the electronic current flowing through the electrolyte for SOFCs . It must be fully dense to prevent short circuiting of reacting gases through it and it should also be as thin as possible to minimize resistive losses in the cell [1] [31]. The ohmic losses over the electrolyte are one of the most important factors governing the performance of the cell. By the need to reduce the SOFC operating temperature, electrolytes with higher oxygen conductivity or thinner electrolyte structures are required [32].

Although a variety of oxide combinations has been used for solid non-porous electrolytes, present SOFCs use, almost exclusively, stabilized zirconia ( $ZrO_2$ ), especially yttria ( $Y_2O_3$ )-stabilized  $ZrO_2$  (YSZ), as the electrolyte. Yttria-doped zirconia (YSZ) remains the most widely used material for the electrolyte in SOFCs because of its sufficient ionic conductivity (with no electronic conduction) [3].

The crystalline array of  $ZrO_2$  has two oxide ions to every zirconium ion. But, in  $Y_2O_3$  there are only 1.5 oxide ions to every yttrium ion. The result is vacancies in the crystal structure where oxide ions are missing. As a result of this, oxide ions from the cathode leap from hole to hole until they reach the anode (Figure 2.9) [2][3] [17].

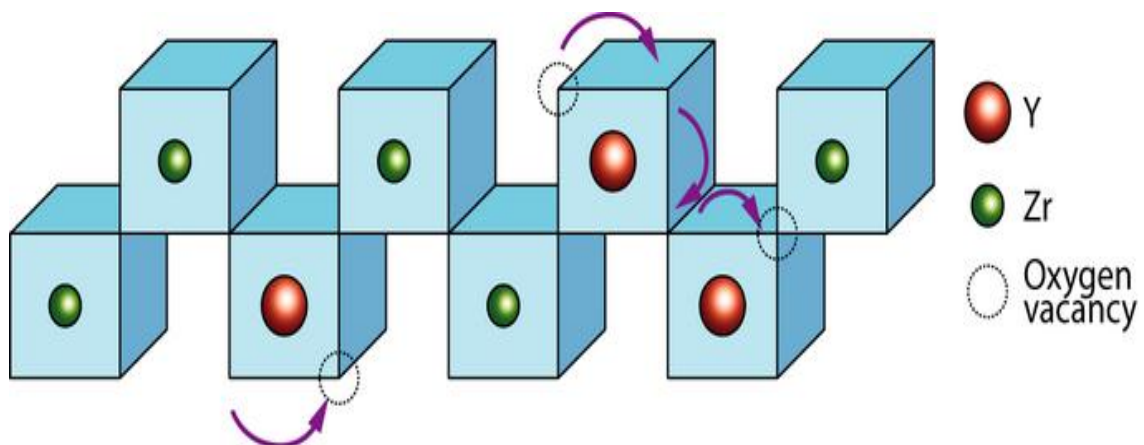


Figure 2.9. Vacancy transport in YSZ [21]

Another interesting fluorite structured material is  $CeO_2$  doped with 10 mol% GdO (CGO). Gadolinium or samarium-doped  $CeO_2$  materials possess higher oxide ion conductivity (e.g.,  $Ce_{0.9}Gd_{0.1}O_{1.95}$ : 0.025 S/cm at 600°C) compared to zirconia based materials ( $< 0.005$  S/cm-1). CGO achieves the required conductivity at 600 °C and therefore could be used in IT-SOFC operating at this temperature [2] [33].

### 2.2.1.3 Cathodes

The cathode material is vital for fuel cells because the oxidation reaction determines the efficiency of the fuel cell. The main function of the cathode is to provide reaction sites for the electrochemical reduction of the oxidant (Figure 2.10). Thus, the cathode material must be chemically, morphologically, and dimensionally stable in the oxidizing environment and must possess sufficient electronic conductivity to support electron flow in the oxidizing environment at the operating temperature. In general, maximum possible cathode conductivity is desirable to minimize ohmic losses. The cathode must have sufficient catalytic activity for the oxidant gas reaction at the operating conditions. Since the SOFC operates at high temperatures ( $600^{\circ}\text{C}$  to  $1000^{\circ}\text{C}$ ) the cathode must be chemically and thermally compatible with the other cell components, from room temperature to those operating temperatures and to the even higher temperatures at which the fuel cell is fabricated [17] [31]. In order to allow gas transport, cathodes must have porous structure [23]. In addition to these requirements, other desirable properties for the SOFC cathode are high strength and toughness and low cost [17].

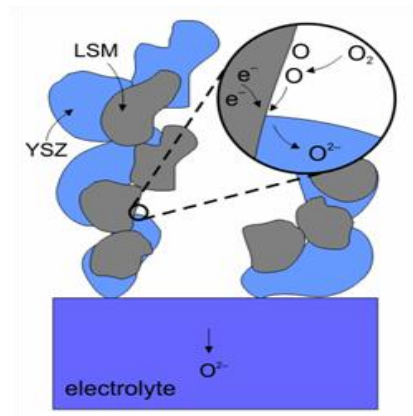


Figure 2.10. Reduction reaction on the surface of a cathode made of LSM-YSZ [35]

In the earliest stages of SOFC development, platinum was used as cathode since other appropriate materials were not available. Because platinum is expensive and not cost-effective, power generation was not practical with platinum cathodes. Less expensive perovskites [36] also possess the required properties. In 1969,  $\text{LaCoO}_3$  was tested by Tedmon et al. [37] and its initial performance in cells was good. After that, lanthanum manganite ( $\text{LaMnO}_3$ )-based materials have consequently attracted much

interest [23]. Many doped oxides are available, but only a few of them works good with the electrolyte [1].

Strontium doped  $\text{LaMnO}_3$  (LSM) has been extensively used as cathode material in the SOFCs. This selection has been based on three factors: high electrical conductivity in oxidizing atmospheres, sufficient compatibility with  $\text{Y}_2\text{O}_3$  – stabilized  $\text{ZrO}_2$  (YSZ) electrolyte, and acceptable thermal expansion match with other cell components [17].

Another approach to lowering the ohmic losses over the cathode at lower operating temperatures is the use of alternative cathode materials with mixed ionic and electronic conductivity. A lot of research are concentrating on  $\text{La}_{1-x}\text{Sr}_x\text{Co}_{1-y}\text{Fe}_y\text{O}_{3-\delta}$  (LSCF) perovskite as an alternative cathode material with high ionic conductivity, to use on ceria (i.e. CGO) or zirconia electrolytes in the last few years [32].

#### **2.2.1.4. Anodes**

The anode must be an excellent catalyst for the oxidation of fuel (hydrogen, carbon dioxide) at the operating conditions (Figure 2.11). Thus, the anode material must be stable in the fuel reducing environment of the fuel and have sufficient electronic conductivity. The oxidation reaction between the oxygen ions and the hydrogen produces heat as well as water and electricity. Also the ceramic anode layer must possess sufficient porosity to allow the fuel to flow towards the electrolyte. [2] [4] [31].

The anode is commonly the thickest and strongest layer in each individual cell. SOFC anodes are fabricated from composite powder mixtures of electrolyte material (YSZ, GDC, or SDC) and nickel oxide NiO [39]. The reduction of NiO to nickel increases the porosity of the anode. At present, nickel is used almost exclusively as the SOFC anode material because of its low cost [17] [40]. NiO/SDC and NiO/GDC anode materials are best used with ceria-based electrolyte materials [22]. The Ni/YSZ cermet anode used by most SOFC developers commonly is produced by reducing a NiO/YSZ anode [17].

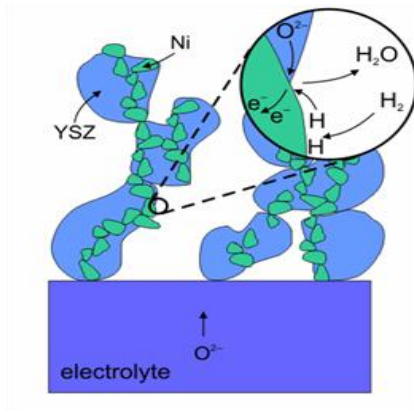


Figure 2.11. Oxidation reaction on the surface of an anode made of Ni-YSZ [35]

### 2.2.1.5. Interconnect

The primary function of the SOFC interconnect is to connect the anode of one cell to the cathode of the next cell in electrical series. The interconnect also separates the fuel from the oxidant in adjoining cells of a stack. Hence, it should not have any porosity to avoid mix of fuel and oxygen. It should have high electronic conductivity with low ionic conductivity. Thus, the interconnect material must be stable in both the reducing and oxidizing environments [1] [17].

## 2.3. Synthesis Methods for Cathode Layer Materials

Many synthesis methods have been developed for preparation of cathode layer materials, such as combustion method, sol-gel process, co-precipitation technique, and citrate process (Pechini) [56], solid-state reaction, slurry spin coating [43], glycine-nitrate method [44], spray-drying method [45], ESD method [12]. These processes is explained briefly in the following part of the chapter.

### 2.3.1. Solid State Method

Solid-state reaction, a simple and cost-effective and most accessible since the composition of products may be controlled and suitable to synthesize a large amount of perovskite type powder [50]. For example, stoichiometric amount of  $\text{La}(\text{NO}_3)_3 \cdot 6\text{H}_2\text{O}$ ,  $\text{SrCl}_2 \cdot 6\text{H}_2\text{O}$ ,  $\text{Fe}(\text{NO}_3)_3 \cdot 9\text{H}_2\text{O}$ ,  $\text{Co}(\text{NO}_3)_2 \cdot 6\text{H}_2\text{O}$  are mixed in ethanol and ball-milled for

20 hours by the purpose of preparation of LSCF cathode powder. These solution is first dried over 900<sup>0</sup>C than pressed into pellets with a stainless steel mold and finally calcined at 1050<sup>0</sup>C. The purpose of calcination is to remove any carbon residue remaining in the ash and to convert it to the desired La<sub>0.6</sub>Sr<sub>0.4</sub>Co<sub>0.2</sub>Fe<sub>0.8</sub>O<sub>3</sub> phase with a well-defined crystalline perovskite structure [43].

### **2.3.2. The Combustion Method**

The combustion method is quite useful for the production of ultrafine ceramic powders with small particle size and high porosity. The most commonly fuels used in the combustion process for synthesis are glycine, urea, citric acid, oxalyl hydrazine and sucrose.

In this method, the metal nitrates are dissolved with the fuel in distilled water and heated on a hot plate, until the water evaporation and formation of a gel phase. After that, the gel is put into in a furnace. Than, the gel undergo a combustion process and yields a powder. Afterwards, the powder is calcined in flowing air. Afterwards, the powders were uniaxially pressed and finally the pellets were sintered at temperatures of 950–1100<sup>0</sup>C [11].

### **2.3.3. Pechini Method**

The advantage of the Pechini method (polymeric precursor method) is based on the fact of its simplicity and possibility to hold the initial stoichiometry [46]. Each metal nitrate salts of La, Co, Sr and Fe is used as the starting materials in order to obtain the synthesis of La<sub>0.6</sub>Sr<sub>0.4</sub>Co<sub>0.2</sub>Fe<sub>0.8</sub>O<sub>3</sub>, for example. These precursors are first dissolved and mixed in distilled water by stirring at room temperature. The citric acid and ethylene glycol are added drop by drop as agents in the metal nitrate mixture solution and then this mixture solution is moved to the hot condition for the chemical formation of polymerization resin. The as-synthesized powders are calcined at temperature of 400 °C to remove organics and nitrates and finally annealed at the different sintering temperature either 700 or 1000 °C [42][47].

### **2.3.4. Spray-Drying Method**

Spray-drying method is a convenient method for the synthesis of cathode materials. Precursors are dissolved in distilled water with a certain molar ratio. The final solution is dried to form a mixed dry precursor via a spray-drier. The inlet air temperature is higher than exit air temperature. The as-prepared precursor is preheated at 400 °C in air, and then as-obtained product is ground in an agate mortar and finally re-sintered at 700–900 °C [45].

### **2.3.5. ESD Method**

ESD method has shown many advantages over some conventional deposition techniques, such as a simple set-up, low price and non-toxic precursors, high deposition efficiency and easy control of the surface morphology of the deposited layers [48]. Also another important advantage is the droplet sizes of electro spraying can be range from hundreds micrometers down to several tens of nanometer [49].

A precursor solution is prepared from stoichiometric mixture of  $\text{La}(\text{NO}_3)_3 \cdot 6\text{H}_2\text{O}$ ,  $\text{SrCl}_2 \cdot 6\text{H}_2\text{O}$ ,  $\text{Co}(\text{NO}_3)_2 \cdot 6\text{H}_2\text{O}$ ,  $\text{Fe}(\text{NO}_3)_3 \cdot 9\text{H}_2\text{O}$  for preparation of LSCF powder. They are dissolved in a mixture of ethanol and butyl carbitol [12].

A DC voltage is applied between an electrically conductive substrate and a nozzle, which is connected to a precursor solution. A certain flow rate of the precursor solution can be achieved at the nozzle. While the DC voltage which mainly depends on properties of precursor solution and nozzle-substrate distance is increased to a certain value the solution is atomized at the orifice of the nozzle, a spray is generated. The spray moves towards the heated substrate under the electrostatic force and, due to pyrolysis of the precursors, a thin layer is generated on the substrate surface [48].

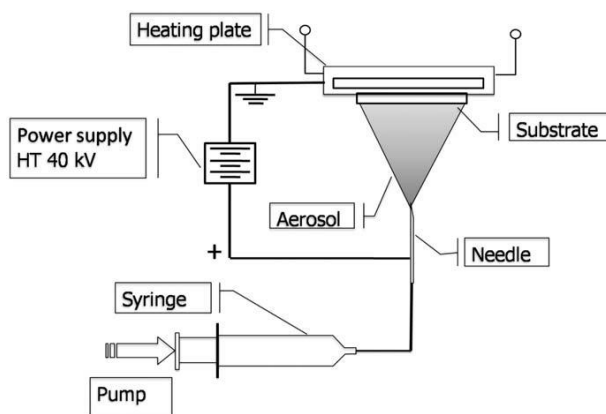


Figure 2.12. Schematic drawing of the ESD setup [12]

## 2.4. Thermal Decomposition Reactions of LSCF precursor Salts

The thermal decomposition of precursor salts is important for better understanding of the solid state reactions. Differential Thermal Analysis and Thermogravimetric Analysis (DTA/TGA) curves of  $\text{La}(\text{NO}_3)_3 \cdot 6\text{H}_2\text{O}$ ,  $\text{SrCl}_2 \cdot 6\text{H}_2\text{O}$ ,  $\text{Co}(\text{NO}_3)_2 \cdot 6\text{H}_2\text{O}$  and  $\text{Fe}(\text{NO}_3)_3 \cdot 9\text{H}_2\text{O}$  precursor salts were studied from the literature to understand the steps of the decomposition. The DTA/TGA curves of all reaction steps are listed along with their temperatures in Table 2.2 to 2.5.

Table 2.2. Decomposition reactions of  $\text{La}(\text{NO}_3)_3 \cdot 6\text{H}_2\text{O}$  [50]

Temperature ( $^{\circ}\text{C}$ )	The Decomposing Compound	Flue Gases	Molecular Weight
20	$\text{La}(\text{NO}_3)_3 \cdot 6\text{H}_2\text{O}$	-	432.9
90	$\text{La}(\text{NO}_3)_3 \cdot 5\text{H}_2\text{O}$	$\text{H}_2\text{O}$	414.9
105	$\text{La}(\text{NO}_3)_3 \cdot 4\text{H}_2\text{O}$	$\text{H}_2\text{O}$	396.9
150	$\text{La}(\text{NO}_3)_3 \cdot 3\text{H}_2\text{O}$	$\text{H}_2\text{O}$	378.9
175	$\text{La}(\text{NO}_3)_3 \cdot 2\text{H}_2\text{O}$	$\text{H}_2\text{O}$	360.9
215	$\text{La}(\text{NO}_3)_3 \cdot \text{H}_2\text{O}$	$\text{H}_2\text{O}$	342.9
410	$\text{La}(\text{OH})(\text{NO}_3)_2$	$\text{HNO}_3$	279.9
440	$\text{LaO}(\text{NO}_3)$	$\text{H}_2\text{O} + \text{N}_2\text{O}_5$	262.9
570	$\text{LaO}_{1.25}(\text{NO}_3)_{0.5}$	$\text{NO}_2$	189.9
640	$\text{La}_2\text{O}_3$	$\text{N}_2\text{O}_5$	76

Table 2.3. Decomposition reactions of  $\text{SrCl}_2 \cdot 6\text{H}_2\text{O}$  [51]

Temperature ( $^{\circ}\text{C}$ )	The Decomposing Compound	Flue Gases	Molecular Weight
25	$\text{SrCl}_2 \cdot 6\text{H}_2\text{O}$	-	266.52
66	$\text{SrCl}_2 \cdot 2\text{H}_2\text{O}$	$4\text{H}_2\text{O}$	194.52
132	$\text{SrCl}_2 \cdot \text{H}_2\text{O}$	$\text{H}_2\text{O}$	176.52
182	$\text{SrCl}_2$	$\text{H}_2\text{O}$	158.52

Table 2.4. Decomposition reactions of  $\text{Co}(\text{NO}_3)_2 \cdot 6\text{H}_2\text{O}$  [38]

Temperature ( $^{\circ}\text{C}$ )	The Decomposing Compound	Flue Gases	Molecular Weight
20	$\text{Co}(\text{NO}_3)_2 \cdot 6\text{H}_2\text{O}$	-	290.93
75	$\text{Co}(\text{NO}_3)_2 \cdot 6\text{H}_2\text{O}$ (melted locally)	-	290.93
170	$\text{Co}(\text{NO}_3)_2 \cdot \text{H}_2\text{O}$	$5\text{H}_2\text{O}$	200.93
195	Composite structure contained ; $\text{Co}(\text{NO}_3)_2$ , $\text{CoO}$ , $\text{Co}_2\text{O}_3$ , $\text{Co}_3\text{O}_4$	$\text{H}_2\text{O}$	Mixture
240	$\text{Co}_3\text{O}_4$	-	240.79

Table 2.5. Decomposition reactions of  $\text{Fe}(\text{NO}_3)_3 \cdot 9\text{H}_2\text{O}$  [34]

Temperature ( $^{\circ}\text{C}$ )	The Decomposing Compound	Flue Gases	Molecular Weight
20	$\text{Fe}(\text{NO}_3)_3 \cdot 9\text{H}_2\text{O}$	-	403.86
75	$\text{Fe}(\text{OH})(\text{NO}_3)_2 \cdot 2\text{H}_2\text{O}$	$6\text{H}_2\text{O} + \text{HNO}_3$	232.86
130	$\text{Fe}(\text{OH})(\text{NO}_3)_2 \cdot \text{H}_2\text{O}$	$\text{H}_2\text{O}$	214.86
155	$\text{Fe}(\text{OH})_2 \cdot (\text{NO}_3)$	$\text{HNO}_3$	151.86
160	$\text{FeOOH}$	$\text{HO}_3$	88.85
320	$\text{Fe}_2\text{O}_3$	$\text{H}_2\text{O}$	159.69

## CHAPTER 3

### EXPERIMENTAL

In this chapter, the materials used in the experiments and the experimental procedure are explained. This thesis is involved with the study of the decomposition of  $\text{La}(\text{NO}_3)_3 \cdot 6\text{H}_2\text{O}$ ,  $\text{SrCl}_2 \cdot 6\text{H}_2\text{O}$ ,  $\text{Co}(\text{NO}_3)_2 \cdot 6\text{H}_2\text{O}$  and  $\text{Fe}(\text{NO}_3)_2 \cdot 9\text{H}_2\text{O}$ . In the literature, these salts are used in making the cathode layer by being dissolved in a proper solvent and by being sprayed on the heated ceramic electrolyte. In this thesis, however, the salts were heated either one by one or in different combinations in ambient conditions (Table 3.1). Two different cathode materials were tested. These were  $\text{La}_{0.6}\text{Sr}_{0.4}\text{Co}_{0.8}\text{Fe}_{0.2}\text{O}_{3-\delta}$  (LSCF-6482) and  $\text{La}_{0.6}\text{Sr}_{0.4}\text{Co}_{0.2}\text{Fe}_{0.8}\text{O}_{3-\delta}$  (LSCF-6428). Zirconia TZ-3Y and Cerium Gadolinium Oxide ( $\text{Ce}_{0.9}\text{Gd}_{0.1}\text{Oxide}$ , CGO) were used as the electrolyte materials. In this chapter, some basic information about the physical and chemical characteristics of these salts are given. Production of the cathode and the ceramic electrolyte is also explained. Diffusion couple experiments and characterization of the resulting interfaces are also presented.

### 3.1. Materials and Equipments Used in the Experiments

#### 3.1.1. Precursor Salt Powders for Cathode

Precursor salt powders were Lanthanum (III) nitrate hexahydrate (ALFA-AESAR, 99.99%), Iron (III) nitrate nonahydrate (SIGMA-ALDRICH, 99.99%), Cobalt (II) nitrate hexahydrate (ALFA-AESAR, 97.7% min) and Strontium chloride hexahydrate (ALFA-AESAR, 99%) salts. These salts were selected because they are used for making LSCF cathode coating on ceramic electrolyte [22]. When mixed in proper proportions to match the LSCF-6482 composition, for example, a compound with  $\text{La}_{0.6}\text{Sr}_{0.4}\text{Co}_{0.8}\text{Fe}_{0.2}\text{O}_{3-\delta}$  formula were targeted to be produced. The acronyms used refer to the first letters of the elemental symbols, like L meaning Lanthanum.

### 3.1.2. Powders Used in the Preparation of the Electrolyte Substrate

In this thesis, Cerium Gadolinium Oxide ( $\text{Ce}_{0.9}\text{Gd}_{0.1}\text{Oxide}$ , PRAXAIR, 99.9%) and Zirconia TZ-3Y (doped with 3 mol%  $\text{Y}_2\text{O}_3$ , TOSOH, 99.9%) were used for preparing the substrate of ceramic electrolyte discs to be coated by the cathode materials which are mentioned in Section 3.2. Specific surface areas of TZ-3Y and CGO are  $16 \text{ m}^2/\text{g}$  and  $6.6 \text{ m}^2/\text{g}$ , respectively. Particle size distribution of TZ-3Y and CGO are shown in Figure 3.1 and Table 3.1, respectively.

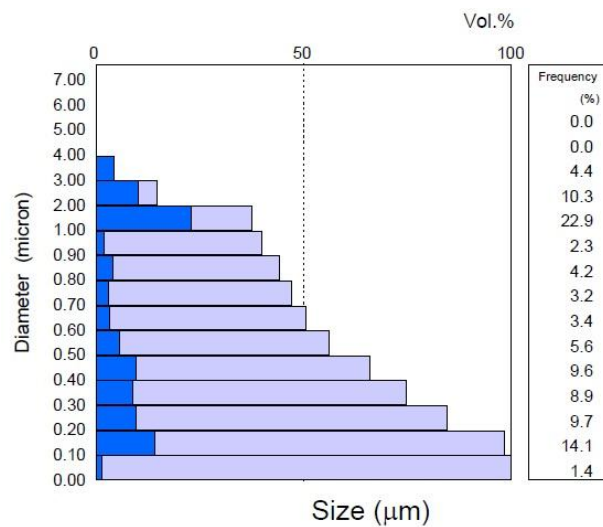


Figure 3.1. Particle size distribution of TZ-3Y.

Table 3.1. Particle size distribution of CGO.

Particle	D10	D50	D95
Size ( $\mu\text{m}$ )	0.4	0.6	0.9

### 3.2. Experimental Plan

Experiments were conducted in five stages:

- (i) powder characterization,
- (ii) effect of heating on decomposition of the salts,

- (iii) electrolyte preparation,
- (iv) mixing of the salts in different proportions
- (v) and diffusion couple experiments.

In the first part, as received salt powders were characterized by SEM, XRD and DTA/TGA. In the second stage these salts were heated and analyzed either individually or in different combinations. In the third stage the electrolyte (CGO and TZ-3Y) were made from powders by compressing in a die followed by sintering. In the fourth stage, the salts were mixed in different combinations and the resulting product were analyzed. In the fifth stage, different cathode mixtures and ceramic electrolytes were contacted and heated together to investigate interfacial reactions at high temperature. The flowchart of the experimental plan of this thesis was summarized in Figure 3.2.

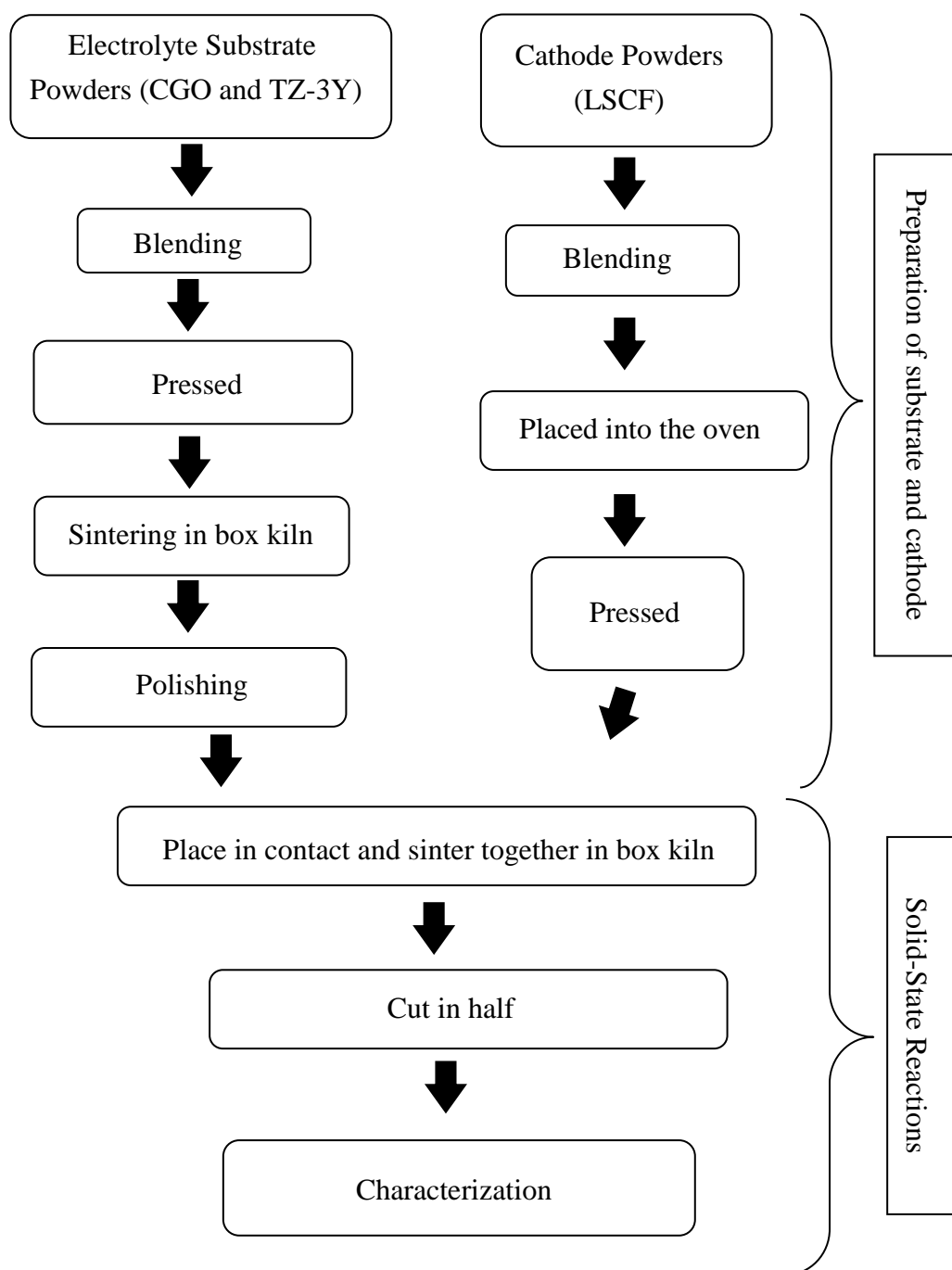


Figure 3.2. Flowchart of the experimental work followed in this thesis.

### 3.2.1. Preparation of the Substrate

Powders of CGO and TZ-3Y were ground by Agate mortar (Figure 3.4.(a) ). TZ-3Y and CGO powders were compacted by uniaxial pressing in a cylindrical stainless steel die for preparing pellets. TZ-3Y and CGO powders were poured into stainless steel

die cavity of diameters 25 and 15 mm, respectively (Figure 3.4 (c), (d) ). All of the pellets were compressed at 20 bars (2 MPa) of pressure using a hydraulic press (Yıldız Hydraulic Press, X5, İzmir, Turkey) shown in Figure 3.4 (b).

In the next step, the CGO and TZ-3Y pellets were sintered in an electrically heated laboratory kiln at 1400°C for 4 h and at 1300°C for 2 h, respectively. Nabertherm LHT 02/17, Germany was used as furnace (Figure 3.4 (e)). Heating rate was 10°C/min for all samples. CGO samples had 15 mm diameter and 2.5 mm thickness before sintering. After sintering process the same sample had 14.2 mm diameter and 2.4 mm thickness (Figure 3.3 (a) and (b) ). TZ-3Y substrates were also prepared in the shape of discs, 25 mm diameter and 3.1 mm thickness before sintering. After sintering process same samples had 17.5 mm diameter and 2.3 mm thickness (Figure 3.3 (c) (d) ). Linear shrinkages of the CGO and TZ-3Y samples were 5.33% and 30% after sintering. Green densities of CGO and TZ-3Y were  $4.20 \times 10^{-3} \text{ g/mm}^3$  and  $1.97 \times 10^{-3} \text{ g/mm}^3$ , respectively. Fired densities of CGO and TZ-3Y substrate samples were measured to be  $4.53 \times 10^{-3} \text{ g/mm}^3$  and  $5.18 \times 10^{-3} \text{ g/mm}^3$ , respectively. Then, one of the two flat surfaces of the samples were ground sequentially using 800P and 1200P grinding paper (EAC, English Abrasives Chemicals Limited, England) followed by polishing using 6  $\mu\text{m}$  and 3  $\mu\text{m}$  diamond suspensions to obtain a well-polished uniform surface by using the polishing machine named Presi, Mecapol P230. (Figure 3.4 (f) ).

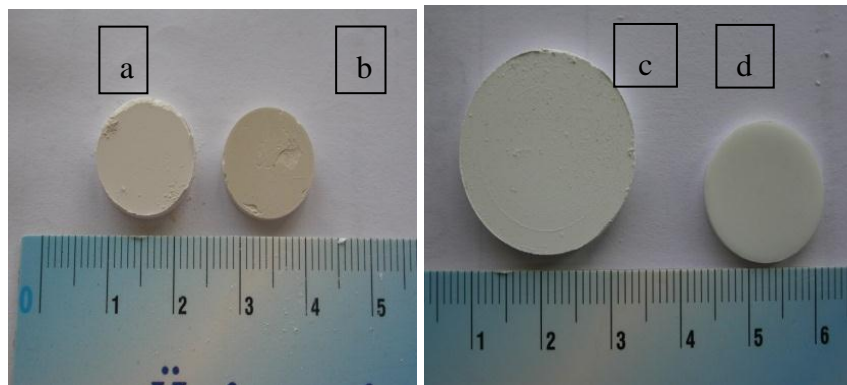


Figure 3.3. CGO Samples of pressed ceramic electrolyte discs: (a) before and (b) after sintering. TZ-3Y pellets which pressed for using as ceramic electrolyte discs: (c) before and (d) after sintering.

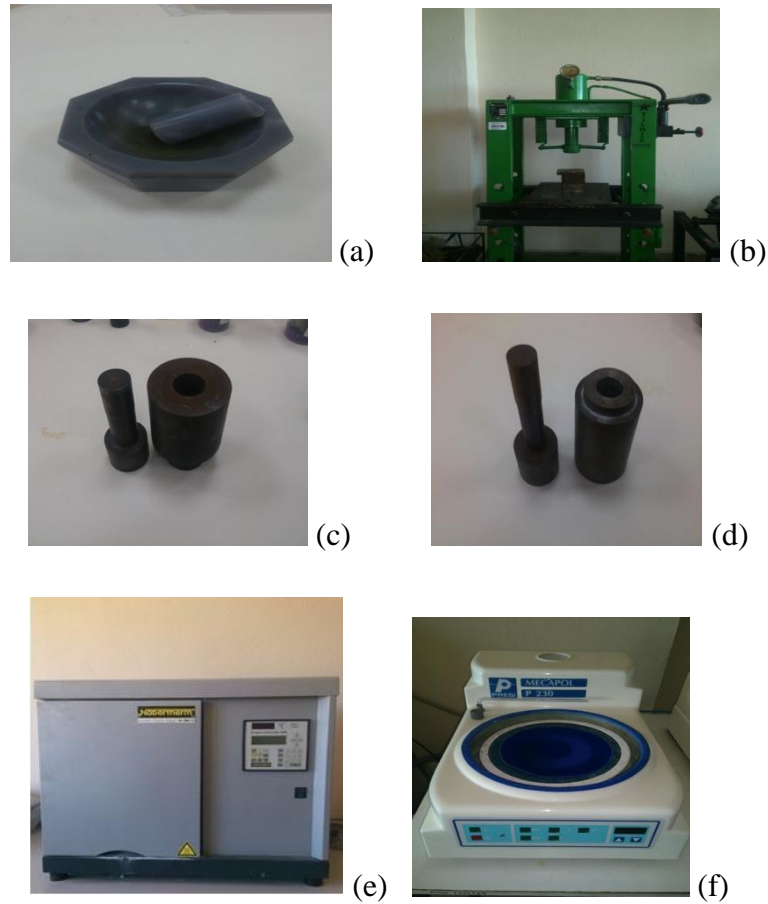


Figure 3.4. Devices used in experiments for making CGO and TZ-3Y pellets: (a) Agate Mortar, (b) Hydraulic manual pres (Yıldız Hidrolik Pres, X5), (c) Stainless steel die with  $\Phi= 25$  mm diameter , (d) Stainless steel die with  $\Phi=15$  mm diameter, (e) Box furnace used for heat treatment (Nabertherm), (f) Polishing machine Presi, Mecapol P230.

### 3.2.2. Preparation of the Cathode

$\text{La}(\text{NO}_3)_3 \cdot 6\text{H}_2\text{O}$ ,  $\text{SrCl}_2 \cdot 6\text{H}_2\text{O}$ ,  $\text{Fe}(\text{NO}_3)_3 \cdot 9\text{H}_2\text{O}$  and  $\text{Co}(\text{NO}_3)_2 \cdot 6\text{H}_2\text{O}$  were used as precursor salts. In the literature, these salts are used for making the solution to be sprayed on the heated ceramic electrolyte. Therefore, in this study these salts were selected for more detailed investigations.

These salts were blended in different combinations. Mixtures of groups of double and triple salts as well as mixtures matching  $\text{La}_{0.6}\text{Sr}_{0.4}\text{Co}_{0.8}\text{Fe}_{0.2}\text{O}_{3-\delta}$  (LSCF-6482) and  $\text{La}_{0.6}\text{Sr}_{0.4}\text{Co}_{0.2}\text{Fe}_{0.8}\text{O}_{3-\delta}$  (LSCF-6428) were prepared. Salts were mixed in different proportions as listed in Table 3.2.

Table 3.2. Experimental conditions for cathode samples that were studied in this thesis.

Sample No.	Colour at 55°C	Colour after heat treatment <sup>3</sup>	Sample Composition
1	White	-	L <sup>1</sup>
2	White	-	Sr <sup>1</sup>
3	Red	-	C <sup>1</sup>
4	Light Purple	-	F <sup>1</sup>
5	Pink	Grey	L+C <sup>2</sup>
6	Purple	Grey	S+C <sup>2</sup>
7	Light Brown	Grey	F+C <sup>2</sup>
8	Brick Colored	Red	F+L <sup>2</sup>
9	Dark Brown	Black	F+S <sup>2</sup>
10	Brown	Black	L+S+C+F <sup>2</sup>
11	Purple	Black	L+S+C <sup>2</sup>
12	Dark White	Black	L+F+C <sup>2</sup>
14	White	White	L+S <sup>2</sup>
15	Earth Colored	Black	L+S+F <sup>2</sup>
16	Dark Brown	Black	S+F+C <sup>2</sup>
17	Light Brown	Black	La <sub>0.6</sub> Sr <sub>0.4</sub> Co <sub>0.8</sub> Fe <sub>0.2</sub> O <sub>3-δ</sub> <sup>2</sup>
18	Dark Red	Black	La <sub>0.6</sub> Sr <sub>0.4</sub> Co <sub>0.2</sub> Fe <sub>0.8</sub> O <sub>3-δ</sub> <sup>2</sup>

<sup>1</sup> L represent La(NO<sub>3</sub>)<sub>3</sub>.6H<sub>2</sub>O, S represent SrCl<sub>2</sub>.6H<sub>2</sub>O C represent, Co(NO<sub>3</sub>)<sub>2</sub>.6H<sub>2</sub>O, F represent Fe(NO<sub>3</sub>)<sub>3</sub>.9H<sub>2</sub>O

<sup>2</sup> Samples number 5 to 17 were prepared in one to one molar ratio. Sample number 17 was prepared in 6:4:8:2 molar ratio. Sample number 18 was prepared in 6:4:2:8 molar ratio.

<sup>3</sup> Samples were heated according to the heat schedule in Figure 3.6.

Powders of these salts were blended and deagglomerated by Agate mortar and pestle in the order listed in Table 3.1 (Figure 3.4.(a) ). These salts were placed into the oven (Nüve Etüv FN 500, Ankara) heated at 55<sup>0</sup>C for 12-18 h until they thoroughly dried. The samples were taken out from the oven and were compacted by uniaxial pressing in a stainless steel die for preparing the pellets. Samples were poured into the stainless steel die cavity of 8 mm diameter. All of the pellets were compressed at 20 bars (2 MPa) of pressure using a hydraulic press device (Yıldız Hydraulic Press, X5, İzmir, Turkey) shown in Figure 3.4 (b).

Pellets were prepared from salt mixtures according to Table 3.2. Samples of pressed discs before sintering process were shown in Figure 3.5.

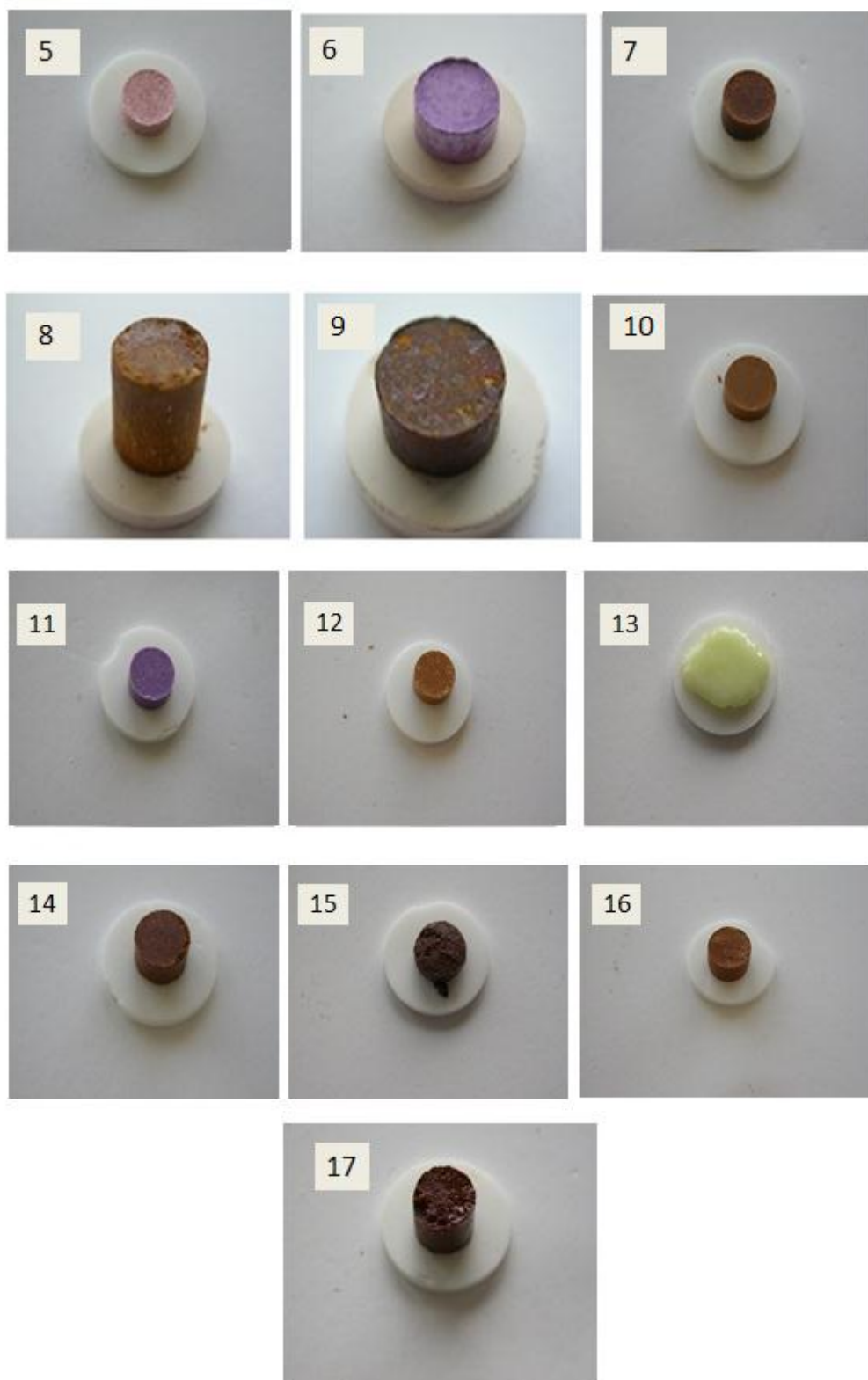


Figure 3.5. Samples of pressed discs before sintering process (5) L+C , (6) S+C , (7) F+C , (8) L+F , (9) S+F , (10) LSCF , (11) L+S+C , (12) L+S , (13) L+S+F, (14) L+F+C , (15) S+F+C, (16)  $L_6S_4C_8F_2$ , (17)  $L_6S_4C_2F_8$ .

### 3.2.3. Solid-State Reaction Process

Solid state reaction process, comprises these steps;

As aforementioned, also shown in Figure 3.3, two different ceramic electrolyte substrates of CGO and TZ-3Y were used. LSCF pellets were placed on top of the electrolytes (CGO or TZ-3Y) and they were put into the furnace together for heating (Nabertherm, LHT 02/17 in İzmir, Turkey). Heating schedule is shown in Figure 3.6.

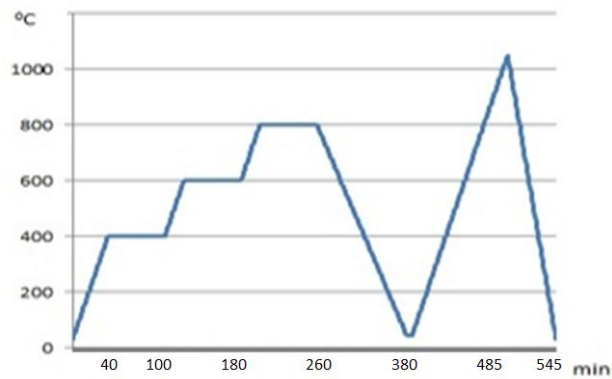


Figure 3.6. Heating schedule for LSCF precursors.

After thermal treatment, pellet couples were removed from the furnace and hot molding was performed on these pellets by Struers Cito Press-1 (Figure 3.7(a) ). Later on, they were cut by Struers Minitom by help of diamond cutting disk (Figure 3.7(b) ). Subsequently these broken pellet pieces were first ground by 800P and 1200P grinding paper, and then polished by 6  $\mu\text{m}$  and 3  $\mu\text{m}$  diamond suspensions. Presi, Mecapol P230 polishing machine is shown in Figure 3.7(c). Finally, samples were ready for characterization.



Figure 3.7. Devices used in the experiments (a) Hot mounting press (b) Low speed diamond saw used for cutting samples (c) Polishing machine

### 3.3. Characterization

Characterization techniques for investigating the  $\text{La}_{0.6}\text{Sr}_{0.4}\text{Co}_{0.8}\text{Fe}_{0.2}\text{O}_{3-\delta}$ ,  $\text{La}_{0.6}\text{Sr}_{0.4}\text{Co}_{0.2}\text{Fe}_{0.8}\text{O}_{3-\delta}$  are explained in this section. Relationship between  $\text{La}_{0.6}\text{Sr}_{0.4}\text{Co}_{0.8}\text{Fe}_{0.2}\text{O}_{3-\delta}$  /  $\text{La}_{0.6}\text{Sr}_{0.4}\text{Co}_{0.2}\text{Fe}_{0.8}\text{O}_{3-\delta}$  and CGO/TZ-3Y were searched by using the characterization techniques which were thermogravimetric analysis (DTA/TG, Perkin Elmer Diomand) for thermal property characterization; X-ray diffraction (XRD, Philips Xpert Pro ) and scanning electron microscopy (SEM, FEI Quanta 250 FEG) for microstructural characterization.

#### 3.3.1. Scanning Electron Microscopy

The microstructure of LSCF powders and the interface between LSCF film and electrolyte were investigated by Scanning Electron Microscopy (SEM) using FEI Quanta 250 FEG equipment. The acceleration voltage was 20 kV, backscattering electron image was used.

When interpreting the EDS analysis results a new term was defined in this thesis: distribution ratio is calculated by the proportion of any element in the substrate layer divided by its proportion of the same element in the coating layer. A high distribution ratio indicates significant diffusion of the element to the substrate.

#### 3.3.2. X-Ray Diffraction Analysis

The crystallographic structures of materials were analyzed by using Philips X'Pert Pro X-Ray Diffraction (XRD) device with  $\text{Cu-K}\alpha$  radiation ( $\lambda = 1,54 \text{ nm}$ ) with 0,0330 step size in the Bragg–Brentano geometry from  $5^\circ$  to  $80^\circ$  general scanning.

#### 3.3.3. Differential Thermal Analysis (DTA/ TGA)

For the purpose to determine the thermal decomposition temperatures, thermogravimetric analysis (TGA) and differential thermal analysis (DTA) were performed on  $\text{La}(\text{NO}_3)_3 \cdot 0.6\text{H}_2\text{O}$ ,  $\text{SrCl}_2 \cdot 6\text{H}_2\text{O}$ ,  $\text{Fe}(\text{NO}_3)_2 \cdot 9\text{H}_2\text{O}$ ,  $\text{Co}(\text{NO}_3)_2 \cdot 6\text{H}_2\text{O}$  as-

received and  $\text{La}_{0.6}\text{Sr}_{0.4}\text{Co}_{0.8}\text{Fe}_{0.2}\text{O}_{3-\delta}$ ,  $\text{La}_{0.6}\text{Sr}_{0.4}\text{Co}_{0.2}\text{Fe}_{0.8}\text{O}_{3-\delta}$  as-prepared with using Perkin Elmer Diamond device under ambient atmosphere (20 ml/min  $\text{N}_2$ ). Samples were heated from  $25^\circ\text{C}$  to  $900^\circ\text{C}$  at a heating rate of  $10^\circ\text{C}/\text{min}$ .

## CHAPTER 4

### RESULTS AND DISCUSSION

In this chapter, the results of experiments aimed at finding the reactions in several different mixtures of LSCF precursors and their interaction with CGO and zirconia substrates are presented and discussed. DTA, TGA, XRD, SEM and EDS analyses were performed in order to understand LSCF process better.

In the first part of this chapter, SEM micrographs of precursor salts are given. Different salt mixtures were heated at 800<sup>0</sup>C for 1 hour followed by heating to 1050<sup>0</sup>C without a soak time. Samples were heated on zirconia and CGO substrates. Their cross sectional micrographs are also shown.

In the second part of the experiments, results of XRD analysis of as-received and heated sample mixtures are presented.

In the last part of this chapter, results of DTA/TGA analysis of as-received and heated sample mixtures are given.

#### 4.1. SEM Analyses

##### 4.1.1 SEM Analyses of As-Received Precursor Salts

As received precursor salt powders were first observed using Scanning Electron Microscope (SEM). Their images are shown in Figures 4.1. to 4.4. The powder  $\text{Co}(\text{NO}_3)_2 \cdot 6\text{H}_2\text{O}$  appeared slightly different from the other powders. It looked more like a partially sintered ceramic. This is thought to originate from the premature hydration of the powder in ambient conditions. A similar observation was made with  $\text{Fe}(\text{NO}_3)_3 \cdot 9\text{H}_2\text{O}$  powder to a lesser extent.

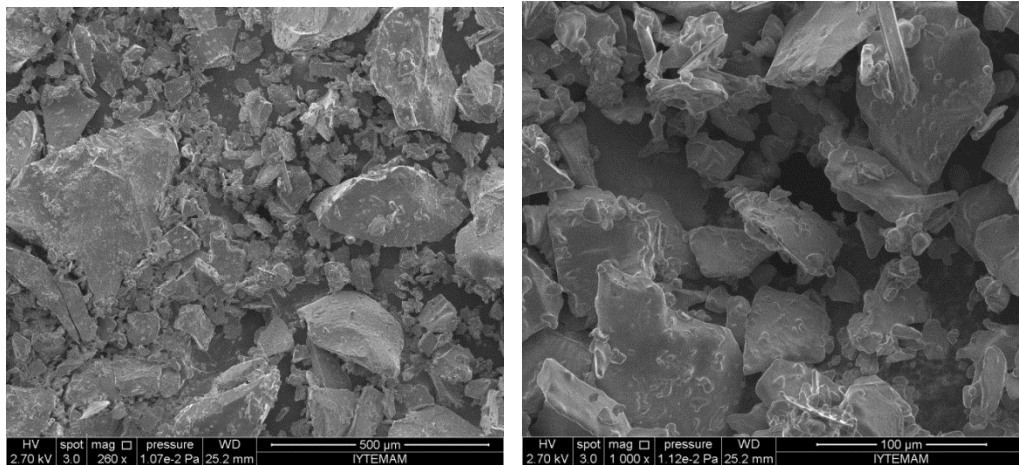


Figure 4.1. SEM image of as-received precursor salt (La(NO<sub>3</sub>)<sub>3</sub>·6H<sub>2</sub>O) at different magnifications.

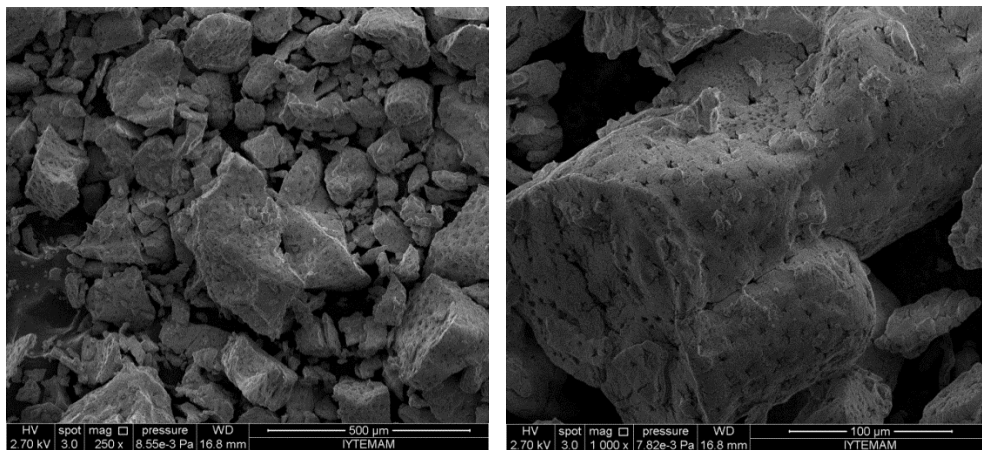


Figure 4.2. SEM image of as-received precursor salt (SrCl<sub>2</sub>·6H<sub>2</sub>O) at different magnifications.

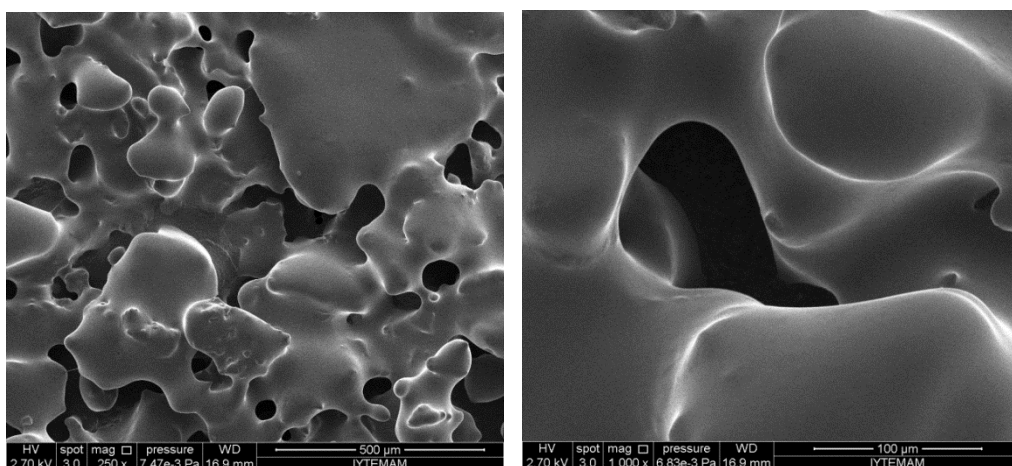


Figure 4.3. SEM image of third as-received precursor salt (Co(NO<sub>3</sub>)<sub>2</sub>·6H<sub>2</sub>O) at different magnifications.

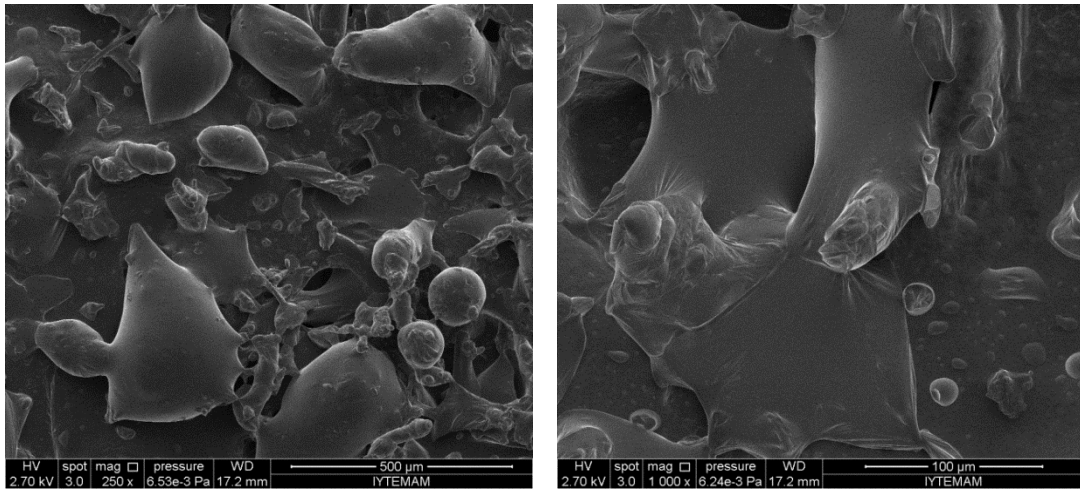


Figure 4.4. SEM image of fourth as-received precursor salt ( $\text{Fe}(\text{NO}_3)_3 \cdot 9\text{H}_2\text{O}$ ) at different magnifications.

#### 4.1.2. Diffusion Couple Heating Experiments

In this section, results of SEM observations of polished cross-sections of heat treated pairs of samples are given. The pairs were always composed of an electrolyte and a cathode material which were heated at high temperature. The purpose was to measure the extent of mutual elemental diffusion between the cathode and the electrolyte. After heating at  $800^\circ\text{C}$  for one hour the pairs mostly stuck well and diffused into each other. This was obviously an expected observation. SEM and EDS analyses were performed to create elemental dot-maps to identify the diffusion directions of the elements. Zirconia was the substrate in pairs in Section 4.1.2.1 while CGO was the substrate for the pairs in Section 4.1.2.2. Table 4.1 and 4.2 shows the elemental analysis data produced by EDS method for Zirconia and CGO, respectively. On the leftmost column the abbreviations refer to the first letter of the precursor salt. L refers to  $\text{La}(\text{NO}_3)_3 \cdot 6\text{H}_2\text{O}$ , S refers to  $\text{SrCl}_2 \cdot 6\text{H}_2\text{O}$ , C refers to  $\text{Co}(\text{NO}_3)_2 \cdot 6\text{H}_2\text{O}$  and F refers to  $\text{Fe}(\text{NO}_3)_3 \cdot 9\text{H}_2\text{O}$ . The substrate is always underneath the other pellet which is called the coating. In most experiments the coating partially fused and well spread on the substrate, while in some cases it slightly foamed but was still well stuck on the substrate surface. A distribution ratio term which was defined in Chapter 3.3.1 was used in Table 4.1 and 4.2. This ratio provides a measure of the distribution of the element into the substrate. If this ratio is small, the element is unable to diffuse into the substrate.

#### 4.1.2.1. SEM and EDS Analysis of Heated TZ-3Y Electrolyte-Cathode Pair Samples

As was expected, according to the EDS analysis (Table 4.1) approximately 67-74% of the substrate was zirconium and 25-32% of the substrate was composed of oxygen (except 4th sample). Rest of the substrate consisted of elements which penetrated from the cathode layer into the substrate. However, precursor elements were observed to be unsurprisingly gathered in the cathode layer.

Table 4.1. EDS analysis results of heated sample pairs.

Pair codes	Zr (%)	O (%)	La (%)	Sr (%)	Co (%)	Fe (%)	Cl (%)
1) L + C (substrate)	71.48	25.61	2.62	0.00	0.29	0.00	0.00
1) L + C (coating)	48.95	23.46	12.21	0.00	15.38	0.00	0.00
1) Distribution ratio	-	-	0.21	-	0.02	-	-
2) S + C (substrate)	67.30	32.37	0.00	0.00	0.00	0.00	0.11
2) S + C (coating)	0.00	18.26	0.00	43.95	6.21	0.00	31.58
2) Distribution ratio	-	-	-	0.00	0.00	-	-
3) F + C (substrate)	72.33	25.69	0.00	0.00	1.36	0.55	0.00
3) F + C (coating)	3.29	22.03	0.00	0.00	34.16	40.52	0.00
3) Distribution ratio	-	-	-	-	0.04	0.01	-
4) F + L (substrate)	57.70	42.00	0.00	0.00	0.09	0.00	0.00
4) F + L (coating)	0.00	32.77	45.11	0.00	0.00	19.71	0.00
4) Distribution ratio	-	-	0.00	-	-	0.00	-
5) F + S (substrate)	73.89	25.96	0.00	0.00	0.00	0.15	0.00
5) F + S (coating)	3.34	14.10	0.00	46.57	0.00	17.94	17.34
5) Distribution ratio	-	-	-	0.00	-	0.01	-
6)L+S+C+F (substrate)	73.27	25.87	0.46	0.00	0.14	0.18	0.08
6)L+S+C+F (coating)	0.00	29.20	22.10	19.50	9.70	9.70	9.70
7) Distribution ratio	-	-	0.02	0.00	0.01	0.02	-
7) L+S+C (substrate)	72.33	25.69	1.31	0.00	0.32	0.00	0.36
7) L+S+C (coating)	0.00	14.54	28.68	25.65	18.06	0.00	13.07
7) Distribution ratio	-	-	0.04	0.00	0.02	-	-
8) L+C+F (substrate)	73.75	25.95	0.03	0.00	0.00	0.26	0.00
8) L+C+F (coating)	2.49	18.64	39.52	0.00	22.14	17.20	0.00
8) Distribution ratio	-	-	0.00	-	0.00	0.01	-

(cont. on next page)

**Table 4.1 (cont.)**

9) L+S (substrate)	73.51	25.90	0.43	0.00	0.00	0.12	0.04
9) L+S (coating)	0.00	13.89	45.33	32.86	0.00	0.00	7.72
9) Distribution ratio	-	-	0.01	0.00	-	-	-
10) L+S+F (substrate)	69.96	25.63	0.27	0.35	0.00	0.23	3.56
10) L+S+F (coating)	5.17	16.39	34.71	27.93	0.00	11.81	3.62
10) Distribution ratio	-	-	0.01	0.01	-	0.02	-
11)S+F+C (substrate)	73.21	25.91	0.00	0.00	0.21	0.59	0.08
11) S+F+C (coating)	0.00	15.68	0.00	45.66	11.34	14.90	12.42
11) Distribution ratio	-	-	-	0.00	0.02	0.04	-
12) LSCF 6482 (substrate)	68.29	30.53	0.56	0.00	0.41	0.21	0.00
12) LSCF 6482 (coating)	5.97	33.56	25.53	15.90	12.08	2.43	4.53
12)Distribution ratio	-	-	0.02	0.00	0.03	0.09	-
13) LSCF 6428(substrate)	72.77	25.79	0.63	0.00	0.17	0.38	0.25
13) LSCF 6428(substrate)	0.00	17.32	33.25	20.64	4.17	23.30	1.32
13)Distribution ratio	-	-	0.02	0.00	0.04	0.01	-

SEM micrograph of the interface between zirconia electrolyte substrate and mixture as observed on the cross section after combination heat treatment at 800°C and 1050°C and by the help of mapping analysis, the distribution of La, Sr, Co, Fe and Zr in the cathode and the electrolyte layers can be observed. Diffusion of species was observed in dot-maps in Figures (4.6, 4.8, 4.10, 4.12, 4.14 and 4.16). However, the distribution of Zr was not taken into much of consideration. As can be seen from SEM images in Figures (4.5, 4.7, 4.9, 4.11, 4.13 and 4.15), most of the precursor mixtures generated a uniform and porous cathode layer all over the substrate by heat treatment. This is important because an ample supply of oxygen is necessary for electrochemical reaction for oxygen reduction in the electrolyte as mentioned before in Chapter 2.1.1.1.

The first pair studied was  $\text{La}(\text{NO}_3)_3 \cdot 6\text{H}_2\text{O} + \text{Co}(\text{NO}_3)_2 \cdot 6\text{H}_2\text{O}$  mixture (also coded as L+C) heated on top of zirconia. The second pair studied was  $\text{SrCl}_2 \cdot 6\text{H}_2\text{O} + \text{Co}(\text{NO}_3)_2 \cdot 6\text{H}_2\text{O}$  (S+C), third pair was  $\text{Co}(\text{NO}_3)_2 \cdot 6\text{H}_2\text{O} + \text{Fe}(\text{NO}_3)_3 \cdot 9\text{H}_2\text{O}$  (C+F) mixture, fourth pair was the mixture of  $\text{La}(\text{NO}_3)_3 \cdot 6\text{H}_2\text{O} + \text{Fe}(\text{NO}_3)_3 \cdot 9\text{H}_2\text{O}$  (L+F), the fifth pair was  $\text{SrCl}_2 \cdot 6\text{H}_2\text{O} + \text{Fe}(\text{NO}_3)_3 \cdot 9\text{H}_2\text{O}$  mixture, the ninth pair was  $\text{La}(\text{NO}_3)_3 \cdot 6\text{H}_2\text{O} + \text{SrCl}_2 \cdot 6\text{H}_2\text{O}$  and finally the tenth combination studied was the mixture of  $\text{La}(\text{NO}_3)_3 \cdot 6\text{H}_2\text{O} + \text{SrCl}_2 \cdot 6\text{H}_2\text{O} + \text{Fe}(\text{NO}_3)_3 \cdot 9\text{H}_2\text{O}$  (also coded as L+S+F) heated on top of zirconia. Results of the experiments using these pairs are explained in the Appendix A.

The sixth combination studied was the mixture of  $\text{La}(\text{NO}_3)_3 \cdot 6\text{H}_2\text{O} + \text{SrCl}_2 \cdot 6\text{H}_2\text{O} + \text{Co}(\text{NO}_3)_2 \cdot 6\text{H}_2\text{O} + \text{Fe}(\text{NO}_3)_3 \cdot 9\text{H}_2\text{O}$  (also coded as LSCF) in 1:1:1:1 molar ratio, heated on top of zirconia. Figure 4.5 shows the SEM micrograph of the interface between zirconia electrolyte substrate and this mixture as observed on the cross section. Owing to mapping analysis, the distribution of La, Sr, Co, Fe and Zr in the cathode and the electrolyte layers can be observed. Despite diffusion of zirconium was observed to be limited at the interface, some diffusion of other elements into the substrate was observed as shown in Figure 4.6. Diffusion ratio into the substrate of Sr was lowest among all La, Sr, Co and Fe according to the EDS analysis in Table 4.1.

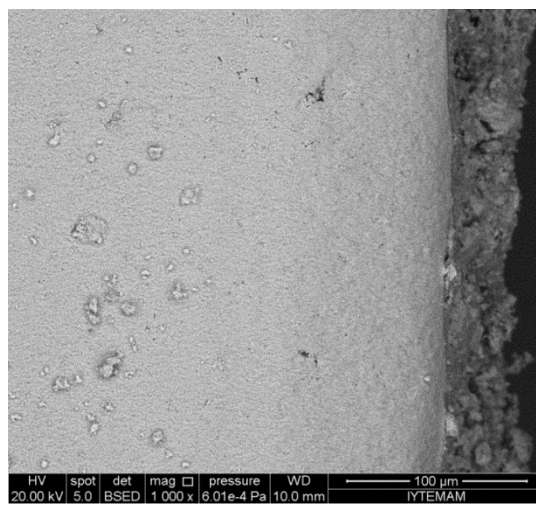


Figure 4.5. SEM image of the interface between  $\text{La}(\text{NO}_3)_3 \cdot 6\text{H}_2\text{O} + \text{SrCl}_2 \cdot 6\text{H}_2\text{O} + \text{Co}(\text{NO}_3)_2 \cdot 6\text{H}_2\text{O} + \text{Fe}(\text{NO}_3)_3 \cdot 9\text{H}_2\text{O}$  mixture and zirconia pellets after heat treatment.

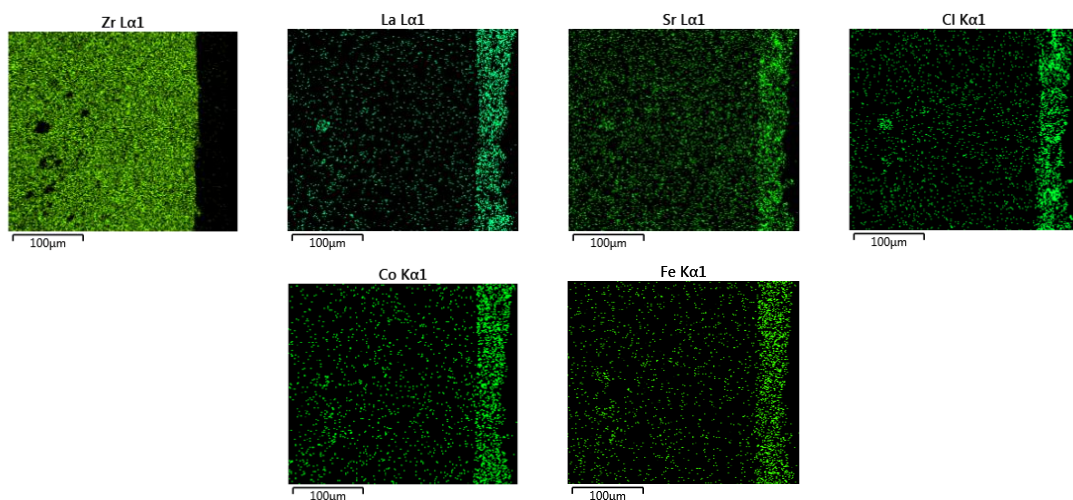


Figure 4.6. Mapping analysis of the interface between  $\text{La}(\text{NO}_3)_3 \cdot 6\text{H}_2\text{O} + \text{SrCl}_2 \cdot 6\text{H}_2\text{O} + \text{Co}(\text{NO}_3)_2 \cdot 6\text{H}_2\text{O} + \text{Fe}(\text{NO}_3)_3 \cdot 9\text{H}_2\text{O}$  mixture and zirconia pellets after heat treatment.

The combination mixture containing  $\text{La}(\text{NO}_3)_3 \cdot 6\text{H}_2\text{O} + \text{SrCl}_2 \cdot 6\text{H}_2\text{O} + \text{Co}(\text{NO}_3)_2 \cdot 6\text{H}_2\text{O}$  (also coded L+S+C) that was heated on top of zirconia indicated that the diffusion of all three species was limited in the interface (Figure 4.8). In reference to the EDS analysis, La and Co had weak distribution ratio and Sr had insignificant diffusion into the substrate (Table 4.1).

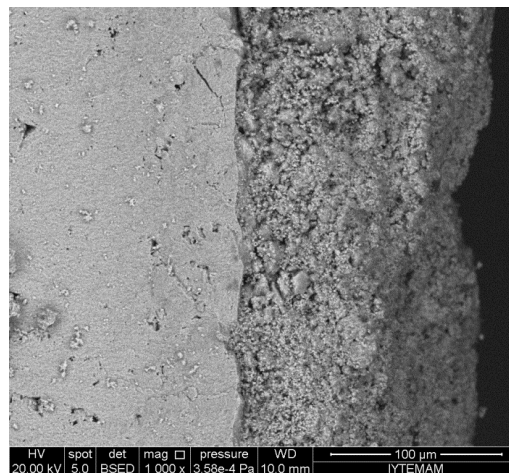


Figure 4.7. SEM image of the interface between  $\text{La}(\text{NO}_3)_3 \cdot 6\text{H}_2\text{O} + \text{SrCl}_2 \cdot 6\text{H}_2\text{O} + \text{Co}(\text{NO}_3)_2 \cdot 6\text{H}_2\text{O}$  mixture and zirconia pellets after heat treatment.

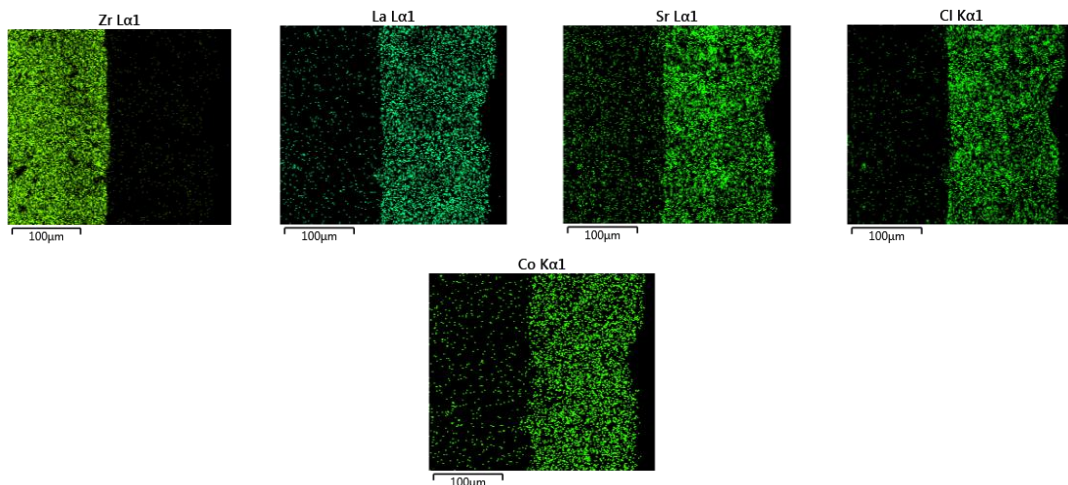


Figure 4.8. Mapping analysis of the interface between  $\text{La}(\text{NO}_3)_3 \cdot 6\text{H}_2\text{O} + \text{SrCl}_2 \cdot 6\text{H}_2\text{O} + \text{Co}(\text{NO}_3)_2 \cdot 6\text{H}_2\text{O}$  mixture and zirconia pellets after heat treatment.

The mixture of  $\text{La}(\text{NO}_3)_3 \cdot 6\text{H}_2\text{O} + \text{Co}(\text{NO}_3)_2 \cdot 6\text{H}_2\text{O} + \text{Fe}(\text{NO}_3)_3 \cdot 9\text{H}_2\text{O}$  salts heated on top of zirconia showed faster diffusion of Co and Fe than Zr and La (Figure 4.10). According to the EDS analysis, La and Co did not diffuse into the substrate (Table 4.1).

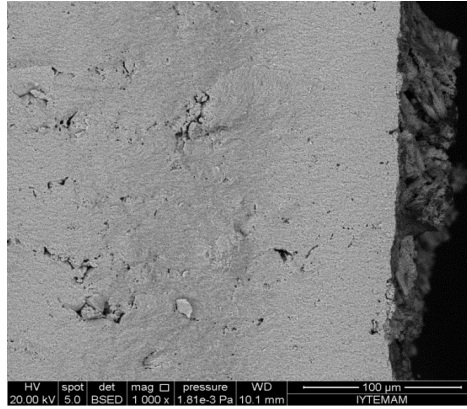


Figure 4.9. SEM image of the interface between  $\text{La}(\text{NO}_3)_3 \cdot 6\text{H}_2\text{O} + \text{Co}(\text{NO}_3)_2 \cdot 6\text{H}_2\text{O} + \text{Fe}(\text{NO}_3)_3 \cdot 9\text{H}_2\text{O}$  mixture and Zirconia pellets after heat treatment.

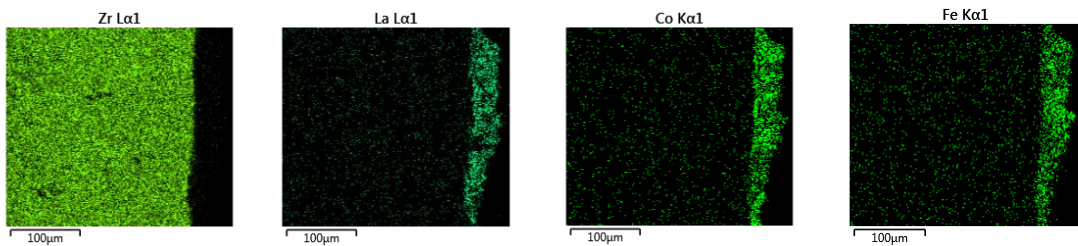


Figure 4.10. Mapping analysis of the interface between  $\text{La}(\text{NO}_3)_3 \cdot 6\text{H}_2\text{O} + \text{Co}(\text{NO}_3)_2 \cdot 6\text{H}_2\text{O} + \text{Fe}(\text{NO}_3)_3 \cdot 9\text{H}_2\text{O}$  mixture and Zirconia pellets after heat treatment.

The salt mixture of  $\text{SrCl}_2 \cdot 6\text{H}_2\text{O} + \text{Co}(\text{NO}_3)_2 \cdot 6\text{H}_2\text{O} + \text{Fe}(\text{NO}_3)_3 \cdot 9\text{H}_2\text{O}$  (also coded as S+C+F) showed limited diffusion of Zr and comparatively faster diffusion of Sr, Co and Fe across the interface (Figure 4.12). In addition, the distribution ratio into the substrate of Fe (0.04) and Co (0.02) were higher than Sr (Table 4.1).

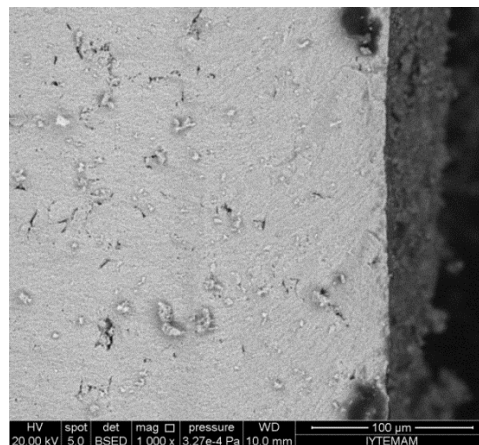


Figure 4.11. SEM image of the interface between  $\text{SrCl}_2 \cdot 6\text{H}_2\text{O} + \text{Co}(\text{NO}_3)_2 \cdot 6\text{H}_2\text{O} + \text{Fe}(\text{NO}_3)_3 \cdot 9\text{H}_2\text{O}$  mixture and zirconia pellets after heat treatment.

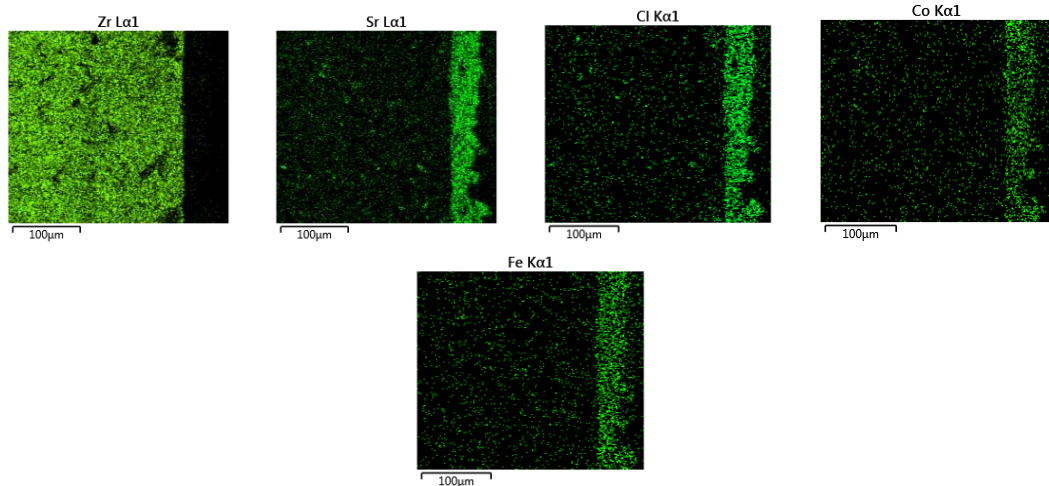


Figure 4.12. Mapping analysis of the interface between  $\text{SrCl}_2 \cdot 6\text{H}_2\text{O} + \text{Co}(\text{NO}_3)_2 \cdot 6\text{H}_2\text{O} + \text{Fe}(\text{NO}_3)_3 \cdot 9\text{H}_2\text{O}$  mixture and zirconia pellets after heat treatment.

The mixture of  $\text{La}(\text{NO}_3)_3 \cdot 6\text{H}_2\text{O} + \text{SrCl}_2 \cdot 6\text{H}_2\text{O} + \text{Co}(\text{NO}_3)_2 \cdot 6\text{H}_2\text{O} + \text{Fe}(\text{NO}_3)_3 \cdot 9\text{H}_2\text{O}$  (also coded as LSCF 6482) that was hoped to synthesize stoichiometric  $\text{La}_{0.6}\text{Sr}_{0.4}\text{Co}_{0.8}\text{Fe}_{0.2}\text{O}_3$  compound on top of zirconia via heating showed in the SEM micrograph (Figure 4.13) that the diffusion of Zr and Fe was limited at interface, while some diffusion of other elements into the substrate was observed in Figure 4.14. However, distribution ratio into the substrate of Sr was lowest rate (0.00) among of all LSCF elements according to EDS analysis in Table 4.1.

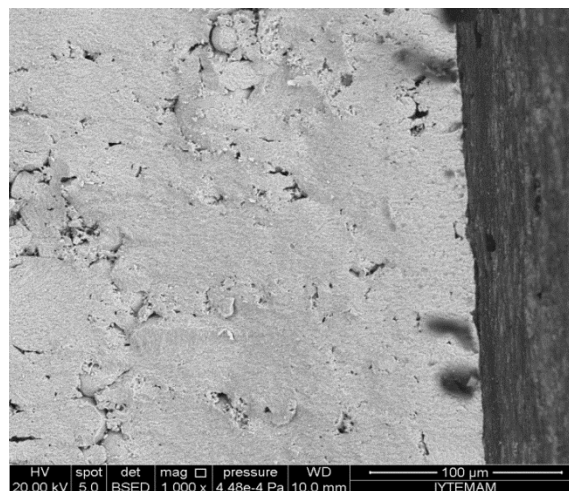


Figure 4.13. SEM image of the interface between  $\text{La}_{0.6}\text{Sr}_{0.4}\text{Co}_{0.8}\text{Fe}_{0.2}\text{O}_3$  mixture and zirconia pellets after heat treatment.

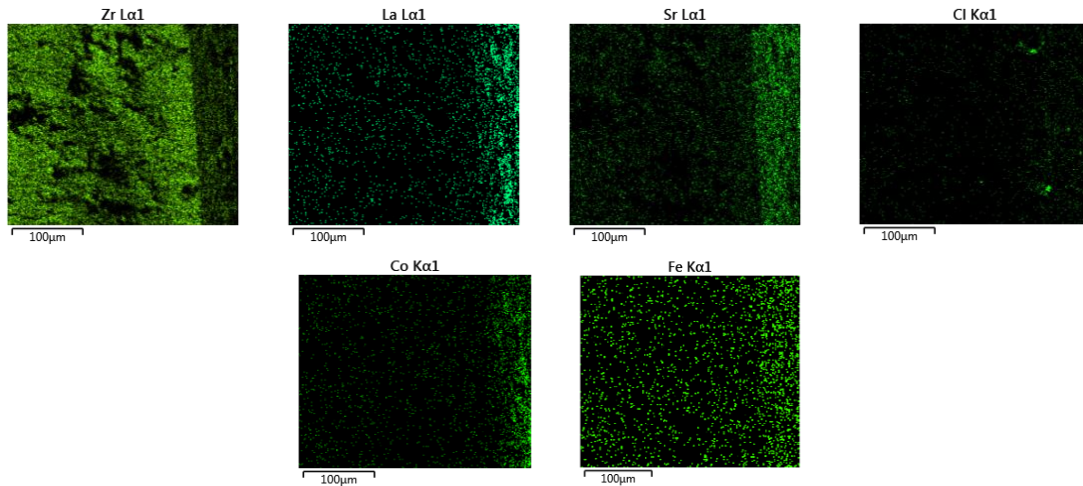


Figure 4.14. Mapping analysis of the interface between  $\text{La}_{0.6}\text{Sr}_{0.4}\text{Co}_{0.8}\text{Fe}_{0.2}\text{O}_3$  mixture and zirconia pellets after heat treatment.

The mixture of  $\text{La}(\text{NO}_3)_3 \cdot 6\text{H}_2\text{O} + \text{SrCl}_2 \cdot 6\text{H}_2\text{O} + \text{Co}(\text{NO}_3)_2 \cdot 6\text{H}_2\text{O} + \text{Fe}(\text{NO}_3)_3 \cdot 9\text{H}_2\text{O}$  (also coded as LSCF 6428) that was hoped to synthesize stoichiometric  $\text{La}_{0.6}\text{Sr}_{0.4}\text{Co}_{0.2}\text{Fe}_{0.8}\text{O}_3$  compound on top of zirconia via heating showed in Figure 4.15 that the diffusion of Zr and Fe was limited at the interface. The  $\text{La}_{0.6}\text{Sr}_{0.4}\text{Co}_{0.2}\text{Fe}_{0.8}\text{O}_3$  compound was observed not to form in the desired stoichiometry as was measured by XRD the results of which are presented in the foregoing sections. Some diffusion of other elements into the substrate was observed as shown in Figure 4.16. Sr ions appeared to diffuse faster than La, Co and Fe. However, distribution ratio into the substrate of Sr was lowest rate (0.00) among of all LSCF elements according to EDS analysis in Table 4.1.

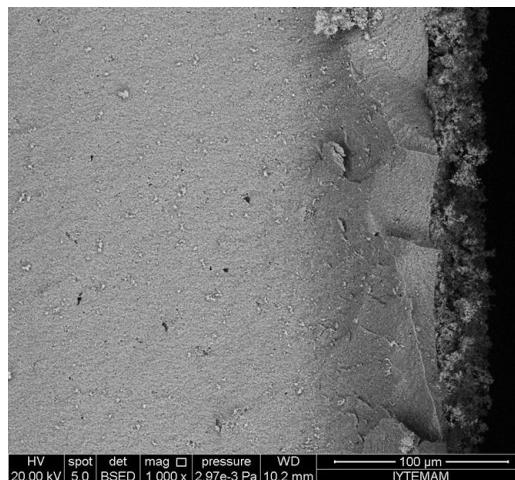


Figure 4.15. SEM image of the interface between  $\text{La}_{0.6}\text{Sr}_{0.4}\text{Co}_{0.2}\text{Fe}_{0.8}\text{O}_3$  mixture and zirconia pellets after heat treatment.

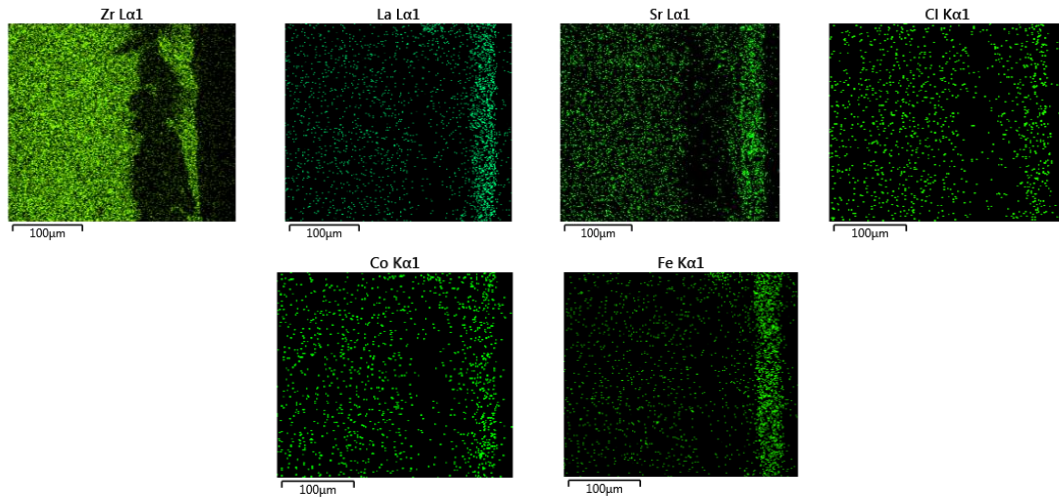


Figure 4.16. Mapping analysis of the interface between  $\text{La}_{0.6}\text{Sr}_{0.4}\text{Co}_{0.2}\text{Fe}_{0.8}\text{O}_3$  mixture and zirconia pellets after heat treatment.

#### 4.1.2.2. SEM and EDS Analysis of Heated CGO Electrolyte-Cathode Pair Samples

As was expected, according to the EDS analysis (Table 4.2) approximately 63-74% of the substrate was Ce and 7-9% of the substrate was composed of Gd (except 7th sample). Rest of the substrate consisted of elements which penetrated from the cathode layer into the substrate and oxygen. However, the precursor elements were observed to be unsurprisingly gathered in the cathode layer.

Table 4.2. EDS analysis results of heated sample pairs.

Pair codes	Ce (%)	Gd (%)	O (%)	La (%)	Sr (%)	Co (%)	Fe (%)	Cl (%)
1)L + C (substrate)	71.95	7.48	18.26	1.55	0.00	0.64	0.00	0.00
1) L + C (coating)	11.44	1.48	25.84	39.95	0.00	21.16	0.00	0.00
1)Distribution ratio	-	-	-	0.04	-	0.03	-	-
2)S + C (substrate)	71.85	9.78	14.31	0.00	2.52	0.20	0.00	1.34
2)S + C (coating)	5.07	0.87	9.51	0.00	46.40	0.13	0.00	38.15
2)Distribution ratio	-	-	-	-	0.05	1.54	-	-
3)F + C (substrate)	71.55	8.40	14.87	0.00	0.00	4.37	0.00	0.00
3)F + C (coating)	0.93	0.00	21.72	0.00	0.00	37.63	39.45	0.00
3)Distribution ratio	-	-	-	-	-	0.12	0.00	-
4)F + L (substrate)	68.61	7.84	23.31	0.00	0.00	0.00	0.15	0.00
4)F + L (coating)	1.95	0.00	19.21	53.30	0.00	0.00	25.45	0.09

(cont. on next page)

**Table 4.2 (cont.)**

4)Distribution ratio	-	-	-	0.00	-	-	0.01	-
5)F + S (substrate)	70.71	9.39	14.71	0.00	2.71	0.00	1.99	1.00
5)F + S (coating)	0.23	0.00	16.28	0.00	46.21	0.00	26.57	9.97
5)Distribution ratio	-	-	-	-	0.06	-	0.07	-
6)L+S+C+F substrate)	74.13	8.97	14.49	1.75	0.00	0.21	0.24	0.21
6)L+S+C+F (coating)	6.41	0.17	16.89	29.72	17.34	11.95	14.74	2.78
6)Distribution ratio	-	-	-	0.06	0.00	0.02	0.01	-
7)L+S+C (substrate)	17.02	2.25	21.87	0.26	41.53	0.00	0.00	17.07
7)L+S+C (coating)	0.86	0.16	18.60	41.43	23.05	1.83	0.00	14.07
7)Distribution ratio	-	-	-	0.01	1.80	0.00	-	-
8)L+C+F (substrate)	73.34	8.91	14.60	1.74	0.00	1.40	0.11	0.00
8)L+C+F (coating)	2.79	0.00	17.46	45.52	0.00	18.45	15.41	0.00
8)Distribution ratio	-	-	-	0.04	-	0.08	0.01	-
9)L+S (substrate)	68.52	8.07	14.37	4.41	2.96	0.00	0.00	1.31
9)L+S (coating)	2.04	0.00	14.28	70.92	9.21	0.00	0.00	3.55
9)Distribution ratio	-	-	-	0.06	0.32	-	-	-
10)L+S+F (substrate)	72.55	9.67	14.49	1.72	0.99	0.00	0.13	0.16
10)L+S+F (coating)	0.00	0.00	15.85	46.16	14.56	0.00	18.80	5.64
10)Distribution ratio	-	-	-	0.04	0.07	-	0.01	-
11)S+F+C (substrate)	63.87	8.62	25.09	0.00	0.75	0.78	0.63	0.25
11)S+F+C (coating)	2.96	0.80	19.05	0.00	31.01	22.85	22.87	0.45
11)Distribution ratio	-	-	-	-	0.02	0.03	0.03	-
12)LSCF 6482 (substrate)	74.43	8.45	14.55	0.61	0.74	0.74	0.26	0.24
12)LSCF 6482(coating)	1.33	0.10	17.05	38.81	15.91	17.13	8.91	0.77
12)Distribution ratio	-	-	-	0.01	0.05	0.04	0.03	-
13)LSCF 6428 (substrate)	49.60	6.34	16.22	5.21	4.98	3.69	13.75	0.20
13)LSCF 6428(substrate)	1.58	0.99	19.05	21.35	10.91	11.39	34.40	0.34
13)Distribution ratio	-	-	-	0.24	0.46	0.32	0.40	-

SEM micrographs of the interfaces between CGO electrolyte substrate and the salt mixtures were observed on the cross section after combination heat treatment at 800°C and 1050°C. Elemental mapping analysis showed the distribution of La, Sr, Co, Fe, Ce and Gd in the cathode and the electrolyte layers. Diffusion of species was observed in dot-map figures (Figures 4.18, 4.20, 4.22, 4.24, 4.26, 4.28 and 4.30). However, the distribution of Ce and Gd was not taken into much of consideration. As can be seen from the SEM images in Figures (4.17, 4.19, 4.21, 4.23, 4.25, 4.27 and 4.29),

most of the precursor mixtures generated a uniform and porous cathode layer all over the substrate by heat treatment. This is important for electrochemical reaction for oxygen reduction as mentioned before in Chapter 2.1.1.1.

The first pair studied was  $\text{La}(\text{NO}_3)_3 \cdot 6\text{H}_2\text{O} + \text{Co}(\text{NO}_3)_2 \cdot 6\text{H}_2\text{O}$  mixture (L+C), the second pair studied was  $\text{SrCl}_2 \cdot 6\text{H}_2\text{O} + \text{Co}(\text{NO}_3)_2 \cdot 6\text{H}_2\text{O}$  (S+C), the third pair studied was  $\text{Co}(\text{NO}_3)_2 \cdot 6\text{H}_2\text{O} + \text{Fe}(\text{NO}_3)_3 \cdot 9\text{H}_2\text{O}$  (C+F) mixture, the fourth pair studied was the mixture of  $\text{La}(\text{NO}_3)_3 \cdot 6\text{H}_2\text{O} + \text{Fe}(\text{NO}_3)_3 \cdot 9\text{H}_2\text{O}$  (L+F), the fifth pair studied was  $\text{SrCl}_2 \cdot 6\text{H}_2\text{O} + \text{Fe}(\text{NO}_3)_3 \cdot 9\text{H}_2\text{O}$  mixture and the eleventh combination studied was the mixture of  $\text{SrCl}_2 \cdot 6\text{H}_2\text{O} + \text{Co}(\text{NO}_3)_2 \cdot 6\text{H}_2\text{O} + \text{Fe}(\text{NO}_3)_3 \cdot 9\text{H}_2\text{O}$  heated on top of CGO. Results of the pairs were explained in the Appendix B.

The mixture of  $\text{La}(\text{NO}_3)_3 \cdot 6\text{H}_2\text{O} + \text{SrCl}_2 \cdot 6\text{H}_2\text{O} + \text{Co}(\text{NO}_3)_2 \cdot 6\text{H}_2\text{O} + \text{Fe}(\text{NO}_3)_3 \cdot 9\text{H}_2\text{O}$  in 1:1:1:1 molar ratio, heated on top of CGO indicated limited diffusion of Ce and Gd at the interface (Figure 4.18). Distribution ratio of the La was highest among all LSCF elements with regard to EDS analysis in Table 4.2.

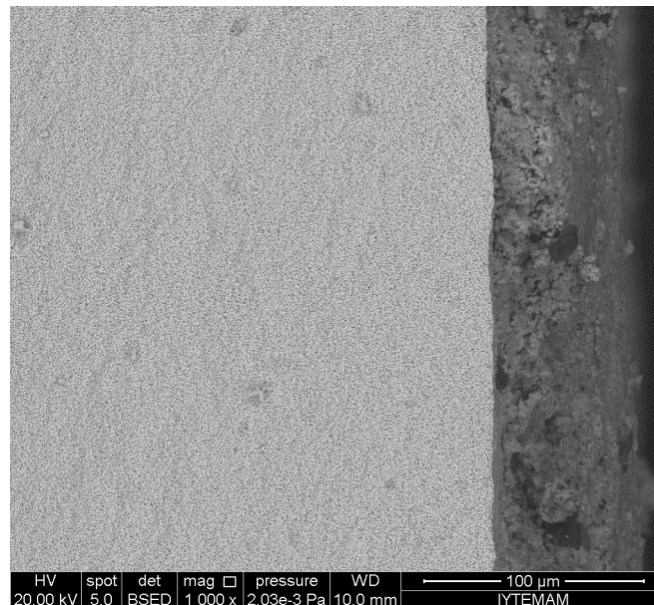


Figure 4.17. SEM image of the interface between  $\text{La}(\text{NO}_3)_3 \cdot 6\text{H}_2\text{O} + \text{SrCl}_2 \cdot 6\text{H}_2\text{O} + \text{Co}(\text{NO}_3)_2 \cdot 6\text{H}_2\text{O} + \text{Fe}(\text{NO}_3)_3 \cdot 9\text{H}_2\text{O}$  mixture and CGO pellets after heat treatment.

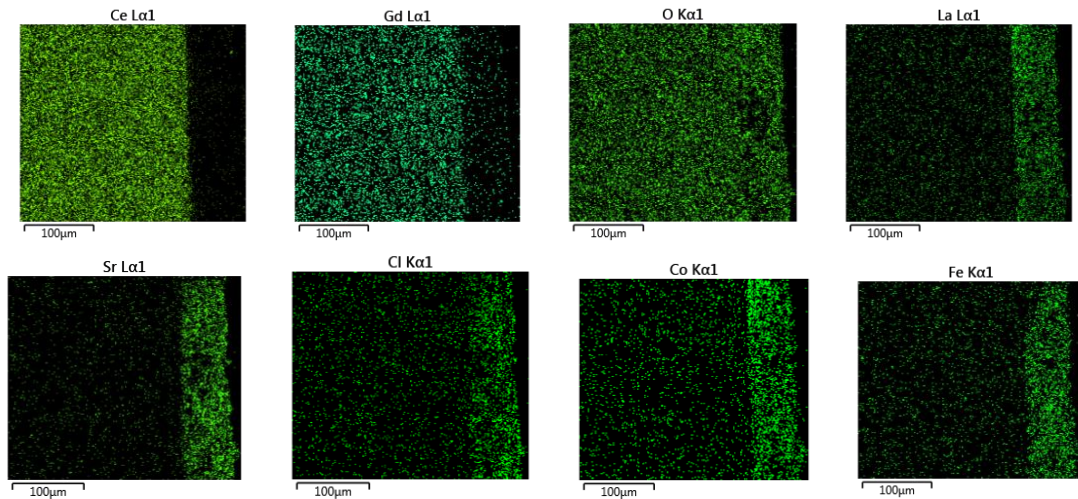


Figure 4.18. Mapping analysis of the interface between  $\text{La}(\text{NO}_3)_3 \cdot 6\text{H}_2\text{O} + \text{SrCl}_2 \cdot 6\text{H}_2\text{O} + \text{Co}(\text{NO}_3)_2 \cdot 6\text{H}_2\text{O} + \text{Fe}(\text{NO}_3)_3 \cdot 9\text{H}_2\text{O}$  mixture and CGO pellets after heat treatment.

The mixture of  $\text{La}(\text{NO}_3)_3 \cdot 6\text{H}_2\text{O} + \text{SrCl}_2 \cdot 6\text{H}_2\text{O} + \text{Co}(\text{NO}_3)_2 \cdot 6\text{H}_2\text{O}$ , heated on top of CGO showed limited diffusion of La ions across the interface based on EDS analysis (Figure 4.20 and Table 4.2). Sr appeared to well diffuse into the substrate as measured by EDS analysis (Table 4.2).

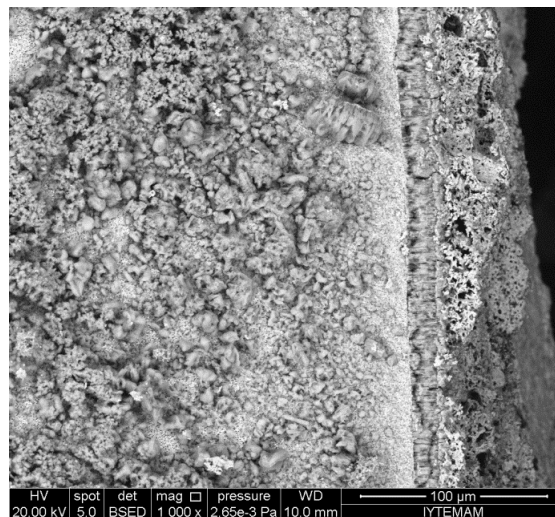


Figure 4.19. SEM image of the interface between  $\text{La}(\text{NO}_3)_3 \cdot 6\text{H}_2\text{O} + \text{SrCl}_2 \cdot 6\text{H}_2\text{O} + \text{Co}(\text{NO}_3)_2 \cdot 6\text{H}_2\text{O}$  mixture and CGO pellets after heat treatment.

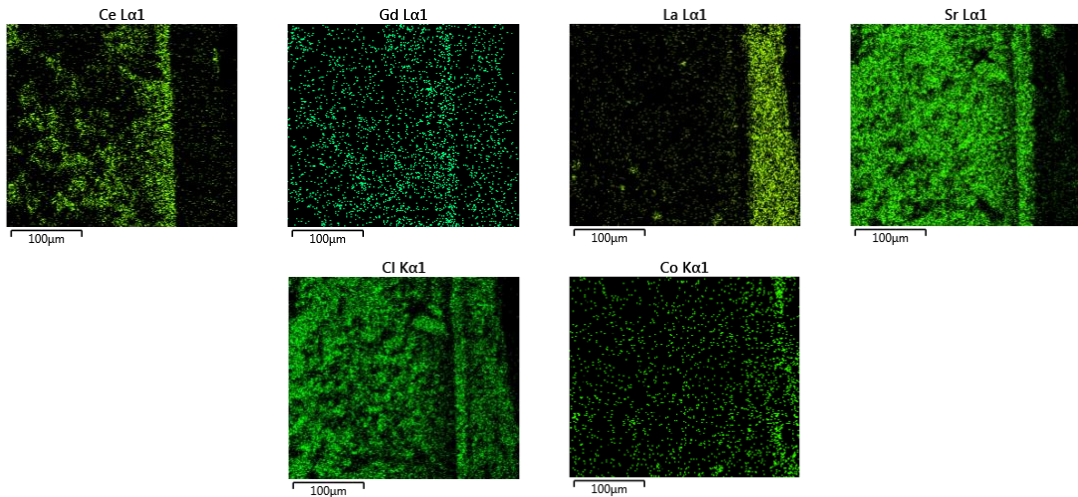


Figure 4.20. Mapping analysis of the interface between  $\text{La}(\text{NO}_3)_3 \cdot 6\text{H}_2\text{O} + \text{SrCl}_2 \cdot 6\text{H}_2\text{O} + \text{Co}(\text{NO}_3)_2 \cdot 6\text{H}_2\text{O}$  mixture and CGO pellets after heat treatment.

The EDS analysis of the sample of the mixture of  $\text{La}(\text{NO}_3)_3 \cdot 6\text{H}_2\text{O} + \text{Co}(\text{NO}_3)_2 \cdot 6\text{H}_2\text{O} + \text{Fe}(\text{NO}_3)_3 \cdot 9\text{H}_2\text{O}$  heated on top of CGO showed that all elements diffused well into the counter layer. Especially, La and Co had significant distribution ratio into the CGO substrate (Table 4.2).

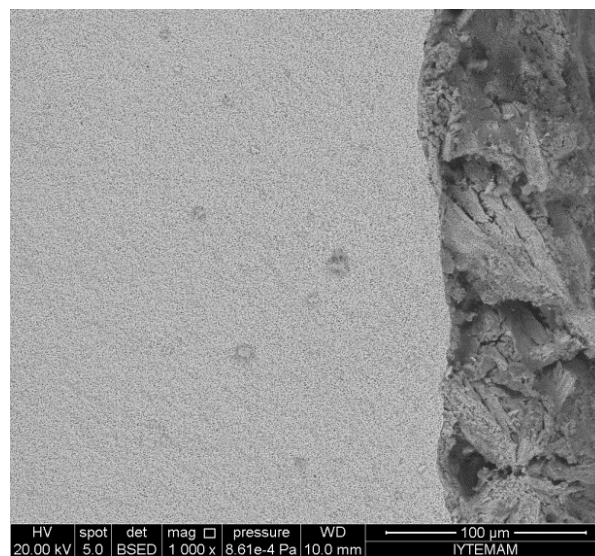


Figure 4.21. SEM image of the interface between  $\text{La}(\text{NO}_3)_3 \cdot 6\text{H}_2\text{O} + \text{Co}(\text{NO}_3)_2 \cdot 6\text{H}_2\text{O} + \text{Fe}(\text{NO}_3)_3 \cdot 9\text{H}_2\text{O}$  mixture and CGO pellets after heat treatment.

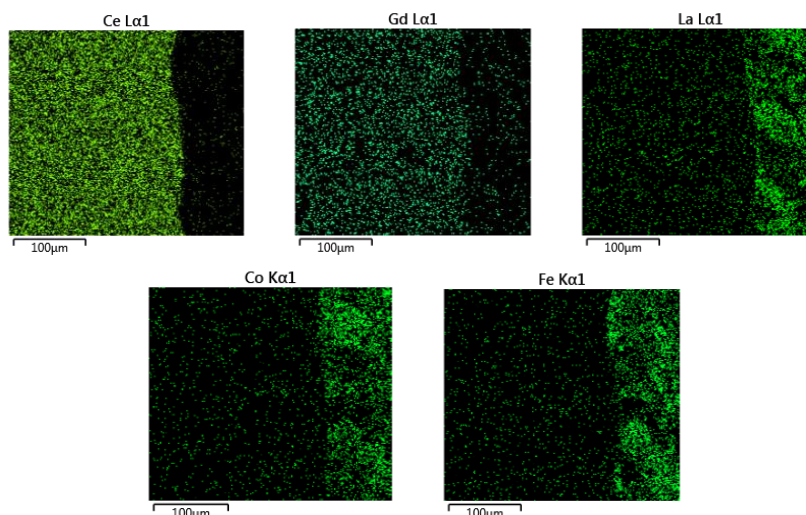


Figure 4.22. Mapping analysis of the interface between  $\text{La}(\text{NO}_3)_3 \cdot 6\text{H}_2\text{O}$  +  $\text{Co}(\text{NO}_3)_2 \cdot 6\text{H}_2\text{O}$  +  $\text{Fe}(\text{NO}_3)_3 \cdot 9\text{H}_2\text{O}$  mixture and CGO pellets after heat treatment.

The EDS analysis of the mixture of  $\text{La}(\text{NO}_3)_3 \cdot 6\text{H}_2\text{O}$  +  $\text{SrCl}_2 \cdot 6\text{H}_2\text{O}$  heated on top of CGO (Figure 4.23 and 4.24 and Table 4.2) indicated that all elements had some diffusion to each other. Dot-maps in Figure 4.48 indicated that along interface between the cathode and the electrolyte layers Sr significantly deposited and formed a Sr-rich interlayer. This was thought to occur by melting of the Sr salt during heating and the formation of the Sr-rich oxide along the interface (Table 4.2).

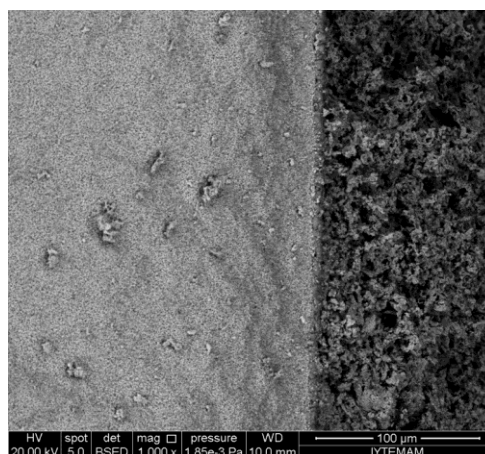


Figure 4.23. SEM image of the interface between  $\text{La}(\text{NO}_3)_3 \cdot 6\text{H}_2\text{O}$  +  $\text{SrCl}_2 \cdot 6\text{H}_2\text{O}$  mixture and CGO pellets after heat treatment.

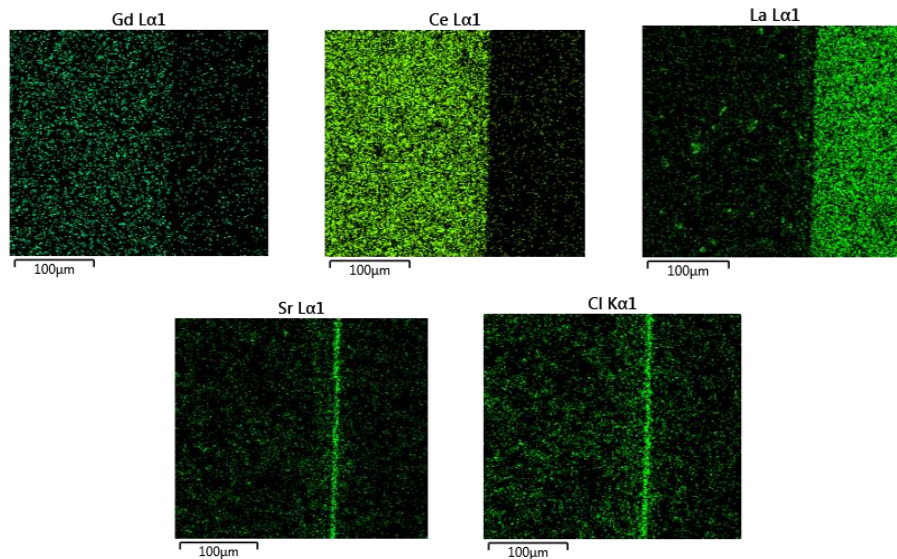


Figure 4.24. Mapping analysis of interface between  $\text{La}(\text{NO}_3)_3 \cdot 6\text{H}_2\text{O} + \text{SrCl}_2 \cdot 6\text{H}_2\text{O}$  mixture and CGO pellets after heat treatment.

The EDS analysis of the interface between the mixture of  $\text{La}(\text{NO}_3)_3 \cdot 6\text{H}_2\text{O} + \text{SrCl}_2 \cdot 6\text{H}_2\text{O} + \text{Fe}(\text{NO}_3)_3 \cdot 9\text{H}_2\text{O}$  heated on top of CGO indicated that all elements had some diffusion into the substrate from the cathode layer (Figure 4.26 and Table 4.2). Sr ions appeared to diffuse faster into the substrate than both La and Fe ions (Table 4.2).

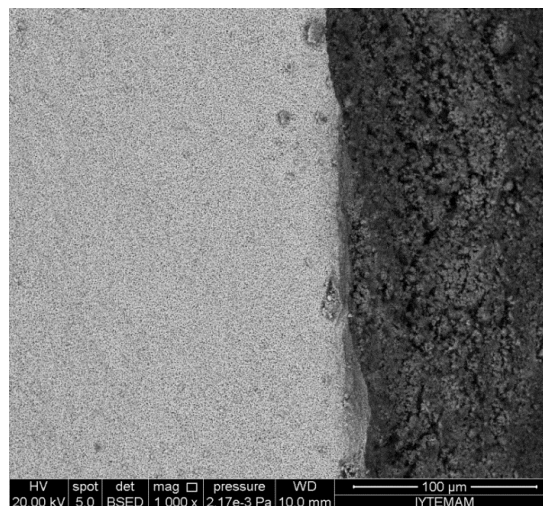


Figure 4.25. SEM image of the interface between  $\text{La}(\text{NO}_3)_3 \cdot 6\text{H}_2\text{O} + \text{SrCl}_2 \cdot 6\text{H}_2\text{O} + \text{Fe}(\text{NO}_3)_2 \cdot 9\text{H}_2\text{O}$  mixture and CGO pellets after heat treatment.

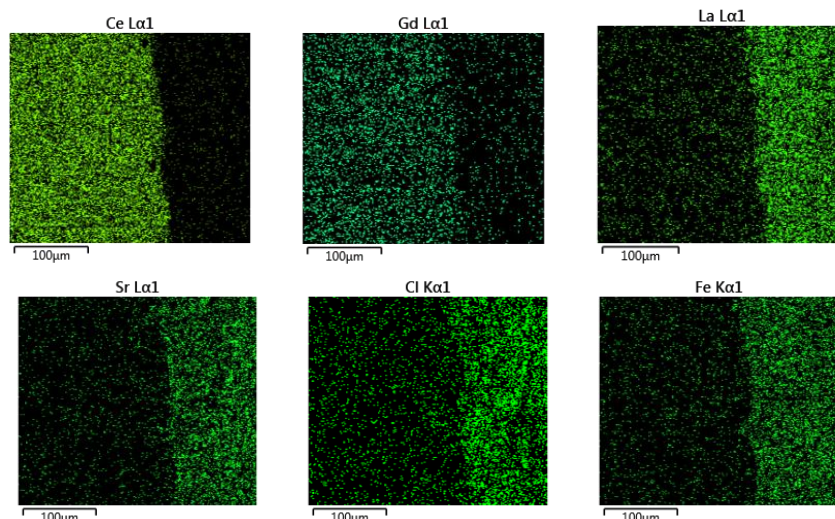


Figure 4.26. Mapping analysis of interface between  $\text{La}(\text{NO}_3)_3 \cdot 6\text{H}_2\text{O} + \text{SrCl}_2 \cdot 6\text{H}_2\text{O} + \text{Fe}(\text{NO}_3)_2 \cdot 9\text{H}_2\text{O}$  mixture and CGO pellets after heat treatment.

The mixture of  $\text{La}(\text{NO}_3)_3 \cdot 6\text{H}_2\text{O} + \text{SrCl}_2 \cdot 6\text{H}_2\text{O} + \text{Co}(\text{NO}_3)_2 \cdot 6\text{H}_2\text{O} + \text{Fe}(\text{NO}_3)_3 \cdot 9\text{H}_2\text{O}$  that was hoped to synthesize stoichiometric  $\text{La}_{0.6}\text{Sr}_{0.4}\text{Co}_{0.8}\text{Fe}_{0.2}\text{O}_3$  compound on top of CGO via heating was analyzed by EDS (Table 4.2). Some diffusion of all elements into the substrate was observed in Figure 4.28. XRD chart of this sample confirmed that stoichiometric  $\text{La}_{0.6}\text{Sr}_{0.4}\text{Co}_{0.8}\text{Fe}_{0.2}\text{O}_3$  was formed because of low distribution ratio of elements into the substrate, as expected (Figure 4.28).

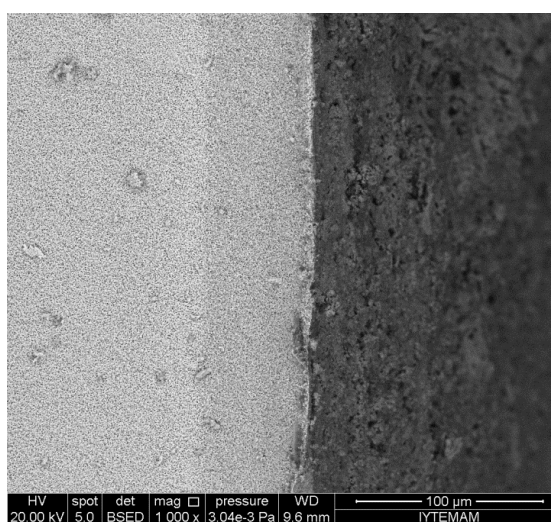


Figure 4.27. SEM image of the interface between  $\text{La}_{0.6}\text{Sr}_{0.4}\text{Co}_{0.8}\text{Fe}_{0.2}\text{O}_3$  mixture and CGO pellets after heat treatment.

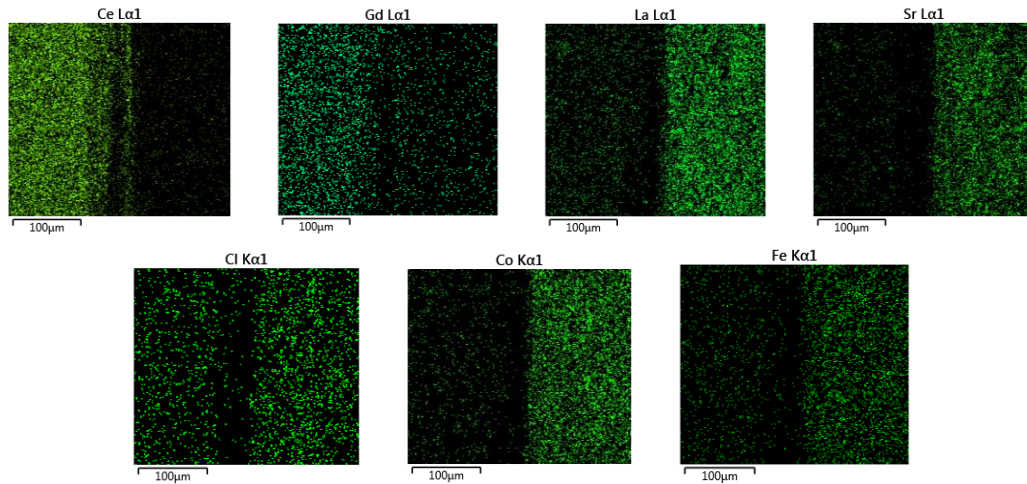


Figure 4.28. Mapping analysis of the interface between  $\text{La}_{0.6}\text{Sr}_{0.4}\text{Co}_{0.8}\text{Fe}_{0.2}\text{O}_3$  mixture and CGO pellets after heat treatment.

The mixture of  $\text{La}(\text{NO}_3)_3 \cdot 6\text{H}_2\text{O} + \text{SrCl}_2 \cdot 6\text{H}_2\text{O} + \text{Co}(\text{NO}_3)_2 \cdot 6\text{H}_2\text{O} + \text{Fe}(\text{NO}_3)_3 \cdot 9\text{H}_2\text{O}$  that was hoped to synthesize stoichiometric  $\text{La}_{0.6}\text{Sr}_{0.4}\text{Co}_{0.2}\text{Fe}_{0.8}\text{O}_3$  compound on top of CGO via heating failed to produce the LSCF compound with expected stoichiometry. All elements had significantly high distribution ratio which resulted in considerable material transport across the interface leading to failed formation of the expected LSCF (6428) compound.

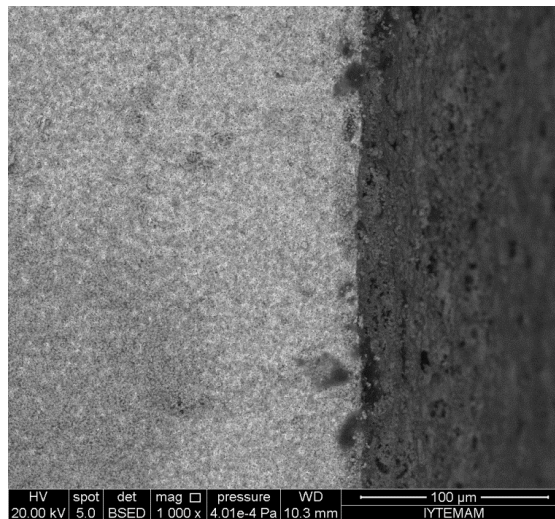


Figure 4.29. SEM image of the interface between  $\text{La}_{0.6}\text{Sr}_{0.4}\text{Co}_{0.2}\text{Fe}_{0.8}\text{O}_3$  mixture and CGO pellets after heat treatment.

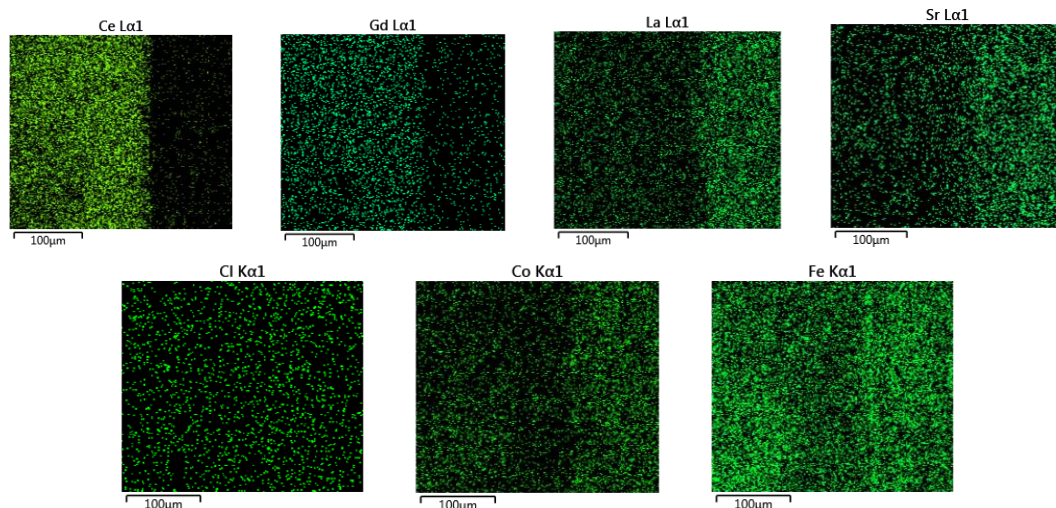


Figure 4.30. Mapping analysis of the interface between  $\text{La}_{0.6}\text{Sr}_{0.4}\text{Co}_{0.2}\text{Fe}_{0.8}\text{O}_3$  mixture and CGO pellets after heat treatment.

## 4.2. X-Ray Diffraction Analysis

In this section, the results of XRD analyses of as-received and heated mixture salt samples are presented. XRD analyses were performed on the latter to investigate structural changes caused by temperature.

### 4.2.1. XRD Analysis of As-Received Precursor Salts

Salt samples were analyzed for their crystalline structures using XRD method. The results are given below.

Figures 4.31 to 4.34 present the XRD patterns of as-received LSCF precursor salts. It can be seen that the first three precursors (salts of La, Sr and Co) unsurprisingly showed their labeled structures as desired. However, the structure of  $\text{Fe}(\text{NO}_3)_3 \cdot 9\text{H}_2\text{O}$  could not be identified. XRD measurement of this sample was repeated multiple number of times without success. Sample was observed to start to flow like a liquid during ‘mortar and pellet’ handling before the XRD analysis.

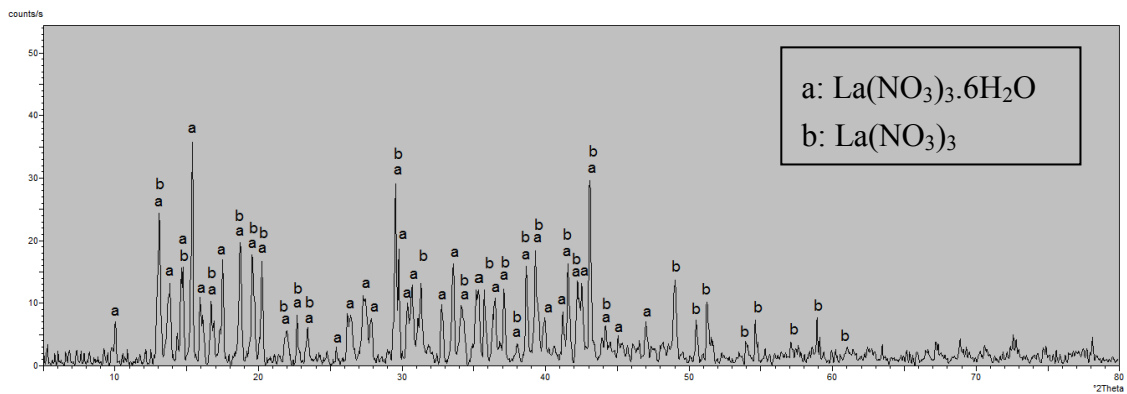


Figure 4.31. XRD chart for  $\text{La}(\text{NO}_3)_3 \cdot 6\text{H}_2\text{O}$

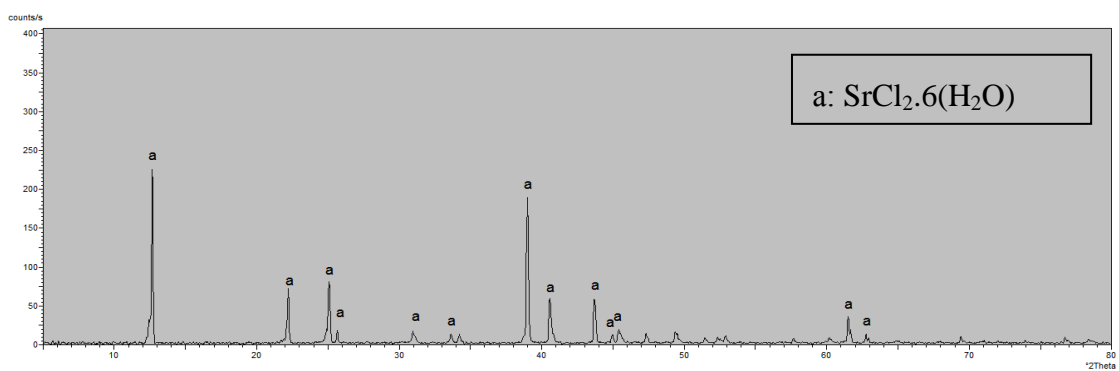


Figure 4.32. XRD chart for  $\text{SrCl}_2 \cdot 6\text{H}_2\text{O}$

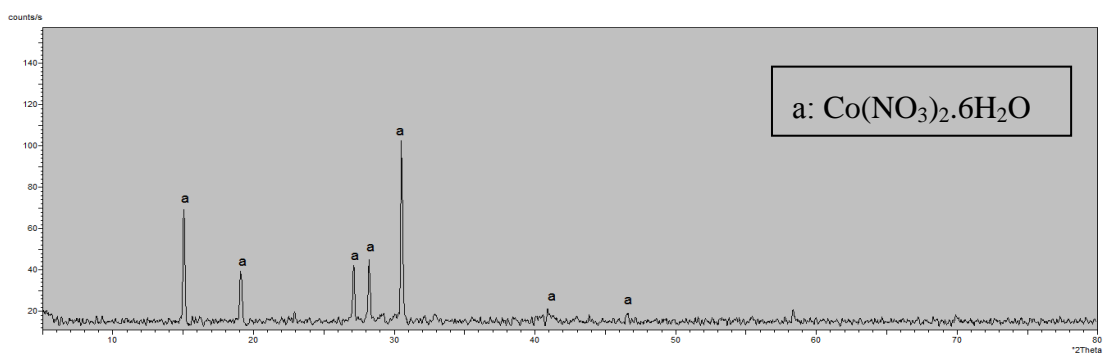


Figure 4.33. XRD chart for  $\text{Co}(\text{NO}_3)_2 \cdot 6\text{H}_2\text{O}$

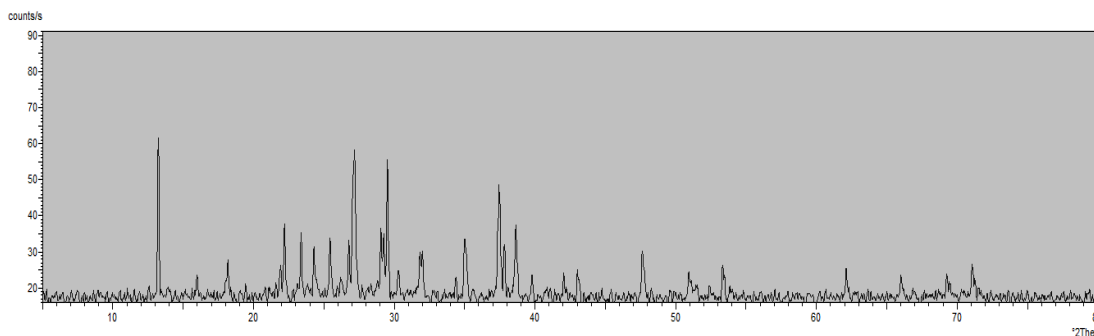


Figure 4.34. XRD chart for  $\text{Fe}(\text{NO}_3)_3 \cdot 9\text{H}_2\text{O}$

## 4.2.2. XRD Analysis of Mixture of Precursor Salts

XRD charts of as-synthesized mixtures were obtained from samples that were dried at  $55^\circ\text{C}$  in an oven. The profiles presented characteristic peaks of the salts compounds as expected.

Figure 4.35 presents the XRD patterns of mixture of  $\text{La}(\text{NO}_3)_3 \cdot 6\text{H}_2\text{O}$  +  $\text{Co}(\text{NO}_3)_2 \cdot 6\text{H}_2\text{O}$ . It can be seen that La and Co elements already started to react together even at these low temperatures.

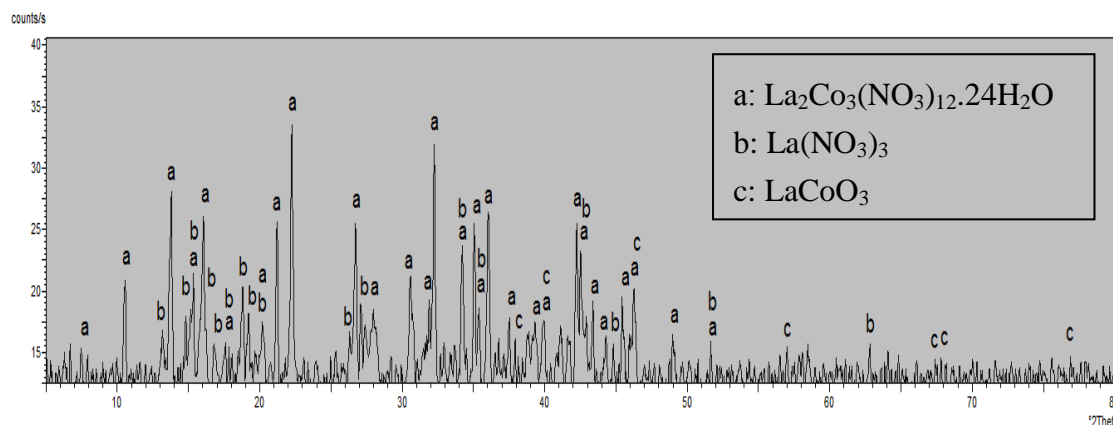


Figure 4.35. XRD chart for  $\text{La}(\text{NO}_3)_3 \cdot 6\text{H}_2\text{O}$  +  $\text{Co}(\text{NO}_3)_2 \cdot 6\text{H}_2\text{O}$  mixture

Figure 4.36 presents the XRD patterns of mixture of  $\text{SrCl}_2 \cdot 6\text{H}_2\text{O}$  +  $\text{Co}(\text{NO}_3)_2 \cdot 6\text{H}_2\text{O}$ . It can be seen that the two main elements of the precursor salts did not react with each other but their main phase was changed at  $55^\circ\text{C}$ . Interestingly, Sr and Co swapped their nitrate and chloride anions.

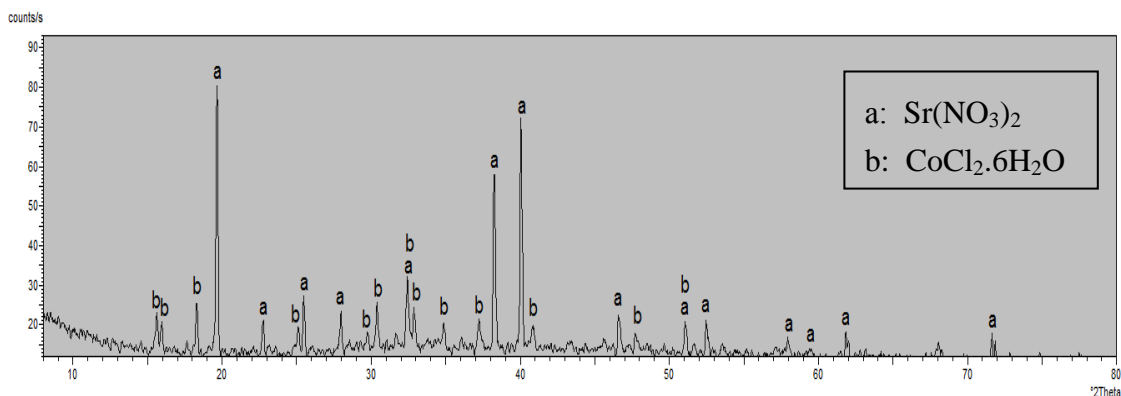


Figure 4.36. XRD chart for  $\text{SrCl}_2 \cdot 6\text{H}_2\text{O} + \text{Co}(\text{NO}_3)_2 \cdot 6\text{H}_2\text{O}$  mixture.

Figure 4.37 presents the XRD patterns of as-synthesized mixture of  $\text{Co}(\text{NO}_3)_2 \cdot 6\text{H}_2\text{O} + \text{Fe}(\text{NO}_3)_3 \cdot 9\text{H}_2\text{O}$ . Two precursor salts did not react with each other at  $55^\circ\text{C}$  and remained as received.

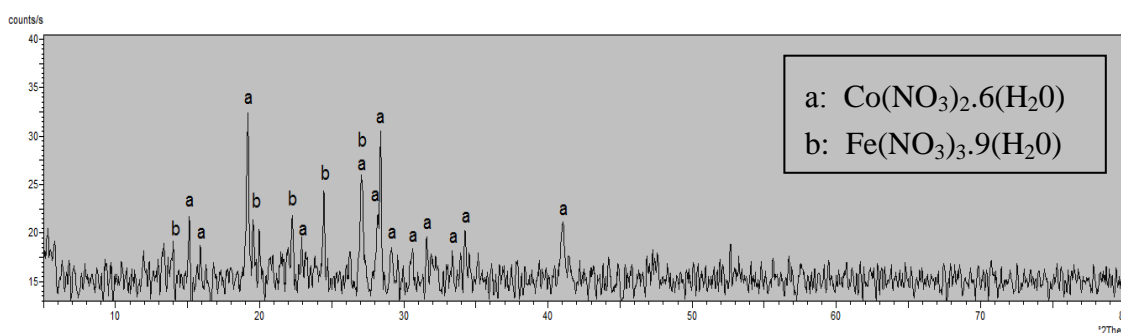


Figure 4.37. XRD chart for  $\text{Co}(\text{NO}_3)_2 \cdot 6\text{H}_2\text{O} + \text{Fe}(\text{NO}_3)_3 \cdot 9\text{H}_2\text{O}$  mixture.

The XRD patterns of  $\text{La}(\text{NO}_3)_3 \cdot 6\text{H}_2\text{O} + \text{Fe}(\text{NO}_3)_3 \cdot 9\text{H}_2\text{O}$  mixture shown that La and Fe elements already started to react together even at these low temperatures. Besides owing to the presence of  $\text{Fe}_2\text{O}_3$  the mixture was colored red.

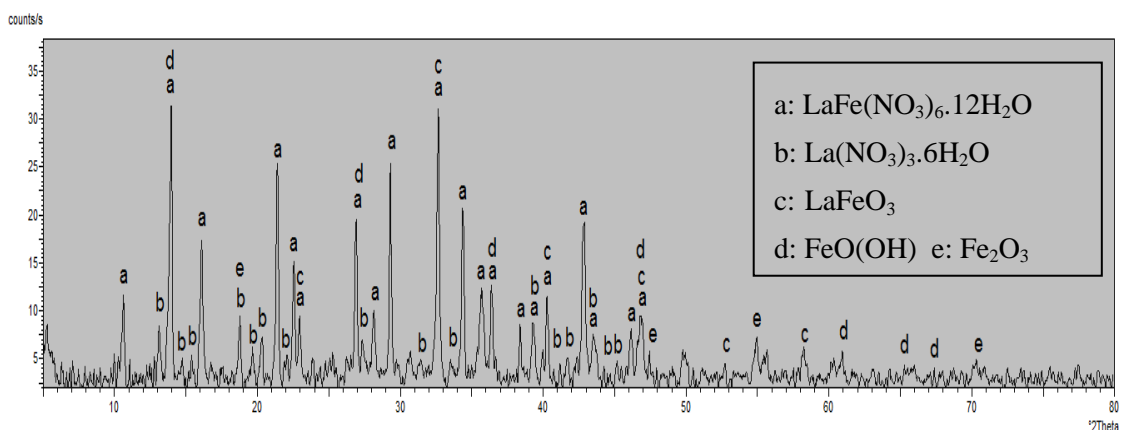


Figure 4.38. XRD chart for  $\text{La}(\text{NO}_3)_3 \cdot 6\text{H}_2\text{O} + \text{Fe}(\text{NO}_3)_3 \cdot 9\text{H}_2\text{O}$  as-synthesized mixture.

The XRD patterns of as-synthesized mixture of  $\text{SrCl}_2 \cdot 6\text{H}_2\text{O} + \text{Fe}(\text{NO}_3)_3 \cdot 9\text{H}_2\text{O}$  was shown in Figure 4.39. Two main elements of this mixture Fe and Sr did not react with each other at low temperature but they changed their initial structures.

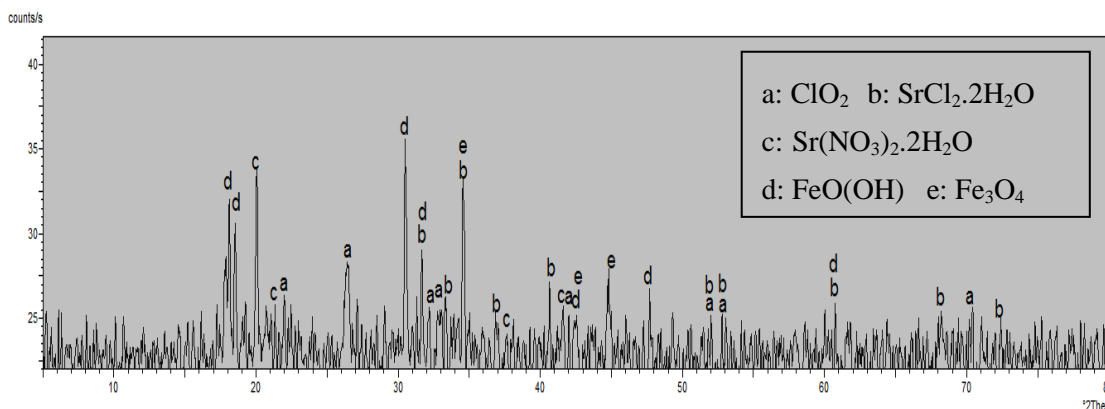


Figure 4.39. XRD chart for  $\text{SrCl}_2 \cdot 6\text{H}_2\text{O} + \text{Fe}(\text{NO}_3)_3 \cdot 9\text{H}_2\text{O}$  mixture.

XRD chart of  $\text{La}(\text{NO}_3)_3 \cdot 6\text{H}_2\text{O} + \text{SrCl}_2 \cdot 6\text{H}_2\text{O} + \text{Co}(\text{NO}_3)_2 \cdot 6\text{H}_2\text{O} + \text{Fe}(\text{NO}_3)_3 \cdot 9\text{H}_2\text{O}$  indicated that La-Fe and La-Co elements reacted together, respectively (Figure 4.40). However, Fe – Co did not react with each other and Sr did not react with any of the precursor salts at low temperature.

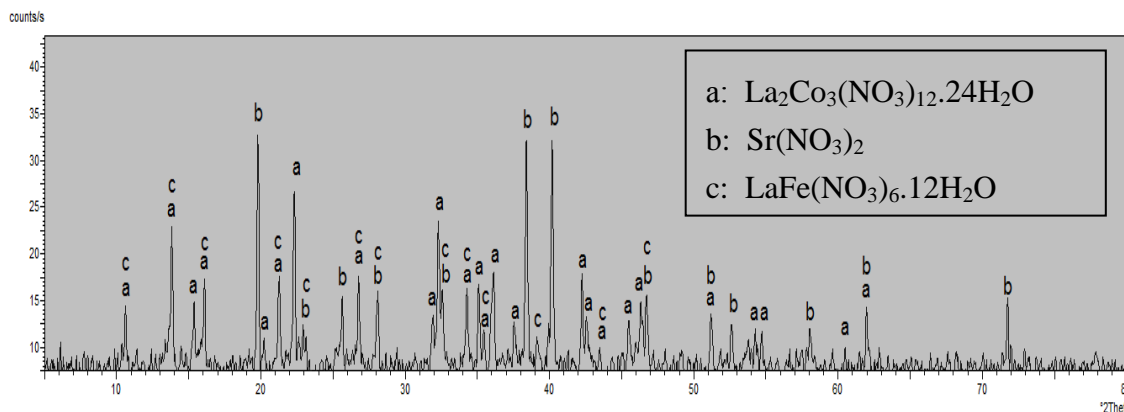


Figure 4.40. XRD chart for  $\text{La}(\text{NO}_3)_3 \cdot 6\text{H}_2\text{O} + \text{SrCl}_2 \cdot 6\text{H}_2\text{O} + \text{Co}(\text{NO}_3)_2 \cdot 6\text{H}_2\text{O} + \text{Fe}(\text{NO}_3)_3 \cdot 9\text{H}_2\text{O}$  mixture.

Figure 4.41 presents the XRD patterns of mixture of  $\text{La}(\text{NO}_3)_3 \cdot 6\text{H}_2\text{O} + \text{SrCl}_2 \cdot 6\text{H}_2\text{O} + \text{Co}(\text{NO}_3)_2 \cdot 6\text{H}_2\text{O}$ . Although, La-Co elements already started to react together, Sr did not react with either La or Co at these low temperatures.

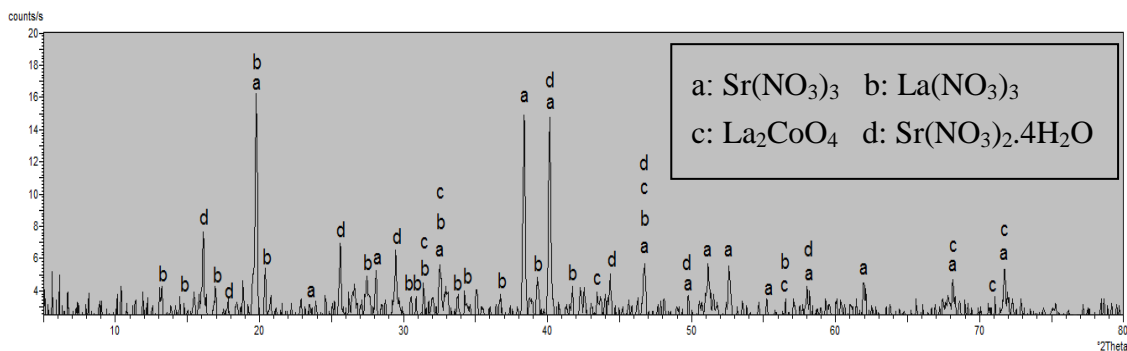


Figure 4.41. XRD chart for  $\text{La}(\text{NO}_3)_3 \cdot 6\text{H}_2\text{O} + \text{SrCl}_2 \cdot 6\text{H}_2\text{O} + \text{Co}(\text{NO}_3)_2 \cdot 6\text{H}_2\text{O}$  mixture.

The XRD patterns of mixture of  $\text{La}(\text{NO}_3)_3 \cdot 6\text{H}_2\text{O} + \text{Co}(\text{NO}_3)_2 \cdot 6\text{H}_2\text{O} + \text{Fe}(\text{NO}_3)_3 \cdot 9\text{H}_2\text{O}$  showed signs of low temperature reaction with each other. However, Fe did not react with any of the precursor salts at low temperature (Figure 4.42).

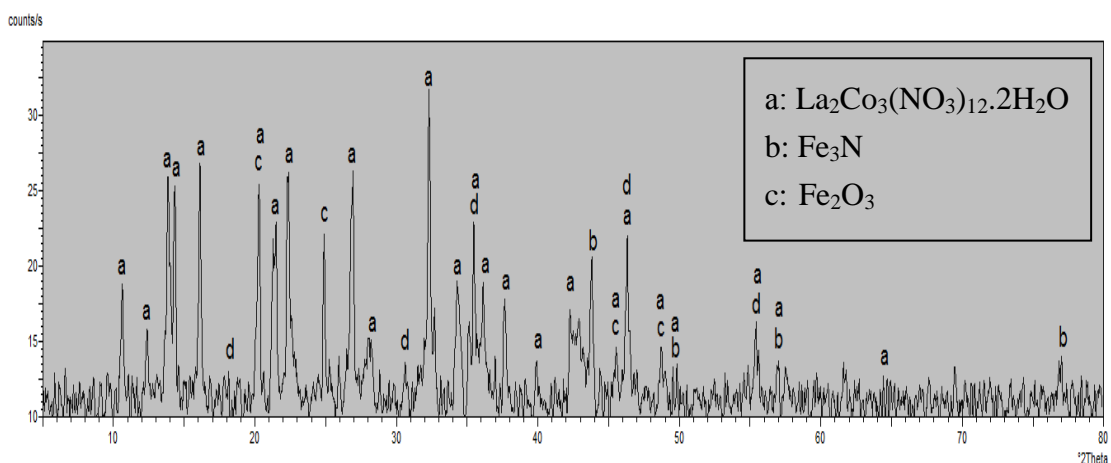


Figure 4.42. XRD chart for  $\text{La}(\text{NO}_3)_3 \cdot 6\text{H}_2\text{O} + \text{Co}(\text{NO}_3)_2 \cdot 6\text{H}_2\text{O} + \text{Fe}(\text{NO}_3)_3 \cdot 9\text{H}_2\text{O}$  mixture.

Sr did not react with La at low temperature, just like other samples, as evidenced in the XRD chart of  $\text{La}(\text{NO}_3)_3 \cdot 6\text{H}_2\text{O} + \text{SrCl}_2 \cdot 6\text{H}_2\text{O}$  mixture (Figure 4.43).

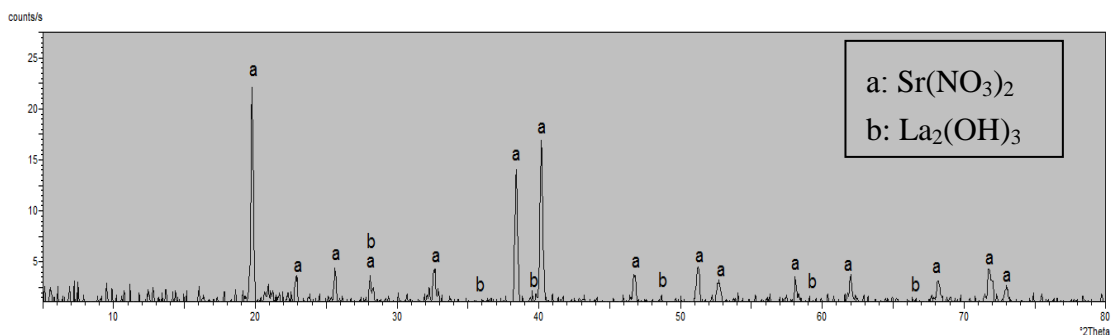


Figure 4.43. XRD chart for  $\text{La}(\text{NO}_3)_3 \cdot 6\text{H}_2\text{O} + \text{SrCl}_2 \cdot 6\text{H}_2\text{O}$  mixture.

The XRD patterns of as-synthesized mixture of  $\text{La}(\text{NO}_3)_3 \cdot 6\text{H}_2\text{O} + \text{SrCl}_2 \cdot 6\text{H}_2\text{O} + \text{Fe}(\text{NO}_3)_3 \cdot 9\text{H}_2\text{O}$  is shown in Figure 4.44. Unlike other samples, Sr element already started to react with La and Fe at low temperature.

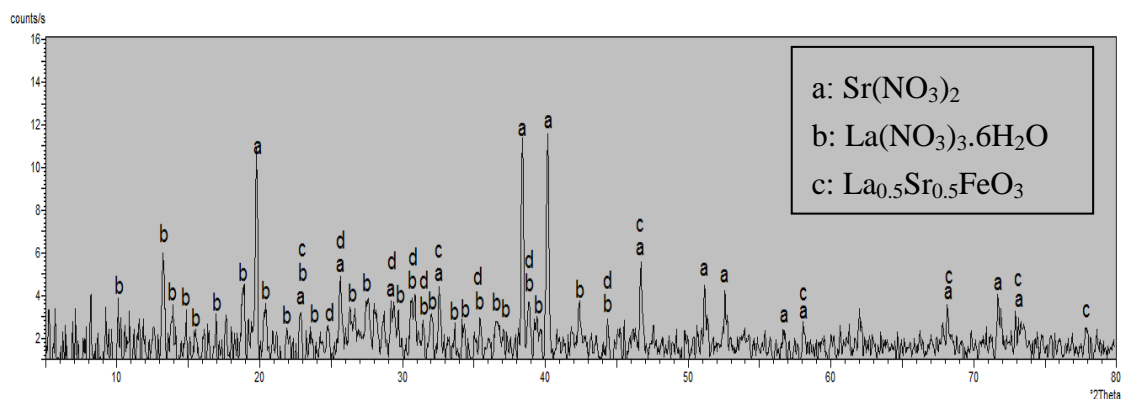


Figure 4.44. XRD chart for  $\text{La}(\text{NO}_3)_3 \cdot 6\text{H}_2\text{O} + \text{SrCl}_2 \cdot 6\text{H}_2\text{O} + \text{Fe}(\text{NO}_3)_3 \cdot 9\text{H}_2\text{O}$  mixture.

Figure 4.45 presents the XRD patterns of mixture of  $\text{SrCl}_2 \cdot 6\text{H}_2\text{O} + \text{Co}(\text{NO}_3)_2 \cdot 6\text{H}_2\text{O} + \text{Fe}(\text{NO}_3)_3 \cdot 9\text{H}_2\text{O}$ . Not much reaction occurred between the salts except for the exchange of Cl and  $\text{NO}_3$  between Sr and Fe salts.

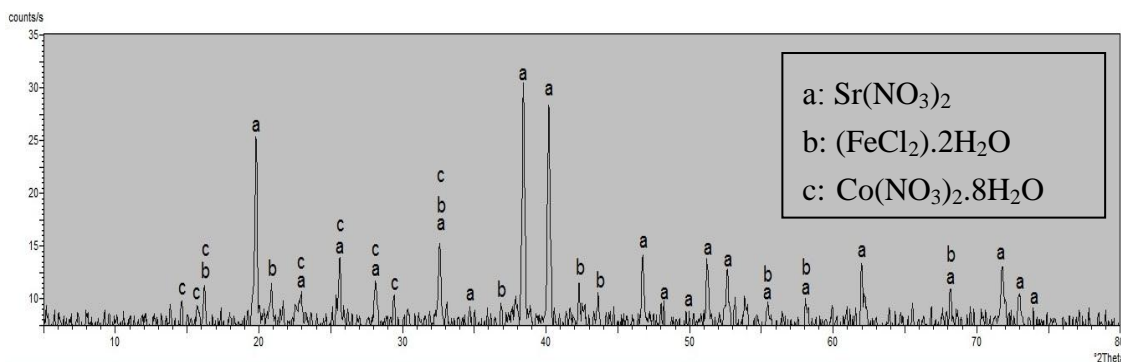


Figure 4.45. XRD chart for  $\text{SrCl}_2 \cdot 6\text{H}_2\text{O} + \text{Fe}(\text{NO}_3)_3 \cdot 9\text{H}_2\text{O} + \text{Co}(\text{NO}_3)_2 \cdot 6\text{H}_2\text{O}$  mixture.

Figure 4.46 presents the XRD patterns of the  $55^\circ\text{C}$  heat treated mixture of  $\text{La}(\text{NO}_3)_3 \cdot 6\text{H}_2\text{O} + \text{SrCl}_2 \cdot 6\text{H}_2\text{O} + \text{Co}(\text{NO}_3)_2 \cdot 6\text{H}_2\text{O} + \text{Fe}(\text{NO}_3)_3 \cdot 9\text{H}_2\text{O}$  which indicated that Sr already started to react with La and Fe to form a new phase ( $\text{La}_{0.6}\text{Sr}_{0.4}\text{FeO}_3$ ). La and Co elements reacted together to form another phase, and Fe and Co did not reach with each other like the previous samples at low temperature. Notice that despite the  $55^\circ\text{C}$  low temperature heating, a new compound ( $\text{La}_{0.6}\text{Sr}_{0.4}\text{FeO}_3$ ) was still able to form. Some of these salts were extremely reactive at low temperatures.

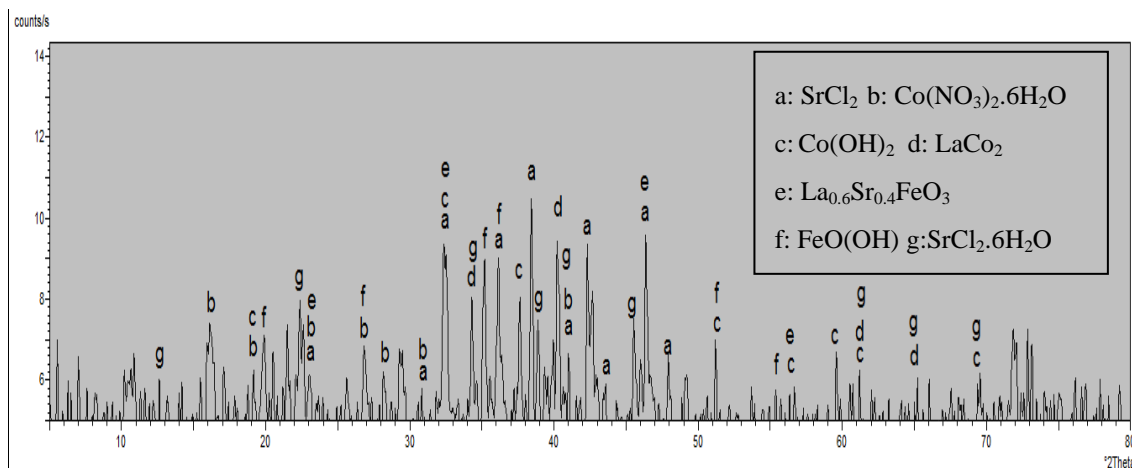


Figure 4.46. XRD chart for  $\text{La}_{0.6}\text{Sr}_{0.4}\text{Co}_{0.8}\text{Fe}_{0.2}\text{O}_3$  mixture.

Figure 4.47 presents the XRD patterns of the  $55^\circ\text{C}$  heat treated mixture of  $\text{La}(\text{NO}_3)_3 \cdot 6\text{H}_2\text{O} + \text{SrCl}_2 \cdot 6\text{H}_2\text{O} + \text{Co}(\text{NO}_3)_2 \cdot 6\text{H}_2\text{O} + \text{Fe}(\text{NO}_3)_3 \cdot 9\text{H}_2\text{O}$  which indicated that Sr element already started to react with La, Fe and Co to form a new compound ( $\text{La}_{0.6}\text{Sr}_{0.4}\text{Co}_{0.4}\text{Fe}_{0.6}\text{O}_3$ ) with a very close stoichiometry to the originally targeted 6428 phase.

The last two samples produced interesting results such that a final LSCF stoichiometric compound could be formed from these samples. But the final heat treatment at  $800^\circ\text{C}$  and  $1050^\circ\text{C}$  yielded surprising results.

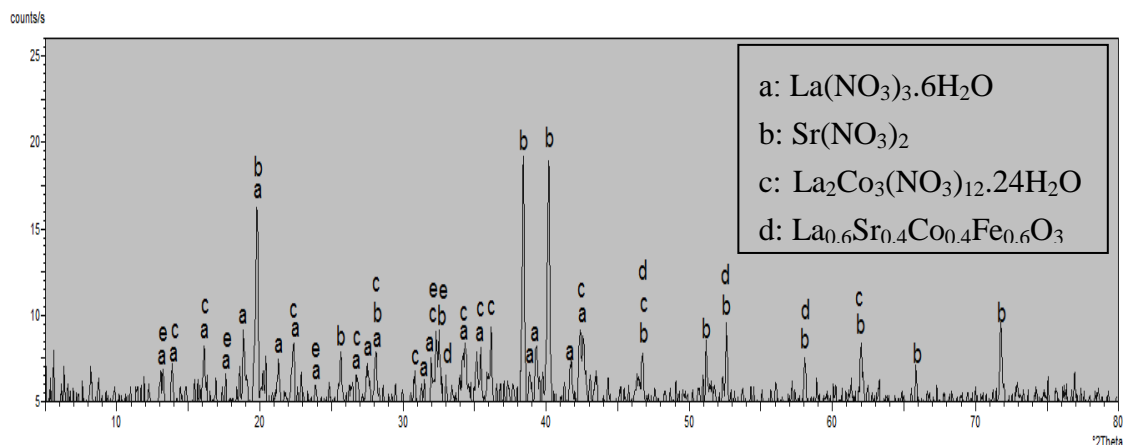


Figure 4.47. XRD chart for  $\text{La}_{0.6}\text{Sr}_{0.4}\text{Co}_{0.2}\text{Fe}_{0.8}\text{O}_3$  mixture.

### 4.2.3. XRD Analysis of Heated Precursor Salt Mixtures

XRD charts of as-synthesized mixtures that were heated in a furnace via a heating schedule as shown in Figure 3.6 are given in this section.

Figure 4.48 presents the XRD patterns of as-synthesized mixture of  $\text{La}(\text{NO}_3)_3 \cdot 6\text{H}_2\text{O} + \text{Co}(\text{NO}_3)_2 \cdot 6\text{H}_2\text{O}$ . It can be seen that La and Co elements completely reacted with each other to form  $\text{LaCoO}_3$ , besides EDS analysis confirmed this data too (Table 4.1).

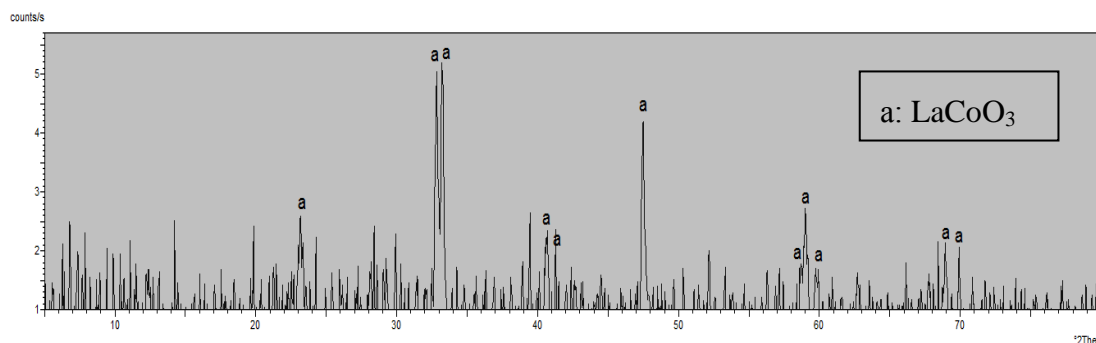


Figure 4.48. XRD chart for  $\text{La}(\text{NO}_3)_3 \cdot 6\text{H}_2\text{O} + \text{Co}(\text{NO}_3)_2 \cdot 6\text{H}_2\text{O}$  mixture after heat treatment.

The XRD patterns of as-synthesized mixture of  $\text{SrCl}_2 \cdot 6\text{H}_2\text{O} + \text{Co}(\text{NO}_3)_2 \cdot 6\text{H}_2\text{O}$  indicated that Sr and Co elements did not react with each other. Absence of Sr containing mineral in the XRD chart can be explained by the presence of Sr ions in solid solution in the  $\text{CoO}$  phase (Figure 4.49).

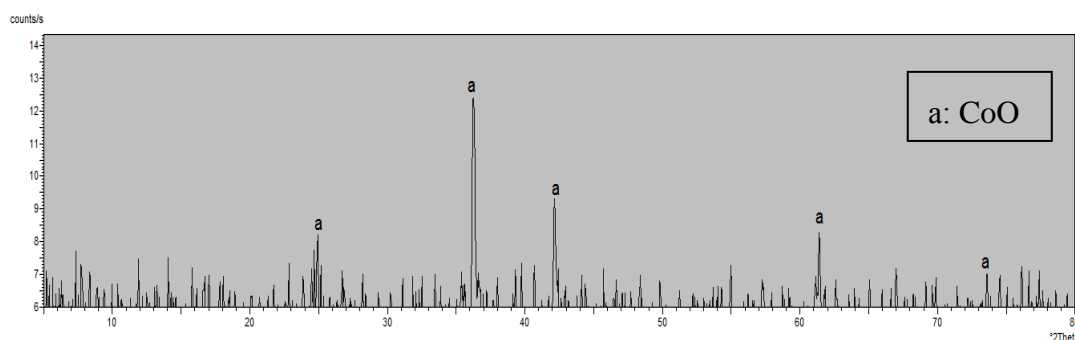


Figure 4.49. XRD chart for  $\text{SrCl}_2 \cdot 6\text{H}_2\text{O} + \text{Co}(\text{NO}_3)_2 \cdot 6\text{H}_2\text{O}$  mixture after heat treatment.

It can be seen from the XRD patterns of  $\text{Fe}(\text{NO}_3)_3 \cdot 9\text{H}_2\text{O} + \text{Co}(\text{NO}_3)_2 \cdot 6\text{H}_2\text{O}$  mixture that Co and Fe elements completely reacted with each other.

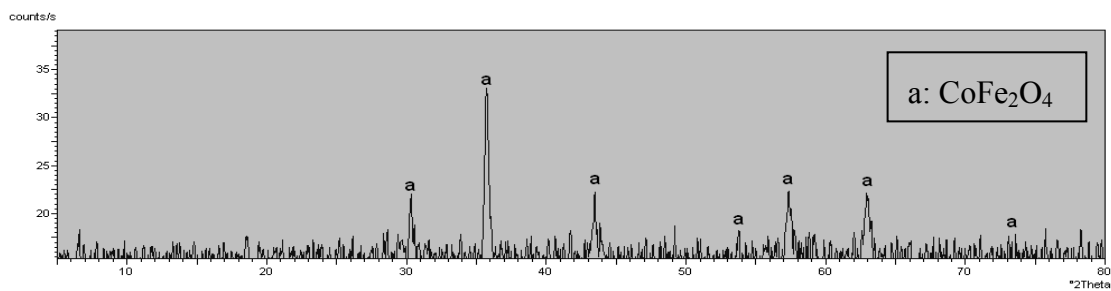


Figure 4.50. XRD chart for  $\text{Fe}(\text{NO}_3)_3 \cdot 9\text{H}_2\text{O} + \text{Co}(\text{NO}_3)_2 \cdot 6\text{H}_2\text{O}$  mixture after heat treatment

The XRD patterns of as-synthesized mixture of  $\text{La}(\text{NO}_3)_3 \cdot 6\text{H}_2\text{O} + \text{Fe}(\text{NO}_3)_2 \cdot 9\text{H}_2\text{O}$  shown in Figure 4.51. It can be seen that La and Fe elements completely reacted with each other by heat treatment, as desired.

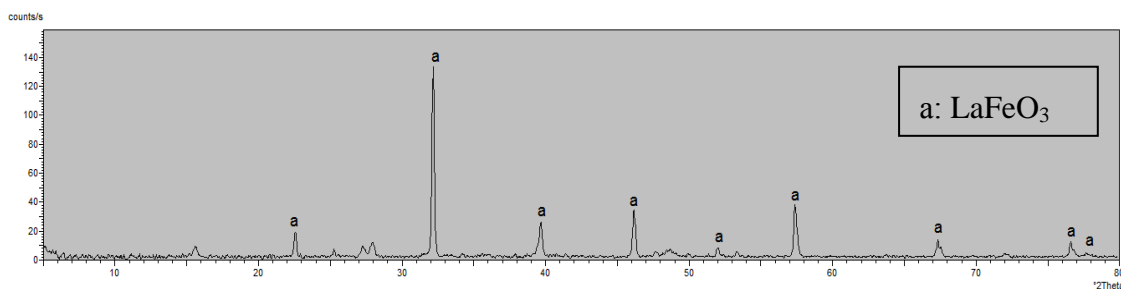


Figure 4.51. XRD chart for  $\text{La}(\text{NO}_3)_3 \cdot 6\text{H}_2\text{O} + \text{Fe}(\text{NO}_3)_3 \cdot 9\text{H}_2\text{O}$  mixture after heat treatment.

Figure 4.52 presents the XRD patterns of as-synthesized mixture of  $\text{SrCl}_2 \cdot 6\text{H}_2\text{O} + \text{Fe}(\text{NO}_3)_3 \cdot 9\text{H}_2\text{O}$ . It can be seen that Fe and Sr elements completely reacted in the solid state to form new phases.

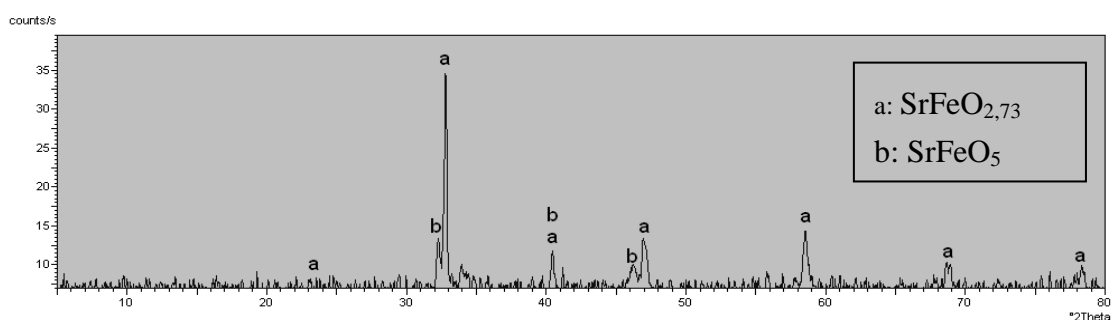


Figure 4.52. XRD chart for  $\text{SrCl}_2 \cdot 6\text{H}_2\text{O} + \text{Fe}(\text{NO}_3)_3 \cdot 9\text{H}_2\text{O}$  mixture after heat treatment.

Figure 4.53 presents the XRD patterns of as-synthesized mixture of  $\text{La}(\text{NO}_3)_3 \cdot 6\text{H}_2\text{O} + \text{SrCl}_2 \cdot 6\text{H}_2\text{O} + \text{Fe}(\text{NO}_3)_3 \cdot 9\text{H}_2\text{O} + \text{Co}(\text{NO}_3)_2 \cdot 6\text{H}_2\text{O}$ . The profile

presented characteristic peaks of  $\text{La}_{0.6}\text{Sr}_{0.4}\text{Co}_{0.1}\text{Fe}_{0.9}\text{O}_3$ . In spite of all elements were reacted with each other in one phase, mixture stoichiometric was not  $\text{LaSrCoFeO}_3$ , as desired. One of the reason of this stoichiometric changing was, distribution ratio of elements into the substrates via heating. Peaks were broader than expected, indicating a nano-sized crystal.

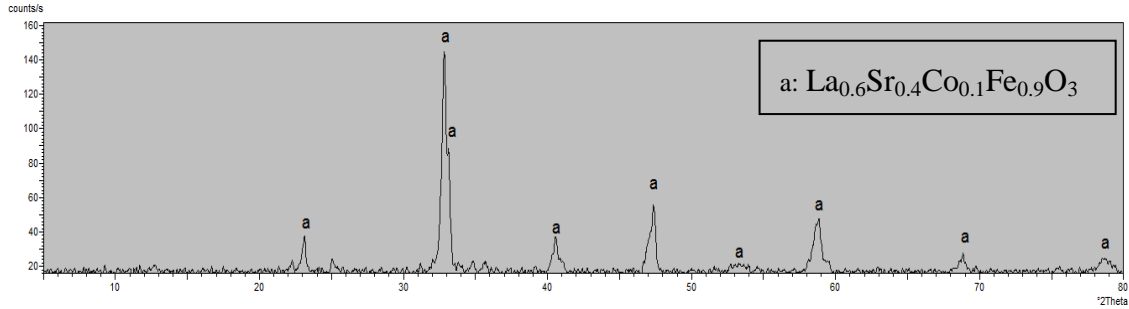


Figure 4.53. XRD chart for  $\text{La}(\text{NO}_3)_3 \cdot 6\text{H}_2\text{O} + \text{SrCl}_2 \cdot 6\text{H}_2\text{O} + \text{Fe}(\text{NO}_3)_3 \cdot 9\text{H}_2\text{O} + \text{Co}(\text{NO}_3)_2 \cdot 6\text{H}_2\text{O}$  mixture after heat treatment.

The particle size of the  $\text{La}_{0.6}\text{Sr}_{0.4}\text{Co}_{0.1}\text{Fe}_{0.9}\text{O}_3$  was estimated from the width, at mean height, of the diffraction peaks of the X-rays, calculated using Scherrer's equation:

$$d = B\lambda / (\beta \cos\theta)$$

where  $d$  is the average particle size of the phase under investigation,  $B$  is Scherrer's constant (0.89),  $\lambda$  is the wavelength used (1.5405 Å),  $\beta$  is the width at mean height (FWHM) of the diffraction peak, and  $\theta$  is the angle of diffraction.

Average particle size of the  $\text{La}_{0.6}\text{Sr}_{0.4}\text{Co}_{0.1}\text{Fe}_{0.9}\text{O}_3$  was calculated to be approximately 230 nm. The broad peaks were hence explained by small submicron crystal size.

Figure 4.54 presents the XRD patterns of as-synthesized the mixture of  $\text{La}(\text{NO}_3)_3 \cdot 6\text{H}_2\text{O} + \text{SrCl}_2 \cdot 6\text{H}_2\text{O} + \text{Co}(\text{NO}_3)_3 \cdot 6\text{H}_2\text{O}$ . Despite elements were reacted with each other perfectly, phase stoichiometry was not as desired. One of the reason of this changing in stoichiometry was distribution ratio of elements into the substrates via heating and second possibility of this changing can be that Co overshadowed Sr.

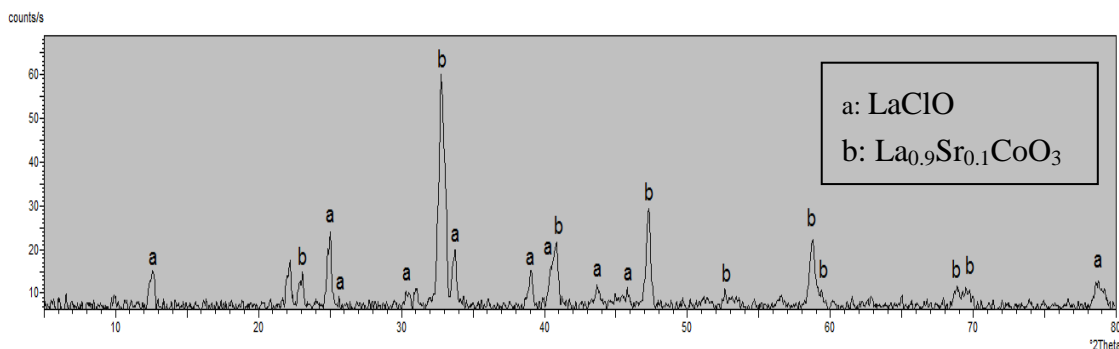


Figure 4.54. XRD chart for  $\text{La}(\text{NO}_3)_3 \cdot 6\text{H}_2\text{O} + \text{SrCl}_2 \cdot 6\text{H}_2\text{O} + \text{Co}(\text{NO}_3)_2 \cdot 6\text{H}_2\text{O}$  mixture after heat treatment.

Figure 4.55 presents the XRD patterns of as-synthesized mixture of  $\text{La}(\text{NO}_3)_3 \cdot 6\text{H}_2\text{O} + \text{Co}(\text{NO}_3)_2 \cdot 6\text{H}_2\text{O} + \text{Fe}(\text{NO}_3)_3 \cdot 9\text{H}_2\text{O}$ . Despite elements were reacted with each other perfectly one by one, they were not react all together in one phases as desired. As can seen from all phases, La element was more dominant than other elements in this mixture after heat treatment.

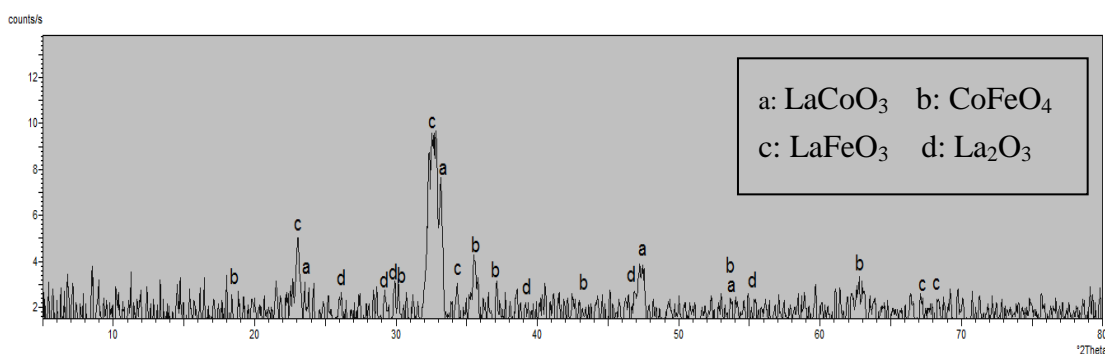


Figure 4.55. XRD chart for  $\text{La}(\text{NO}_3)_3 \cdot 6\text{H}_2\text{O} + \text{Co}(\text{NO}_3)_2 \cdot 6\text{H}_2\text{O} + \text{Fe}(\text{NO}_3)_3 \cdot 9\text{H}_2\text{O}$  mixture after heat treatment.

The XRD patterns of the heat treated  $\text{La}(\text{NO}_3)_3 \cdot 6\text{H}_2\text{O} + \text{SrCl}_2 \cdot 6\text{H}_2\text{O}$  mixture. La and Sr were reacted with each other, as expected by knowledge from EDS analysis.

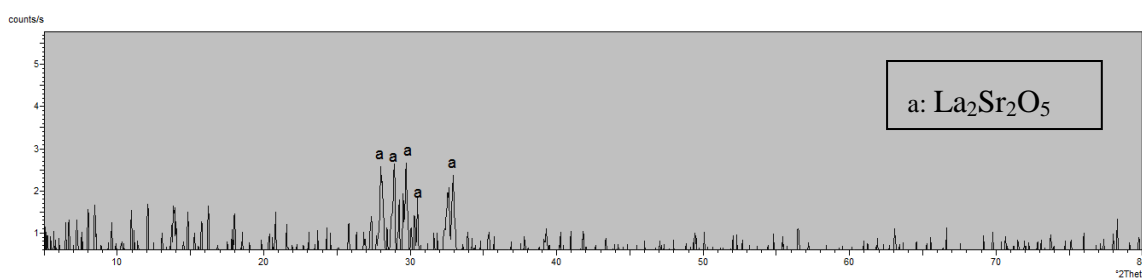


Figure 4.56. XRD chart for  $\text{La}(\text{NO}_3)_3 \cdot 6\text{H}_2\text{O} + \text{SrCl}_2 \cdot 6\text{H}_2\text{O}$  mixture after heat treatment.

Figure 4.57 presents the XRD patterns of as-synthesized the mixture of  $\text{La}(\text{NO}_3)_3 \cdot 6\text{H}_2\text{O} + \text{SrCl}_2 \cdot 6\text{H}_2\text{O} + \text{Fe}(\text{NO}_3)_3 \cdot 9\text{H}_2\text{O}$ . It was desirable phase because of all three elements were present in a single phase.

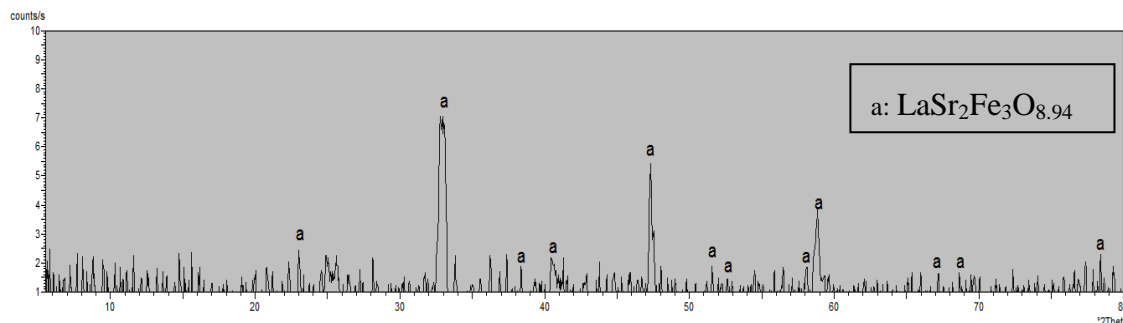


Figure 4.57. XRD chart for  $\text{La}(\text{NO}_3)_3 \cdot 6\text{H}_2\text{O} + \text{SrCl}_2 \cdot 6\text{H}_2\text{O} + \text{Fe}(\text{NO}_3)_3 \cdot 9\text{H}_2\text{O}$  mixture after heat treatment.

The XRD patterns of as-synthesized mixture of  $\text{SrCl}_2 \cdot 6\text{H}_2\text{O} + \text{Co}(\text{NO}_3)_2 \cdot 6\text{H}_2\text{O} + \text{Fe}(\text{NO}_3)_3 \cdot 9\text{H}_2\text{O}$  (Figure 4.58). As can be seen from XRD chart, in spite of Fe and Sr were reacted with each other, Co was not detected in this sample heated after heat treatment, surprisingly. In this temperature precursor salts did not react with each other to produce the desired phase. However, according to EDS analysis, percentage of Co was lowest but still it was existence in coating. (Table 4.1).

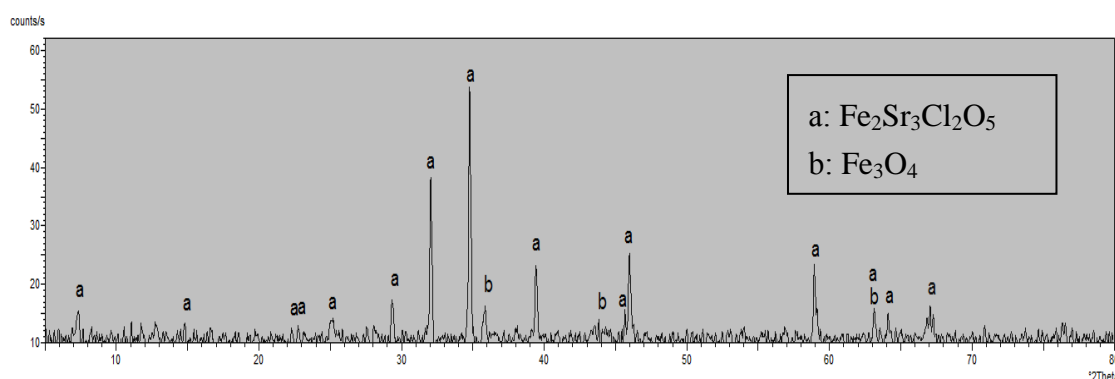


Figure 4.58. XRD chart for  $\text{SrCl}_2 \cdot 6\text{H}_2\text{O} + \text{Co}(\text{NO}_3)_2 \cdot 6\text{H}_2\text{O} + \text{Fe}(\text{NO}_3)_3 \cdot 9\text{H}_2\text{O}$  mixture after heat treatment.

Figure 4.59 presents the XRD patterns of as-synthesized the mixture of  $\text{La}(\text{NO}_3)_3 \cdot 6\text{H}_2\text{O} + \text{SrCl}_2 \cdot 6\text{H}_2\text{O} + \text{Co}(\text{NO}_3)_2 \cdot 6\text{H}_2\text{O} + \text{Fe}(\text{NO}_3)_3 \cdot 9\text{H}_2\text{O}$  that was hoped to yield stoichiometric  $\text{La}_{0.6}\text{Sr}_{0.4}\text{Co}_{0.8}\text{Fe}_{0.2}\text{O}_3$  compound heated via a heating schedule as shown in Figure 3.6. The profile presented characteristic peaks of  $\text{La}_{0.6}\text{Sr}_{0.4}\text{Co}_{0.8}\text{Fe}_{0.2}\text{O}_3$  as

expected which meant that the LSCF 6482 compound was successfully produced in the desired stoichiometry.

Average particle size of the  $\text{La}_{0.6}\text{Sr}_{0.4}\text{Co}_{0.8}\text{Fe}_{0.2}\text{O}_3$  was calculated by using Scherrer's equation to be approximately 340 nm.

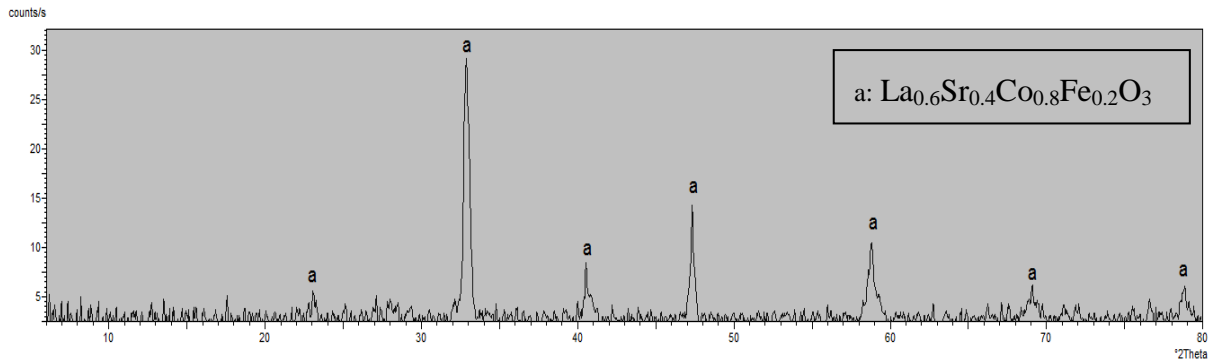


Figure 4.59. XRD chart for  $\text{La}_{0.6}\text{Sr}_{0.4}\text{Co}_{0.8}\text{Fe}_{0.2}\text{O}_3$  stoichiometry mixture after heat treatment.

Figure 4.60 presents the XRD patterns of as-synthesized mixture of  $\text{La}(\text{NO}_3)_3 \cdot 6\text{H}_2\text{O} + \text{SrCl}_2 \cdot 6\text{H}_2\text{O} + \text{Co}(\text{NO}_3)_2 \cdot 6\text{H}_2\text{O} + \text{Fe}(\text{NO}_3)_3 \cdot 9\text{H}_2\text{O}$  that was hoped to synthesize stoichiometric  $\text{La}_{0.6}\text{Sr}_{0.4}\text{Co}_{0.2}\text{Fe}_{0.8}\text{O}_3$  compound upon thermal treatment. This particular salt mixture was able to produce a near stoichiometric LSCF compound even at  $55^\circ\text{C}$  so the expectation was to rapidly form LSCF 6428 in this sample. The result was surprising that LSCF 6428 could not be formed in this sample because of partial loss of constituent elements by diffusion into the substrate during heating. EDS analysis was found to further confirm this theory (Table 4.1 and 4.2).

Average particle size of the  $\text{La}_{0.6}\text{Sr}_{0.4}\text{FeO}_3$  and  $\text{LaCo}_{0.4}\text{Fe}_{0.6}\text{O}_3$  were calculated by using Scherrer's equation to be approximately 209 nm and 206 nm, respectively.

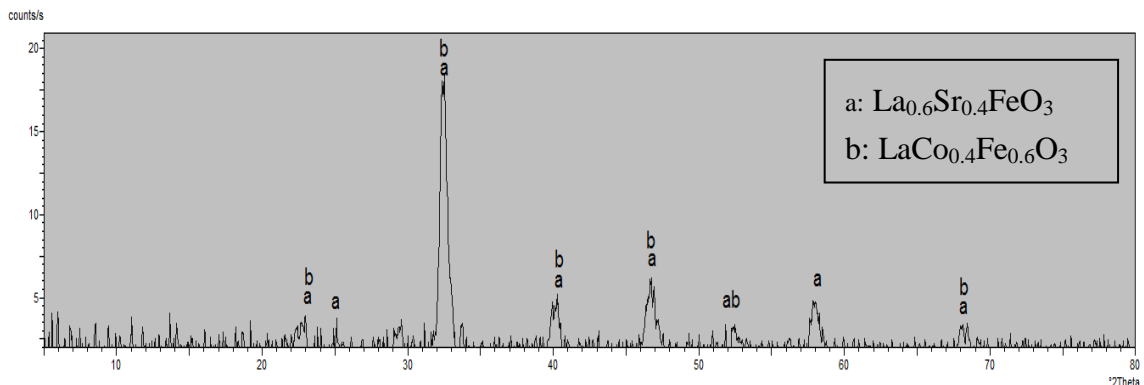


Figure 4.60. XRD chart for  $\text{La}_{0.6}\text{Sr}_{0.4}\text{Co}_{0.2}\text{Fe}_{0.8}\text{O}_3$  stoichiometry mixture after heat treatment.

### 4.3. Thermal Characterization of Precursors Salts

In this part of the thesis, the results of DTA/TGA analyses of as-received and heated mixture salt samples are presented. The resulting graphs are shown in Figures 4.61 to 4.68.

#### 4.3.1. Thermal Characterization of As-Received Precursors Salts

The thermal decomposition of precursor salts is important for better understanding of the solid state reactions.  $\text{La}(\text{NO}_3)_3 \cdot 6\text{H}_2\text{O}$ ,  $\text{SrCl}_2 \cdot 6\text{H}_2\text{O}$ ,  $\text{Co}(\text{NO}_3)_2 \cdot 6\text{H}_2\text{O}$  and  $\text{Fe}(\text{NO}_3)_3 \cdot 9\text{H}_2\text{O}$  as-received precursor salts were studied by using differential thermal analysis (DTA/ TGA) to understand the steps in the decomposition of the precursor salts and to see if they are reacting with each other during the course of heating. The temperature range for the measurements ranged from room temperature to 900 °C at a heating rate of 10 °C/min in air.

TGA and DTA curves of  $\text{La}(\text{NO}_3)_3 \cdot 6\text{H}_2\text{O}$  are shown in Figure 4.61. Thermal decomposition takes place in three stages and is completed at about 640°C for this as-received salt powder. First decomposition stage, from 78 to 209°C, can be assigned to the loss of adsorbed water by five different dehydration processes at 78, 136, 156, 177 and 209°C, respectively. The weight loss in each step was approximately 1 mol of water. Upon completion of these dehydration processes  $\text{La}(\text{NO}_3)_3 \cdot \text{H}_2\text{O}$  was left. And as second decomposition stage, from endothermic peak at 210°C to endothermic peak at 410°C, 1 mol water and 1 mole  $\text{HNO}_3$  was gone. From 410 to 470°C, loss of  $\text{HNO}_3$  took place. Last decomposition stage, 470 to 640°C can be associated with the decomposition of nitrates. As final material,  $\text{La}_2\text{O}_3$  was obtained to confirm the observations in the literature [50].

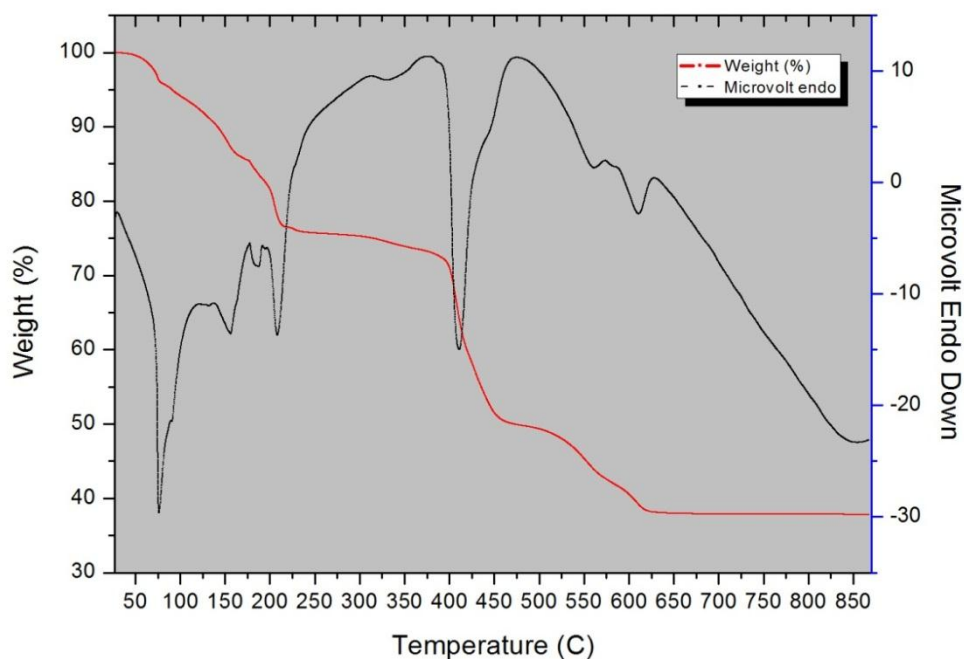


Figure 4.61. DTA (black) / TGA (red) analysis of La(NO<sub>3</sub>)<sub>3</sub>·6H<sub>2</sub>O precursor salt.

TGA and DTA analysis of SrCl<sub>2</sub>·6H<sub>2</sub>O salt is shown in Figure 4.62. Thermal decomposition takes place in three endothermic stages at 95, 120 and 170 °C. The total weight loss was approximately 6 mols of water which was equivalent to 37% weight loss. At the end of these dehydration processes SrCl<sub>2</sub> was obtained. In the literature, the last decomposition temperature is reported to be 180°C with the final product of SrCl<sub>2</sub> phase [51].

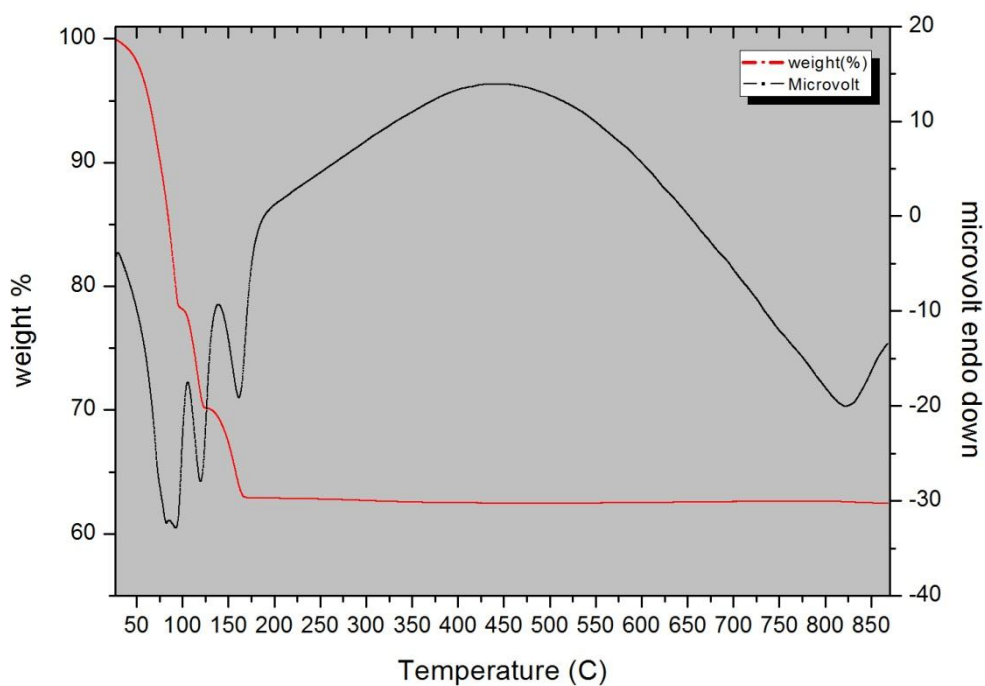


Figure 4.62. DTA (black) / TGA (red) analysis SrCl<sub>2</sub>·6H<sub>2</sub>O precursor salt.

Third precursor salt was Co(NO<sub>3</sub>)<sub>2</sub>·6H<sub>2</sub>O. Figure 4.63 shows the TGA and DTA curves of the decomposition of the salt from room temperature to 900°C. Decomposition was complete in three steps. First step was dehydration process at around 180°C and all steps were finished at 860°C. Co<sub>3</sub>O<sub>4</sub> transformed into CoO as observed by TGA and DTA curves in Figure 4.63. Total weight loss was 26% which is close to that expected theoretically for the formation of CoO [38].

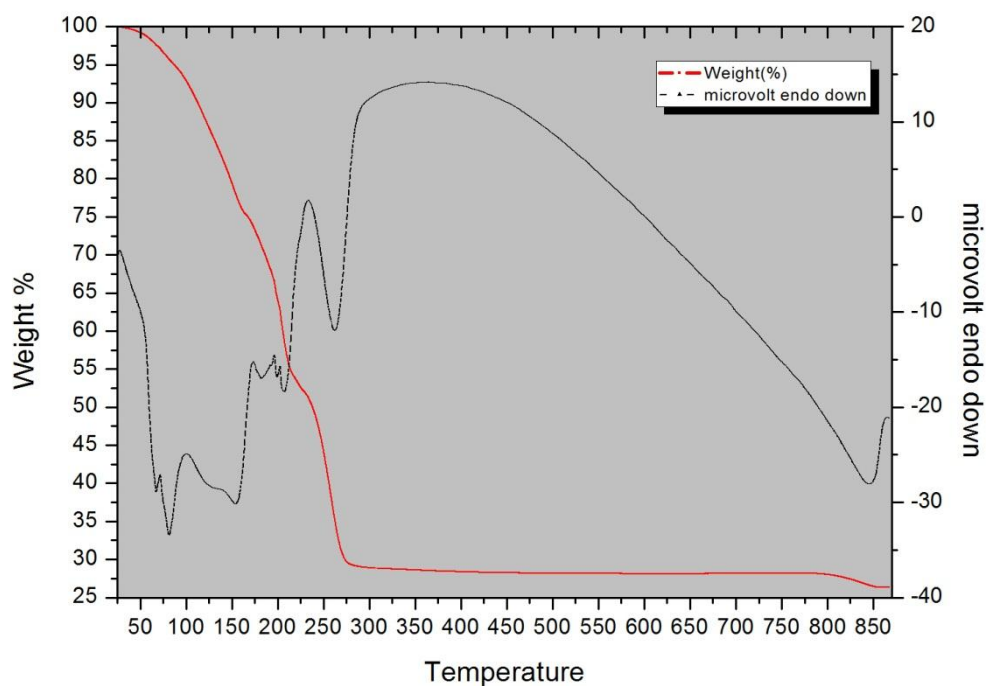


Figure 4.63. DTA (black) / TGA (red) analysis  $\text{Co}(\text{NO}_3)_2 \cdot 6\text{H}_2\text{O}$  precursor salt.

Figure 4.64 shows the TGA and DTA curves of  $\text{Fe}(\text{NO}_3)_3 \cdot 9\text{H}_2\text{O}$  as received precursor salt decomposition. Thermal decomposition takes place in three stages at 59, 105 and 155 °C, respectively. Dehydration process was finished at 140°C. At the end of the decomposition,  $\text{Fe}_3\text{O}_4$  was left at around 400°C.

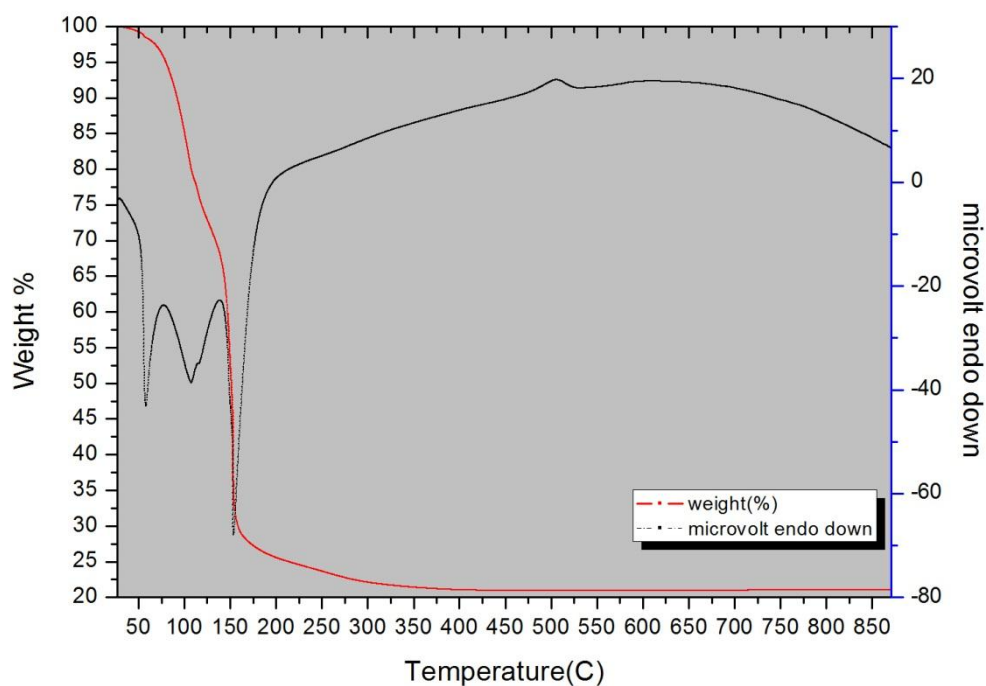


Figure 4.64. DTA (black) / TGA (red) analysis  $\text{Fe}(\text{NO}_3)_3 \cdot 9\text{H}_2\text{O}$  precursor salt.

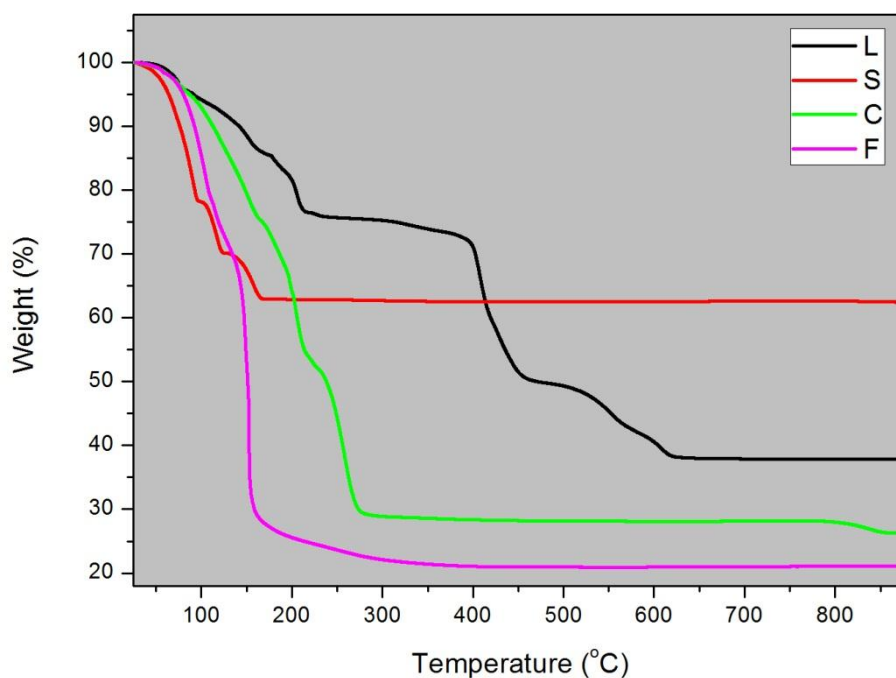


Figure 4.65. TGA analyses of  $\text{La}(\text{NO}_3)_3 \cdot 6\text{H}_2\text{O}$  (black),  $\text{SrCl}_2 \cdot 6\text{H}_2\text{O}$  (red),  $\text{Co}(\text{NO}_3)_2 \cdot 6\text{H}_2\text{O}$  (green) and  $\text{Fe}(\text{NO}_3)_3 \cdot 9\text{H}_2\text{O}$  (pink) precursor salts.

Table 4.3. Last dehydration temperature, temperature at last weight loss and final weight of precursor salts.

Material	Temperature at last weight loss ( $^{\circ}\text{C}$ )	Final weight (%)
$\text{La}(\text{NO}_3)_3 \cdot 6\text{H}_2\text{O}$	640	38
$\text{SrCl}_2 \cdot 6\text{H}_2\text{O}$	170	62
$\text{Co}(\text{NO}_3)_2 \cdot 6\text{H}_2\text{O}$	860	26
$\text{Fe}(\text{NO}_3)_3 \cdot 9\text{H}_2\text{O}$	400	21

### 4.3.2. Thermal Characterization of As-Synthesized Precursors Salts

In order to understand the thermal decomposition of these mixtures better, the weight loss curves of all mixtures which have two, three and four ingredients are shown all together in Figures 4.66 to 4.68.

TGA curves of  $\text{La}(\text{NO}_3)_3 \cdot 6\text{H}_2\text{O} + \text{Co}(\text{NO}_3)_2 \cdot 6\text{H}_2\text{O}$  (L+C),  $\text{SrCl}_2 \cdot 6\text{H}_2\text{O} + \text{Co}(\text{NO}_3)_2 \cdot 6\text{H}_2\text{O}$  (S+C),  $\text{Co}(\text{NO}_3)_2 \cdot 6\text{H}_2\text{O} + \text{Fe}(\text{NO}_3)_3 \cdot 9\text{H}_2\text{O}$  (C+F),  $\text{La}(\text{NO}_3)_3 \cdot 6\text{H}_2\text{O} + \text{Fe}(\text{NO}_3)_3 \cdot 9\text{H}_2\text{O}$  (L+F),  $\text{SrCl}_2 \cdot 6\text{H}_2\text{O} + \text{Fe}(\text{NO}_3)_3 \cdot 9\text{H}_2\text{O}$  (S+F) and  $\text{La}(\text{NO}_3)_3 \cdot 6\text{H}_2\text{O} + \text{SrCl}_2 \cdot 6\text{H}_2\text{O}$  (L+S) with respectively black, red, green, yellow, blue and orange colors are presented in Figure 4.66.

As can be seen from Figure 4.66 TGA chart of the mixture of  $\text{La}(\text{NO}_3)_3 \cdot 6\text{H}_2\text{O} + \text{Co}(\text{NO}_3)_2 \cdot 6\text{H}_2\text{O}$  (black curve) was significantly different from both  $\text{La}(\text{NO}_3)_3 \cdot 6\text{H}_2\text{O}$  and  $\text{Co}(\text{NO}_3)_2 \cdot 6\text{H}_2\text{O}$  curves. Decomposition process was finished at  $640^{\circ}\text{C}$  and  $860^{\circ}\text{C}$  with  $\text{La}_2\text{O}_3$  and  $\text{CoO}$  final products for  $\text{La}(\text{NO}_3)_3 \cdot 6\text{H}_2\text{O}$  and  $\text{Co}(\text{NO}_3)_2 \cdot 6\text{H}_2\text{O}$ , respectively. However, final weight loss of  $\text{La}(\text{NO}_3)_3 \cdot 6\text{H}_2\text{O} + \text{Co}(\text{NO}_3)_2 \cdot 6\text{H}_2\text{O}$  mixture was at around  $920^{\circ}\text{C}$ . Final product of this mixture was  $\text{LaCoO}_3$  according to the XRD chart of this mixture in Figure 4.48 and TGA analysis confirmed this data. Theoretically 34% of total weight was supposed to be left while the experimental observation was 31% according to the TGA curve.

Second TGA chart belongs to of  $\text{SrCl}_2 \cdot 6\text{H}_2\text{O} + \text{Co}(\text{NO}_3)_2 \cdot 6\text{H}_2\text{O}$  and it was presented by red curve in Figure 4.66. It is obvious that this chart was different from both precursor salts. Decomposition of  $\text{SrCl}_2 \cdot 6\text{H}_2\text{O}$  finished at  $170^{\circ}\text{C}$  and  $\text{SrCl}_2$  was obtained as final product. Another precursor salt of this mixture was  $\text{Co}(\text{NO}_3)_2 \cdot 6\text{H}_2\text{O}$  which had a final weight loss at  $860^{\circ}\text{C}$ . On the other hand, the decomposition of this

mixture was finished at a much later than expected temperature of around 920°C.

Thermal decomposition curves of  $\text{Co}(\text{NO}_3)_2 \cdot 6\text{H}_2\text{O} + \text{Fe}(\text{NO}_3)_3 \cdot 9\text{H}_2\text{O}$  (green curve) and  $\text{SrCl}_2 \cdot 6\text{H}_2\text{O} + \text{Fe}(\text{NO}_3)_3 \cdot 9\text{H}_2\text{O}$  (blue curve) mixtures were quite similar with each other and they were not much different from their ingredient salts. Final weight loss temperature of  $\text{SrCl}_2 \cdot 6\text{H}_2\text{O}$  was around 170°C and  $\text{SrCl}_2$  was obtained as final product after decomposition process. Final decomposition temperature of  $\text{Co}(\text{NO}_3)_2 \cdot 6\text{H}_2\text{O}$  was approximately 640°C and  $\text{CoO}$  was left as the final product in this temperature.  $\text{Fe}_3\text{O}_4$  was the final product of  $\text{Fe}(\text{NO}_3)_3 \cdot 9\text{H}_2\text{O}$ , which formed around 400°C. Decomposition of  $\text{Co}(\text{NO}_3)_2 \cdot 6\text{H}_2\text{O} + \text{Fe}(\text{NO}_3)_3 \cdot 9\text{H}_2\text{O}$  mixture was finished around 450°C. However, final weight loss temperature of other mixture ( $\text{SrCl}_2 \cdot 6\text{H}_2\text{O} + \text{Fe}(\text{NO}_3)_3 \cdot 9\text{H}_2\text{O}$ ) was between 410-430°C which was quite close to expectation. Notwithstanding of this, both curves of mixtures were quite similar. Because both final decomposition temperatures were more close to the final temperature of  $\text{Fe}(\text{NO}_3)_3 \cdot 9\text{H}_2\text{O}$  precursor (Figure 4.64). C+F mixture appeared to have some limited reaction around 250-420°C while S+F appeared to have not reacted at all.

Decomposition process of the mixed ingredients of  $\text{La}(\text{NO}_3)_3 \cdot 6\text{H}_2\text{O}$  and  $\text{Fe}(\text{NO}_3)_3 \cdot 9\text{H}_2\text{O}$  is shown in Figure 4.66 with yellow TGA curve. Final decomposition temperatures of  $\text{La}(\text{NO}_3)_3 \cdot 6\text{H}_2\text{O}$  and  $\text{Fe}(\text{NO}_3)_3 \cdot 9\text{H}_2\text{O}$  were around 640°C and 400°C, respectively. In spite of this, decomposition of  $\text{La}(\text{NO}_3)_3 \cdot 6\text{H}_2\text{O}$  and  $\text{Fe}(\text{NO}_3)_3 \cdot 9\text{H}_2\text{O}$  mixture was completed around 760°C. There was a bump in L+C curve around 450-700°C.

Thermal analysis of  $\text{La}(\text{NO}_3)_3 \cdot 6\text{H}_2\text{O} + \text{SrCl}_2 \cdot 6\text{H}_2\text{O}$  mixture is shown by the orange curve in Figure 4.66. There were three major weight loss knees. The curve looked more like the L curve than the S curve. The final decomposition temperature of the mixture of  $\text{La}(\text{NO}_3)_3 \cdot 6\text{H}_2\text{O} + \text{SrCl}_2 \cdot 6\text{H}_2\text{O}$  was almost complete at 640°C while some small weight loss continued to take place up until 1000°C.

Interestingly, L+C, S+C, L+F and L+C+F had same weight loss around 760°C. Another interesting result of the graphs was that S+C and L+S lost the least amount of weight of roughly 60%. L+C and L+F had higher weight loss of about 70%. S+F and C+F had the highest weight loss of around 75%. As can be seen from the data, mixtures which had  $\text{SrCl}_2 \cdot 6\text{H}_2\text{O}$  had lost least weight. Mixtures that included  $\text{La}(\text{NO}_3)_3 \cdot 6\text{H}_2\text{O}$  lost weight more than the mixtures that included  $\text{SrCl}_2 \cdot 6\text{H}_2\text{O}$ . Finally, mixtures that contained  $\text{Fe}(\text{NO}_3)_3 \cdot 9\text{H}_2\text{O}$  lost the highest amount of weights by heat treatment. However, effect of Co was not clear according to this data. Furthermore, another

interestingly result of these graphs, Sr always appeared to be the passive partner failing to outweigh its opponent in the TGA curve.

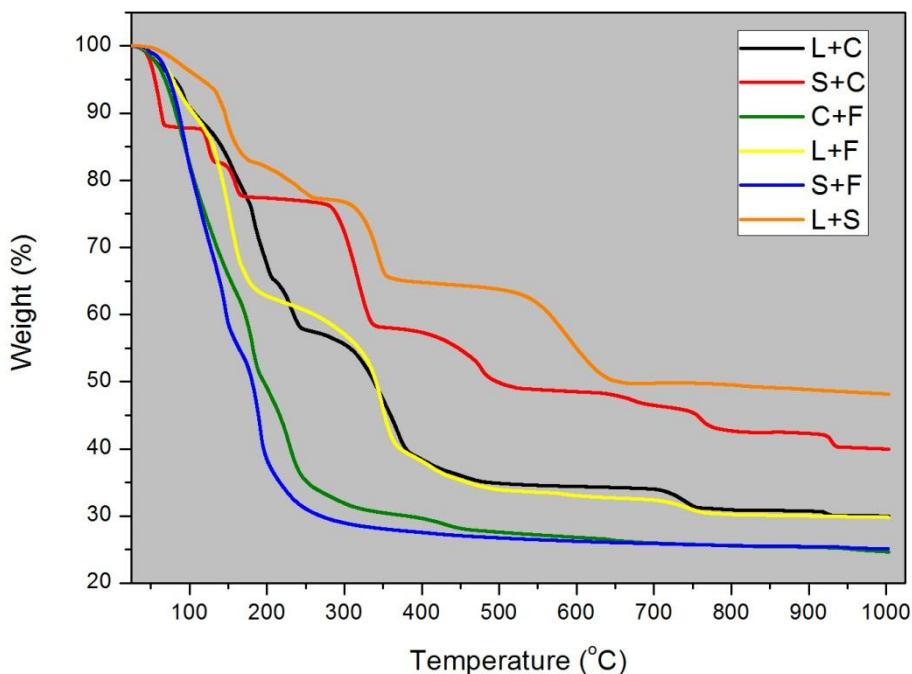


Figure 4.66. TGA analyses of mixtures with two ingredients.

Figure 4.67 shows the thermal decomposition curves of  $\text{La}(\text{NO}_3)_3 \cdot 6\text{H}_2\text{O} + \text{SrCl}_2 \cdot 6\text{H}_2\text{O} + \text{Co}(\text{NO}_3)_2 \cdot 6\text{H}_2\text{O}$ ,  $\text{La}(\text{NO}_3)_3 \cdot 6\text{H}_2\text{O} + \text{Co}(\text{NO}_3)_2 \cdot 6\text{H}_2\text{O} + \text{Fe}(\text{NO}_3)_3 \cdot 9\text{H}_2\text{O}$ ,  $\text{La}(\text{NO}_3)_3 \cdot 6\text{H}_2\text{O} + \text{SrCl}_2 \cdot 6\text{H}_2\text{O} + \text{Fe}(\text{NO}_3)_3 \cdot 9\text{H}_2\text{O}$  and  $\text{SrCl}_2 \cdot 6\text{H}_2\text{O} + \text{Co}(\text{NO}_3)_2 \cdot 6\text{H}_2\text{O} + \text{Fe}(\text{NO}_3)_3 \cdot 9\text{H}_2\text{O}$  mixtures by black, red, green and orange curves, respectively. It is explicit that TGA charts of mixtures were different from the curves for ingredient precursor salts.

Mixture of  $\text{La}(\text{NO}_3)_3 \cdot 6\text{H}_2\text{O} + \text{SrCl}_2 \cdot 6\text{H}_2\text{O} + \text{Co}(\text{NO}_3)_2 \cdot 6\text{H}_2\text{O}$  is shown by the black curve in Figure 4.67. Decomposition of the ingredients was finished at 640°C, 170°C and 860°C, respectively. On the other hand, decomposition of the mixture was completed around 800°C, earlier than that expected.

The TGA curves of the mixture of  $\text{La}(\text{NO}_3)_3 \cdot 6\text{H}_2\text{O} + \text{SrCl}_2 \cdot 6\text{H}_2\text{O} + \text{Fe}(\text{NO}_3)_3 \cdot 9\text{H}_2\text{O}$  is shown in Figure 4.67 by green color. The difference between the mixture and the plain ingredients was pronounced. Final decomposition temperature was 640°C for  $\text{La}(\text{NO}_3)_3 \cdot 6\text{H}_2\text{O}$ , 170°C for  $\text{SrCl}_2 \cdot 6\text{H}_2\text{O}$  and 400°C for  $\text{Fe}(\text{NO}_3)_3 \cdot 9\text{H}_2\text{O}$  with  $\text{La}_2\text{O}_3$ ,  $\text{SrCl}_2$  and  $\text{Fe}_3\text{O}_4$  final products. Although final weight loss temperatures of

the plain ingredients were only 640°C, final weight loss temperature of the mixture was about 810°C. Decomposition process was hence finished at a higher temperature than expected.

Decomposition process of the mixed ingredients of  $\text{La}(\text{NO}_3)_3 \cdot 6\text{H}_2\text{O}$  +  $\text{Co}(\text{NO}_3)_2 \cdot 6\text{H}_2\text{O}$  +  $\text{Fe}(\text{NO}_3)_3 \cdot 9\text{H}_2\text{O}$  is shown by the red TGA curve in Figure 4.93. Final decomposition temperatures of  $\text{La}(\text{NO}_3)_3 \cdot 6\text{H}_2\text{O}$ ,  $\text{Co}(\text{NO}_3)_2 \cdot 6\text{H}_2\text{O}$  and  $\text{Fe}(\text{NO}_3)_3 \cdot 9\text{H}_2\text{O}$  were around 640°C, 860°C and 400°C. Decomposition of their mixture took place rapidly until 330°C and slowly until 1000°C.

Orange curve in Figure 4.67 represents the TGA chart of the mixture of  $\text{SrCl}_2 \cdot 6\text{H}_2\text{O}$  +  $\text{Co}(\text{NO}_3)_2 \cdot 6\text{H}_2\text{O}$  +  $\text{Fe}(\text{NO}_3)_3 \cdot 9\text{H}_2\text{O}$  which had the least amount of weight loss of 50%. Final decomposition temperatures of the ingredients were 170°C, 860°C and 400°C, respectively. However, decomposition of the mixture finished later than expected around 1000°C.

Just like other precursor salt and two reactant mixtures graphs (from Figure 4.66 and 4.67), as can be seen from the data, S+C+F mixture which did not have  $\text{La}(\text{NO}_3)_3 \cdot 6\text{H}_2\text{O}$  had lost least weight. L+C+F mixture that did not include  $\text{SrCl}_2 \cdot 6\text{H}_2\text{O}$  lost weight more than the other mixtures.

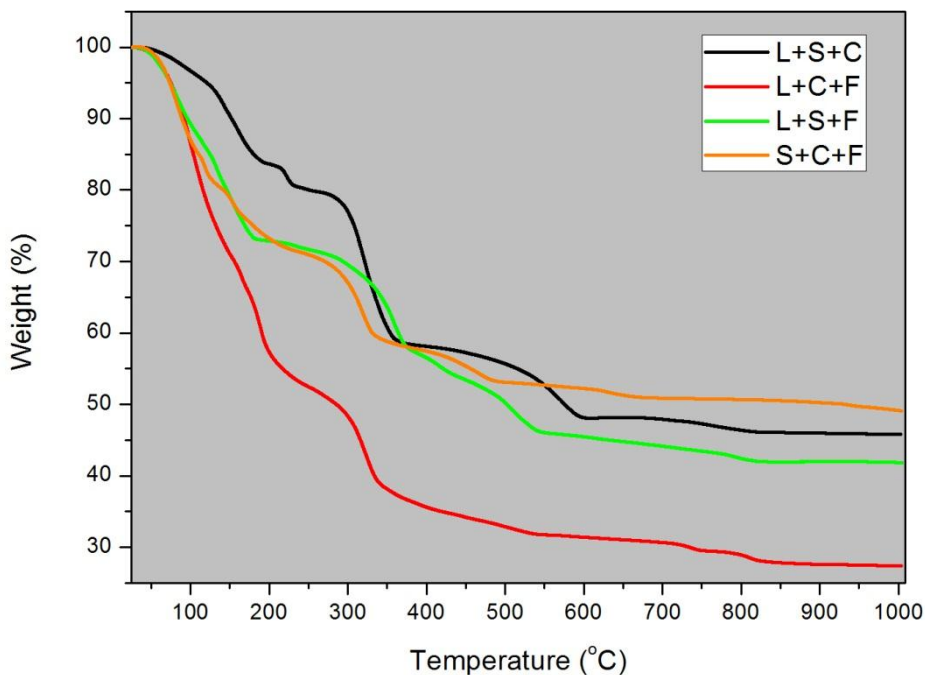


Figure 4.67. TGA analyses of mixtures with three ingredients.

Thermal decomposition curves of the mixtures of LSCF in 1:1:1:1, 6:4:8:2 and 6:4:2:8 molar ratio are shown in Figure 4.68. The final decomposition temperatures of the precursors were 640°C for  $\text{La}(\text{NO}_3)_3 \cdot 6\text{H}_2\text{O}$ , 170°C for  $\text{SrCl}_2 \cdot 6\text{H}_2\text{O}$ , 860°C for  $\text{Co}(\text{NO}_3)_2 \cdot 6\text{H}_2\text{O}$  and 400°C for  $\text{Fe}(\text{NO}_3)_3 \cdot 9\text{H}_2\text{O}$  as shown also in Table 4.3.

Final weight loss of LSCF in 1:1:1:1 molar ratio was around 845°C close to expectation. Final decomposition of the other two samples were 910°C and 1000°C for LSCF in 6482 and 6428, respectively. Both curves were quite similar after 220°C and they had nearly the same final weight loss in the end of decomposition.

Because these three samples were all LSCF samples in different proportions, it was expected to obtain quite similar curves and they did, unsurprisingly. Especially, the portion of the curve which was between 550-840°C was almost identical. In spite of,  $\text{L}_6\text{S}_4\text{C}_8\text{F}_2$  and  $\text{L}_6\text{S}_4\text{C}_2\text{F}_8$  curves were quite similar, the weight loss of LSCF mixture were less than  $\text{L}_6\text{S}_4\text{C}_8\text{F}_2$  and  $\text{L}_6\text{S}_4\text{C}_2\text{F}_8$ . Increasing the proportion of S and decreasing the proportion of L caused the less weight loss than  $\text{L}_6\text{S}_4\text{C}_8\text{F}_2$  and  $\text{L}_6\text{S}_4\text{C}_2\text{F}_8$ .

More interestingly mixtures of LS, LSC, LCF, LSCF,  $\text{L}_6\text{S}_4\text{C}_8\text{F}_2$  and  $\text{L}_6\text{S}_4\text{C}_2\text{F}_8$  had approximately same curve between 550°C and 840°C. Furthermore, all of them had  $\text{La}(\text{NO}_3)_3 \cdot 6\text{H}_2\text{O}$  and  $\text{SrCl}_2 \cdot 6\text{H}_2\text{O}$  precursor salts in their mixture composition.

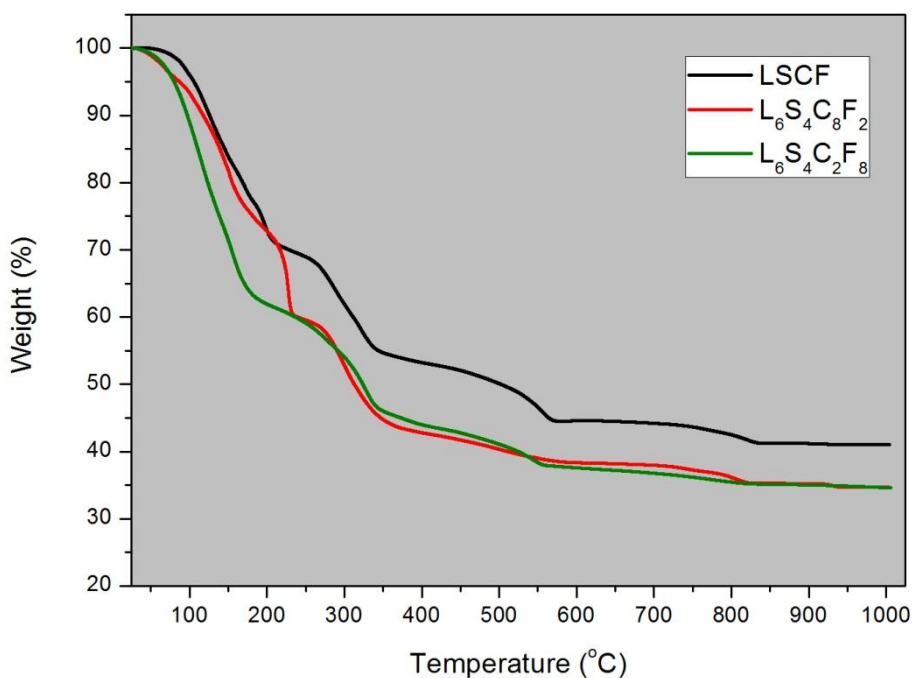


Figure 4.68. TGA analysis of mixture of  $\text{La}(\text{NO}_3)_3 \cdot 6\text{H}_2\text{O}$  +  $\text{SrCl}_2 \cdot 6\text{H}_2\text{O}$  +  $\text{Co}(\text{NO}_3)_2 \cdot 6\text{H}_2\text{O}$  +  $\text{Fe}(\text{NO}_3)_3 \cdot 9\text{H}_2\text{O}$  in different stoichiometry.

#### 4.4. General Interpretation and Discussion

A set of experiments was done for the purpose of investigation of the formation of  $\text{La}_{1-x}\text{Sr}_x\text{Co}_{1-y}\text{Fe}_y\text{O}_{3-d}$  cathode materials and their interaction with electrolyte substrates for potential IT-SOFC applications.

First of all, as-received precursor salts of  $\text{La}(\text{NO}_3)_3 \cdot 6\text{H}_2\text{O}$ ,  $\text{SrCl}_2 \cdot 6\text{H}_2\text{O}$ ,  $\text{Co}(\text{NO}_3)_2 \cdot 6\text{H}_2\text{O}$  and  $\text{Fe}(\text{NO}_3)_2 \cdot 9\text{H}_2\text{O}$  were analyzed by XRD, SEM, TGA and DTA to confirm their structures and chemistries. SEM images of precursor salts indicated that  $\text{Co}(\text{NO}_3)_2 \cdot 6\text{H}_2\text{O}$  prematurely melted at near room temperature which appeared with rounded edges. Initial phases of  $\text{La}(\text{NO}_3)_3 \cdot 6\text{H}_2\text{O}$ ,  $\text{SrCl}_2 \cdot 6\text{H}_2\text{O}$ ,  $\text{Co}(\text{NO}_3)_2 \cdot 6\text{H}_2\text{O}$  and  $\text{Fe}(\text{NO}_3)_2 \cdot 9\text{H}_2\text{O}$  were proven by XRD analysis. However, XRD chart of  $\text{Fe}(\text{NO}_3)_2 \cdot 9\text{H}_2\text{O}$  indicated that one of the bounded waters was released at room temperature after blending in agate mortar. This was further confirmed by DTA-TGA analysis. A similar observation was also made in the literature [34]. DTA-TGA graphs and also information in the literature indicated that the other three precursors release their first bounded water around  $50^\circ\text{C}$  or above [50][51][38].

TGA curves showed that mixtures that included  $\text{SrCl}_2 \cdot 6\text{H}_2\text{O}$  had the least weight loss and those with  $\text{Fe}(\text{NO}_3)_2 \cdot 9\text{H}_2\text{O}$  had the most weight loss. TGA results of as-received precursor salts indicated that decomposition reactions were completed before  $650^\circ\text{C}$  (except a small phase changing from  $\text{Co}_3\text{O}_4$  to  $\text{CoO}$  at  $860^\circ\text{C}$  in  $\text{Co}(\text{NO}_3)_2 \cdot 6\text{H}_2\text{O}$ ), confirming the information in the literature [38]. Some of the as-synthesized mixtures had the final decomposition temperature over  $800^\circ\text{C}$ . Therefore, heat schedule selected for the experiments went up to  $1050^\circ\text{C}$  in order to finish all possible reactions of mixtures.

XRD charts showed that La was the key element for reactions at low temperatures. In the presence of La, all elements easily reacted. However, in the absence of La, other elements had significant problem to react with each other at low temperature. There was no knowledge about this topic in the literature yet. Also XRD charts indicated that Sr tended to swap its chloride and take the nitrate from its partner at low temperature. As-synthesized mixtures were placed into the kiln and heated according to the heat schedule in Figure 3.6. XRD results of the heated samples indicated that salts decomposed thoroughly and reacted completely by the help of heat, as expected. When the 6428 sample was blended and heated at  $55^\circ\text{C}$  temperature, an

erratic LSCF compound was interestingly observed at low temperature. The expectation was to observe the rapid formation of  $L_6S_4C_2F_8$  in this sample upon heating. But the heated sample produced no such phase. The other salt mixture with  $L_6S_4C_8F_2$  stoichiometry, on the other hand, surprisingly produced the oxide,  $L_6S_4C_8F_2$  in the desired stoichiometry. This difference in the behaviors may arise from the differences in the distribution ratios of La, Sr, Co and Fe elements in the coating and substrate layers.

As final step, diffusion couple experiments were done and the samples were investigated by SEM-EDS analysis on broken sample fracture surface. There are two state of the art materials for use as a substrate in IT-SOFC applications and both of them were used in the experiments as substrate. By the help of the distribution ratio which was defined in Chapter 3.3.1 and used in Table 4.1 and 4.2., it was understood that La, Sr, Co and Fe elements transported from cathode layer into the CGO substrate layer faster than through the zirconia layer due possibly to the higher density and melting point of zirconia substrate.

To sum up, La is the key element to enable formation of new oxide phases in LSCF formation process.  $La_{0.6}Sr_{0.4}Co_{0.8}Fe_{0.2}O_3$  was successfully produced as the cathode layer over the substrate by the solid state method without using ethanol. LSCF 6428, however, could not be produced at the desired stoichiometry principally due to premature loss of constituent elements during too slow heating in the furnace. When the same samples are heated rapidly, LSCF 6428 could be formed [12].

## CHAPTER 5

### CONCLUSION

Decomposition of the salt powders were studied using DTA, TGA and XRD to understand the reactions that take place during heating. Data in the literature was confirmed as far as the decomposition of salts alone are considered. But when these salts were mixed in different combinations some interesting findings were observed. Almost all combinations of LSCF salt mixtures were prepared and analyzed by SEM-EDS, XRD and DTA-TGA before heat treatment and after treatment. From SEM-EDS analyses it was found that there was a weak diffusion from the cathode layer into the both CGO and Zirconia substrate. However, there was some significant diffusion into the CGO substrate in some examples especially mixture of L+S+C and  $L_6S_4C_2F_8$ . La was usually able to diffuse through the substrate better than the other precursor elements of LSCF, namely Sr, Co and Fe. The cathode layers in most of the samples formed well to cover the substrate surface. These layers appeared to be porous enough and uniform to satisfy electrochemical reaction for oxygen reduction. Both electrolyte materials (CGO and Zirconia) were quite dense and uniform, as desired. Spot analysis of some examples in electrolyte layer did not confirm diffusion of LSCF elements. Therefore, dot-map observations need to be confirmed by other measurements before being used for interpretations. Based on XRD analyses it was found that La plays a significant role to ease the formation of new phases. Without lanthanum, other salts had significant difficulty to react to form new phases. Sr salt preferentially transformed itself into nitrate by swapping its chloride upon heating. The nitrate salt of iron was observed to rapidly flow like a liquid during handling before XRD analysis. This was thought to originate from premature loss of chemically bound water at near-room temperature. Observations from the TGA analyses indicated that mixtures which had  $SrCl_2 \cdot 6H_2O$  had lost least weight. Mixtures that included  $La(NO_3)_3 \cdot 6H_2O$  lost weight more than the mixtures that included  $SrCl_2 \cdot 6H_2O$ . Finally, mixtures that contained  $Fe(NO_3)_3 \cdot 9H_2O$  lost the highest amount of weight by heat treatment. However, effect of Co was not clear according to this data. Sr appeared to be the passive partner failing to outweigh its partner elements (La, Fe) in the TGA curve bumps and steps. TGA curves for  $L_6S_4C_8F_2$  and  $L_6S_4C_2F_8$  curves were quite similar. The weight loss of LSCF mixture in one-to-one

molar proportions was less than that of  $\text{L}_6\text{S}_4\text{C}_8\text{F}_2$  and  $\text{L}_6\text{S}_4\text{C}_2\text{F}_8$ . Increasing the proportion of  $\text{SrCl}_2 \cdot 6\text{H}_2\text{O}$  and decreasing the proportion of  $\text{La}(\text{NO}_3)_3 \cdot 6\text{H}_2\text{O}$  caused less weight loss in  $\text{L}_6\text{S}_4\text{C}_8\text{F}_2$  and  $\text{L}_6\text{S}_4\text{C}_2\text{F}_8$ . Mixtures of LS, LSC, LCF, LSCF,  $\text{L}_6\text{S}_4\text{C}_8\text{F}_2$  and  $\text{L}_6\text{S}_4\text{C}_2\text{F}_8$  had approximately the same bumps between  $550^\circ\text{C}$  and  $840^\circ\text{C}$ . Furthermore, all of them had  $\text{La}(\text{NO}_3)_3 \cdot 6\text{H}_2\text{O}$  and  $\text{SrCl}_2 \cdot 6\text{H}_2\text{O}$  precursor salts in their mixture composition. As a final word of all the thesis it can be said that the diffusion of La, Sr, Co or Fe into the substrate has some effect on the stoichiometry of the resulting coating layer. LSCF could finally be formed via solid state synthesis in 6482 stoichiometry. It was, however, not possible to form the desired oxide in 6428 stoichiometry. Without La things appeared to be very slow in solid state synthesis reactions. Therefore, it is an indispensable constituent in cathode materials. Its effect on electrical properties of cathode materials was not the subject of attention in this thesis.

This thesis can be improved with some works in future. Interface between substrate and cathode layer can be search closer to see diffusion of elements to each other reversely. Secondly, heat distribution of cathode material can be changed and see the differences in the formation of LSCF cathode materials. Thirdly, porosity of the cathode mixtures can be calculated. Finally, find out that the reason why distribution ratio of Sr was high in CGO substrate.

## REFERENCES

- [1] S. Singhal, K. Kendall, *High Temperature Solid Oxide Fuel Cells: Fundamentals, Design, and Applications*, Elsevier, Ltd., Oxford, 2003.
- [2] S. Singhal, *The Electrochemical Society Interface*, pp. 41-44, 16(4), 24, 2007.
- [3] K. Kinoshita, E. J. Cairns. "Fuel Cells" in *Kirk-Othmer Encyclopedia of Chemical Technology*, John Wiley & Sons, Inc., 2000.
- [4] J. D. G. Eileen. (2003). CSA. Available: <http://www.csa.com/discoveryguides/fuecel/overview.php>
- [5] Y. J. Leng, S.H. Chan, S.P. Jiang, and K.A. Khor, "Low-Temperature SOFC with Thin Film GDC Electrolyte Prepared in Situ by Solid-State Reaction", *Solid State Ionics*, 170(1-2), 2004.
- [6] G. Hongxia, R. Ran, W. Zhou, Z. Shao, "Anode-supported ScSZ-electrolyte SOFC with whole cell materials from combined EDTA-citrate complexing synthesis process", *Journal of Power Sources*, vol. 172, pp. 704-712, 2007.
- [7] J.P.P. Huijmans., F.P.F. Van Berkel and G.M. Christie, "Intermediate temperature SOFC-a promise for the 21st century", *Journal of Power Sources*, 71:107-110. 1998.
- [8] Ceram Research. (2001). *Solid Oxide Fuel Cells*. Available: <http://www.azom.com/article.aspx?ArticleID=919>.
- [9] T.M. Besmann and R.D. Carneim and T.R. Armstrong. "In Decomposition of Yttrium-Doped Barium Cerate in Carbon Dioxide; Inorganic membranes for energy and environmental applications", Berlin, Germany: Springer, 2008.
- [10] B. C. H. Steele. "Appraisal of  $Ce_{1-y}Gd_yO_{2-y/2}$  electrolytes for IT-SOFC operation at 500°C", *Solid State Ionics*, vol. 129, No. 1-, ISSN 0167-2738, April 2000.
- [11] I.Taniguchi, R. C. V. Landschoot and J. Schoonman, "Fabrication of  $La_{1-x}Sr_xCo_{1-y}Fe_yO_3$  thin films by electrostatic spray deposition", *Solid State Ionics*, vol 156, Number 1, pp. 1-13(13), January 2003.

- [12] D. Marinha , C. Rossignol and E. Djurado, “Influence of of electrospaying parameters on the microstructure of  $\text{La}_{0.6}\text{Sr}_{0.4}\text{Co}_{0.2}\text{Fe}_{0.8}\text{O}_{3-\delta}$  films for SOFCs”, *Journal of Solid State Chemistry*. vol 182: pp. 1742-1748. 2009.
- [13] H.S. Song, S.H. Hyun, J. Kim, H.W. Lee and J. Moon, *J. Mater. Chem.*, 18, 1087–1092, 2008.
- [14] F. Tietz, A. Mai and D. Stöver. “From powder properties to fuel cell performance- A holistic approach for SOFC cathode development”, *Solid State Ionics*, 179: 1509-1515. 2008.
- [15] EG & G Services (Firm) and National Energy Technology Laboratory (U.S.), *Fuel cell handbook*. Morgantown, WV : U.S. Dept. of Energy, Office of Fossil Energy, National Energy Technology Laboratory, November 2004.
- [16] University of Cambridge (2013). *Dissemination of IT for the Promotion of Materials Science (DoITPoMS)*. Available: <http://www.doitpoms.ac.uk/tlplib/fuel-cells/intro.php>.
- [17] N. Q. Minh and T. Takahashi, “Science and Technology of Ceramic Fuel Cells”, Elsevier Science B.V., Amsterdam, Netherlands, 1995.
- [18] G. Hoogers, *Fuel Cell Technology Handbook*, CRC Press, Germany, 2003.
- [19] B. Cook, *An Introduction to Fuel Cells and Hydrogen Technology*, Vancouver, Canada, December 2001.
- [20] Helsinki University of Technology. New& Renewable Energy Systems Group. (2007). *Fuel Cells*. Available: [http://tfy.tkk.fi/aes/AES/projects/renew/fuelcell/fc\\_1.html](http://tfy.tkk.fi/aes/AES/projects/renew/fuelcell/fc_1.html).
- [21] U.S. Department of Energy, Office of Energy Efficiency and Renewable Energy. (2013). Available from: <http://www.eere.energy.gov/>
- [22] A. Stambouli and Boudghene, “Solid oxide fuel cells (SOFCs): a review of an environmentally clean and efficient source of energy”, *Renewable and Sustainable Energy Reviews*, vol. 6, issue 5, pp. 433–455, October 2002.

- [23] N. Q. Minh and T. Takahashi, "Science and Technology of Ceramic Fuel Cells", Elsevier Science. August 15, 1995.
- [24] (2013). *The Energy Lab*. Available from: <http://www.seca.doe.gov>.
- [25] Nedstack (2013). *Fuel Cell Technology*. Available from: <http://www.nedstack.com>
- [26] (2013). *Fuel Cells*. Available from: <http://www.fuelcells.org>
- [27] A. Bauen and D. Hart, "Assessment of the environmental benefits of transport and stationary fuel cells", *Journal of Power Sources*, 86 (1-2), pp. 482-494, 2000.
- [28] A. J. Appleby, "Fuel Cells: Trends in Research and Application", Berlin, Germany: Hemisphere Publishing, 1987.
- [29] M. Aparicio, A. Jitianu and L. C. Klein, "Sol-Gel Processing for Conventional and Alternative Energy, Advances in Sol-Gel Derived Materials and Technologies", ISBN: 978-1-4614-1956-3, Springer Science+Business Media, New York, 2012.
- [30] (2010) *Solid Oxide Fuel Cells for stationary applications*. Available: [http://www.spin-project.eu/index.php?node\\_id=58.51&lang\\_id=1](http://www.spin-project.eu/index.php?node_id=58.51&lang_id=1).
- [31] N.Q. Minh, S.P.S. Badwal, M.J. Bannister, and R.H.J. Hannink, "Science and Technology of Zirconia V", Technomic Publishing Company, Lancaster, PA, p. 652, 1993.
- [32] J.P.P. Huijmans, "Ceramics in solid oxide fuel cells", *Solid State & Materials Science*, 5: 317-323. 2001
- [33] J. D. Nicolas, "Low Temperature Constrained Sintering of Cerium Gadolinium Oxide for solid oxide fuel cell applications", Lawrence Berkeley National Laboratory 2007.
- [34] K. Wieczorek-Ciurawa and A.J. Kozak, "The Thermal Decomposition of  $\text{Fe}(\text{NO}_3)_3 \cdot 9\text{H}_2\text{O}$ ", *Journal of Thermal Analysis and Calorimetry*, vol 58, pp. 647-651, 1999.

- [35] Risø National Laboratory (2012). Available: <http://www.dtu.dk/english>
- [36] J. B. Goodenough and J. M. Longo, *Magnetic Oxides and Related Oxides*, vol. 4a, Ch. 3, pp. 126-314, Landolt-Bernstein, 1970; S. Nomura, *Magnetic Oxides and Related Oxides*, vol. 4a, pp. 368-520, Landolt-Bernstein, 1978.
- [37] C. S. Tedmon, Jr., H. S. Spacil and S. P. Mitoff, Cathode Materials and Performance in High-Temperature Zirconia Electrolyte Fuel Cells, *Journal of the Electrochemical Society*, vol.116, issue 9, pp. 1170, 1969.
- [38] S. A. A. Mansour, “Spectrothermal studies on the decomposition course of cobalt oxysalts Part II. Cobalt nitrate hexahydrate”, *Materials Chemistry and Physics*, vol 36, issues 3–4, pp. 317-323, ISSN 0254-0584, January 1994.
- [39] Nextech materials. (2001). *Fuel cell materials*. Available: <http://www.nextechmaterials.com/energy/>
- [40] N.Q. Minh, C.E. McPheeters, and J.E. Brule, “Monolithic Solid Oxide Fuel Cell Technology Development, Phase 1A, Final Report”, Report No. GRI-89/0267, Gas Research Institute, Chicago, IL, 1989.
- [41] L.Conceição, A. M. Silva, N. F. P. Ribeiro, and M. M. V. M. Souza, “Combustion synthesis of  $\text{La}_{0.7}\text{Sr}_{0.3}\text{Co}_{0.5}\text{Fe}_{0.5}\text{O}_3$  (LSCF) porous materials for application as cathode in IT-SOFC”, *Materials Research Bulletin*, vol. 46, No. 2, pp. (308-314), ISSN 0025-5408, February 2011.
- [42] G. Alessandro, M. M. Natile, N. Luca and A. Glisenti, “ $\text{La}_{0.8}\text{Sr}_{0.2}\text{Ga}_{0.8}\text{Fe}_{0.2}\text{O}_{3-\delta}$ : Influence of the preparation procedure on reactivity toward methanol and ethanol”, *Applied Catalysis B: Environmental*, vol 97, issues 3–4, Pages 307-322, ISSN 0926-3373, 18 June 2010.
- [43] H. Sun, W. Ma, J. Yu, X. Chen and H. Lin, “Preparation and characterization of  $\text{La}_{0.8}\text{Sr}_{0.04}\text{Ca}_{0.16}\text{Co}_{0.6}\text{Fe}_{0.4}\text{O}_{3-\delta}$ - $\text{La}_{0.9}\text{Sr}_{0.1}\text{Ga}_{0.8}\text{Mg}_{0.2}\text{O}_3$  composite cathode thin film for SOFC by slurry spin coating”, *Journal of Rare Earths*, vol 28, issue 6, pp. 917-921, ISSN 1002-0721, December 2010.
- [44] Y. Leng, S. H. Chan and Q. Liu, “Development of LSCF–GDC composite cathodes for low-temperature solid oxide fuel cells with thin film GDC electrolyte”, *International Journal of Hydrogen Energy*, volume 33, issue 14, Pages 3808-3817, ISSN 0360-3199, July 2008

- [45] P. Yue, Z. Wang, W. Peng, L. Li, W. Chen, H. Guo, X. Li, "Spray-drying synthesized  $\text{LiNi}_{0.6}\text{Co}_{0.2}\text{Mn}_{0.2}\text{O}_2$  and its electrochemical performance as cathode materials for lithium ion batteries", *Powder Technology*, vol 214, issue 3, pp. 279-282, ISSN 0032-5910, 25 December 2011.
- [46] Z.Z. Lazarevic, M. Vijatovic, Z. Dohcevic-Mitrovic, N.Z. Romcevic, M.J. Romcevic, N. Paunovic and B.D. Stojanovic, "The characterization of the barium titanate ceramic powders prepared by the Pechini type reaction route and mechanically assisted synthesis", *J. Eur. Ceram. Soc.* 30, 623-628, 2010.
- [47] G. Alessandro, M. M. Natile, G. Antonella, "LSCF and  $\text{Fe}_2\text{O}_3$ /LSCF powders: Interaction with methanol", *Journal of Molecular Catalysis A: Chemical*, vol 282, issues 1-2, 3, Pages 52-61, ISSN 1381-1169, March 2008.
- [48] C.H. Chen, E.M. Kelder, M.J.G. Jak and J. Schoonman, "Electrostatic spray deposition of thin layers of cathode materials for lithium battery", *Solid State Ionics*, vol. 86-88, Part 2, pp. 1301-1306, ISSN 0167-2738, July 1996.
- [49] A. Jaworek and A. T. Sobczyk, "Electrospraying route to nanotechnology: An overview", *Journal of Electrostatics*, vol 66: 197-219, 2008.
- [50] G. A.H. Mekhemer, B. A.A. Balboul, "Thermal genesis course and characterization of lanthanum oxide", *Colloids and Surfaces A: Physicochemical and Engineering Aspects*, vol. 181, Issues 1-3, pp. 19-29, ISSN 0927-7757, 15 June 2001.
- [51] W.W. Wendlandt, "The thermal properties of inorganic compounds III. Strontium chloride 6-hydrate", *Thermochimica Acta*, vol. 12, issue 4, pp. 359-366, ISSN 0040-6031, August 1975

## APPENDIX A

### SEM-EDS RESULTS OF MIXTURES HEATED ON TOP OF ZIRCONIA SUBSTRATE

Some results of experiments which are not given in Chapter 4 are given in this section of thesis.

The  $\text{La}(\text{NO}_3)_3 \cdot 6\text{H}_2\text{O} + \text{Co}(\text{NO}_3)_2 \cdot 6\text{H}_2\text{O}$  (also coded as L+C) heated on top of zirconia. According to Table 4.1 distribution ratio of La was higher than Co into the substrate (Figure A.1 and A.2)

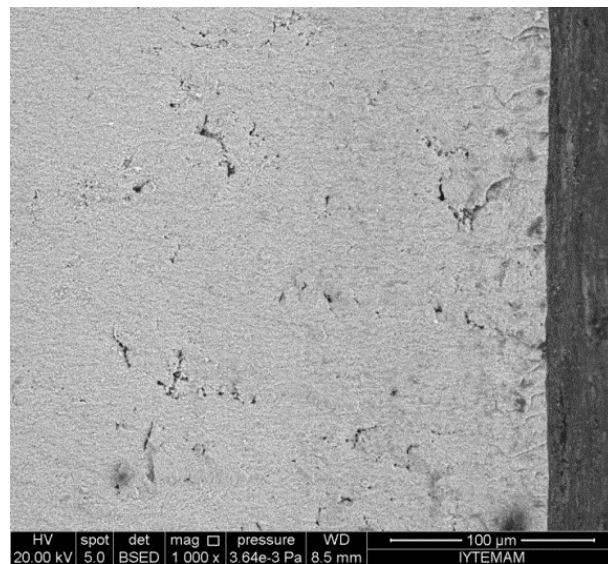


Figure A.1. SEM image of the interface between  $\text{La}(\text{NO}_3)_3 \cdot 6\text{H}_2\text{O} + \text{Co}(\text{NO}_3)_2 \cdot 6\text{H}_2\text{O}$  mixture and zirconia pellets after heat treatment.

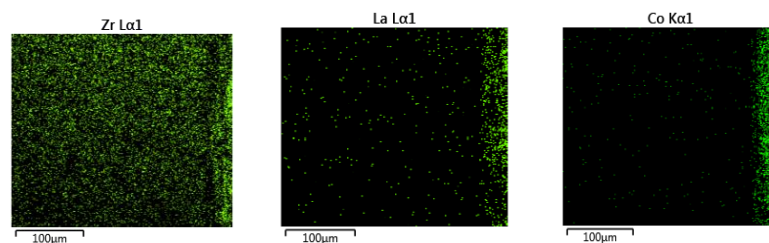


Figure A.2. Mapping analysis of the interface between  $\text{La}(\text{NO}_3)_3 \cdot 6\text{H}_2\text{O} + \text{Co}(\text{NO}_3)_2 \cdot 6\text{H}_2\text{O}$  mixture and zirconia pellets after heat treatment.

$\text{SrCl}_2 \cdot 6\text{H}_2\text{O} + \text{Co}(\text{NO}_3)_2 \cdot 6\text{H}_2\text{O}$  (S+C) mixture heated on top of zirconia (Figure A.3 and A.4)

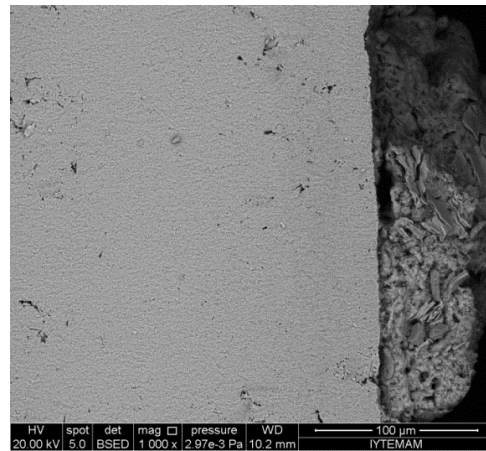


Figure A.3. SEM image of the interface between  $\text{SrCl}_2 \cdot 6\text{H}_2\text{O} + \text{Co}(\text{NO}_3)_2 \cdot 6\text{H}_2\text{O}$  mixture and zirconia pellets after heat treatment.

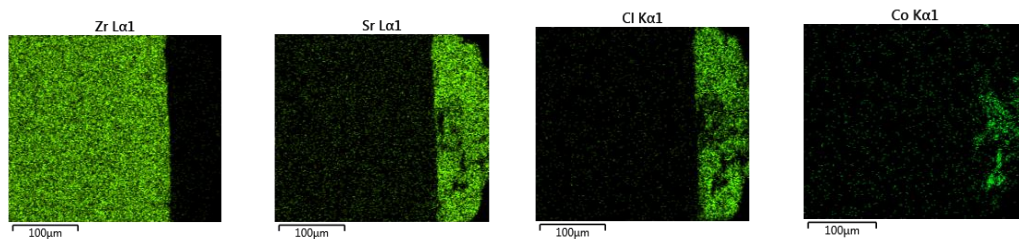


Figure A.4. Mapping analysis of the interface between  $\text{SrCl}_2 \cdot 6\text{H}_2\text{O} + \text{Co}(\text{NO}_3)_2 \cdot 6\text{H}_2\text{O}$  mixture and zirconia pellets after heat treatment.

$\text{Co}(\text{NO}_3)_2 \cdot 6\text{H}_2\text{O} + \text{Fe}(\text{NO}_3)_3 \cdot 9\text{H}_2\text{O}$  (C+F) mixture heated on top of zirconia. Diffusion of all three species was observed to be limited at interface for all elements.

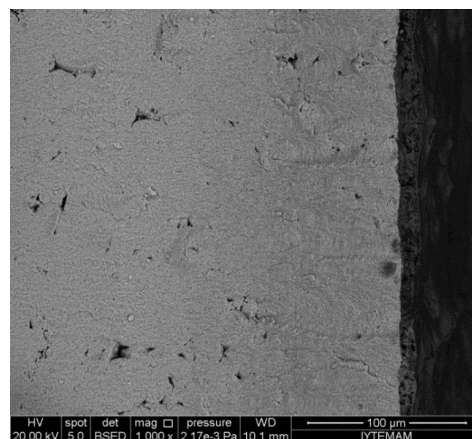


Figure A.5. SEM image of the interface between  $\text{Co}(\text{NO}_3)_2 \cdot 6\text{H}_2\text{O} + \text{Fe}(\text{NO}_3)_3 \cdot 9\text{H}_2\text{O}$  mixture and zirconia pellets after heat treatment.

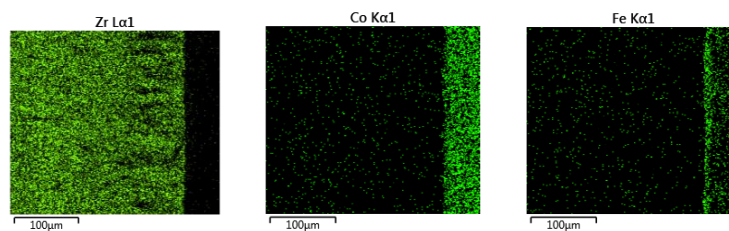


Figure A.6. Mapping analysis of the interface between  $\text{Co}(\text{NO}_3)_2 \cdot 6\text{H}_2\text{O} + \text{Fe}(\text{NO}_3)_3 \cdot 9\text{H}_2\text{O}$  mixture and zirconia pellets after heat treatment.

The mixture of  $\text{La}(\text{NO}_3)_3 \cdot 6\text{H}_2\text{O} + \text{Fe}(\text{NO}_3)_3 \cdot 9\text{H}_2\text{O}$  (L+F) heated on top of zirconia. There was no diffusion of La and Fe elements from cathode layer into the substrate layer according to Table 4.1 (Figure A.7 and A.8).

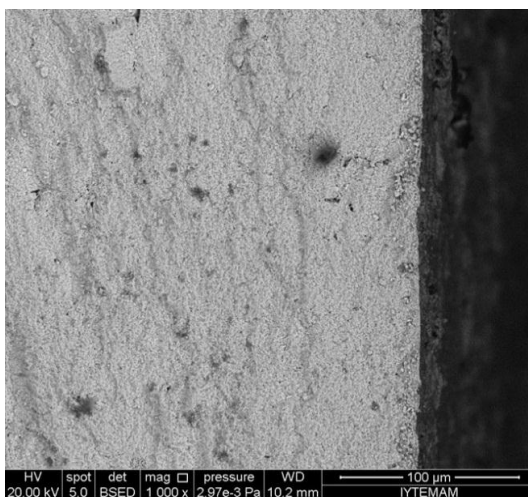


Figure A.7. SEM image of the interface between  $\text{La}(\text{NO}_3)_3 \cdot 6\text{H}_2\text{O} + \text{Fe}(\text{NO}_3)_3 \cdot 9\text{H}_2\text{O}$  mixture and zirconia pellets after heat treatment.

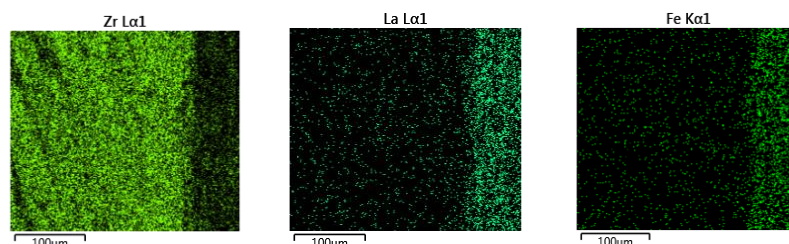


Figure A.8. Mapping analysis of the interface between  $\text{La}(\text{NO}_3)_3 \cdot 6\text{H}_2\text{O} + \text{Fe}(\text{NO}_3)_3 \cdot 9\text{H}_2\text{O}$  mixture and zirconia pellets after heat treatment.

The mixture of  $\text{SrCl}_2 \cdot 6\text{H}_2\text{O} + \text{Fe}(\text{NO}_3)_3 \cdot 9\text{H}_2\text{O}$  heated on top of zirconia. Due to EDS analysis distribution ratio of Sr was 0.00 and Fe was 0.01 (Table 4.1).

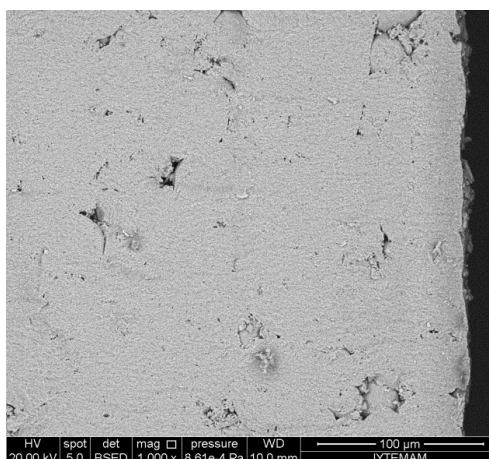


Figure A.9. SEM image of the interface between  $\text{SrCl}_2 \cdot 6\text{H}_2\text{O} + \text{Fe}(\text{NO}_3)_3 \cdot 9\text{H}_2\text{O}$  mixture and zirconia pellets after heat treatment.

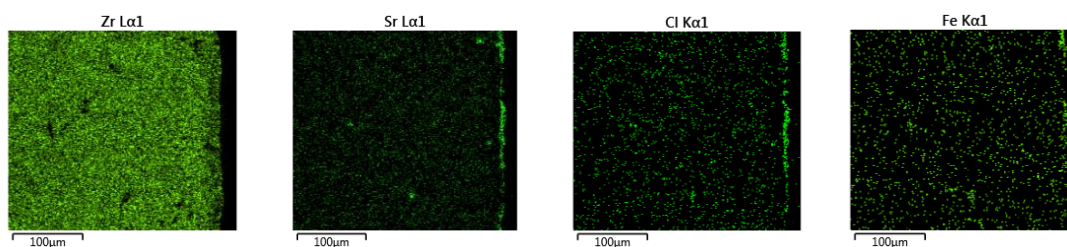


Figure A.10. Mapping analysis of the interface between  $\text{SrCl}_2 \cdot 6\text{H}_2\text{O} + \text{Fe}(\text{NO}_3)_3 \cdot 9\text{H}_2\text{O}$  mixture and zirconia pellets after heat treatment.

The mixture of  $\text{La}(\text{NO}_3)_3 \cdot 6\text{H}_2\text{O} + \text{SrCl}_2 \cdot 6\text{H}_2\text{O}$  was heated on top of zirconia. According to the EDS analysis, distribution ratio of La (0.01) was higher than Sr (0.00) into the substrate (Table 4.1) (Figure A.11 and A.12).

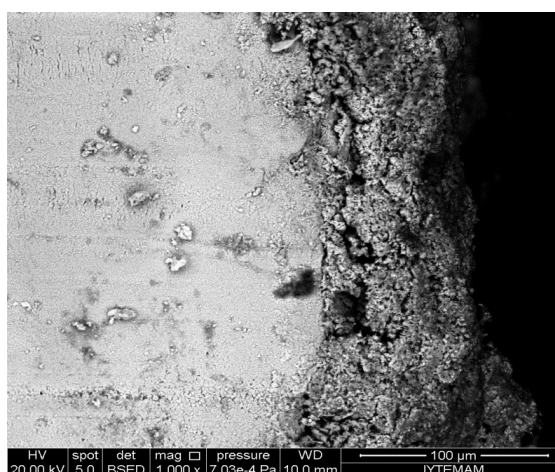


Figure A.11. SEM image of the interface between  $\text{La}(\text{NO}_3)_3 \cdot 6\text{H}_2\text{O} + \text{SrCl}_2 \cdot 6\text{H}_2\text{O}$  mixture and Zirconia pellets after heat treatment.

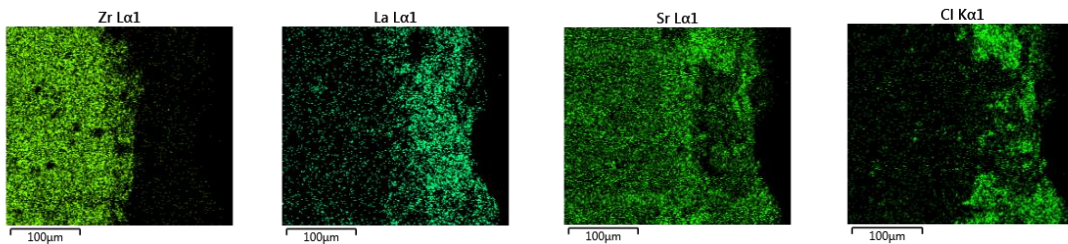


Figure A.12. Mapping analysis of interface between  $\text{La}(\text{NO}_3)_3 \cdot 6\text{H}_2\text{O} + \text{SrCl}_2 \cdot 6\text{H}_2\text{O}$  mixture and zirconia pellets after heat treatment.

The mixture of  $\text{La}(\text{NO}_3)_3 \cdot 6\text{H}_2\text{O} + \text{SrCl}_2 \cdot 6\text{H}_2\text{O} + \text{Fe}(\text{NO}_3)_3 \cdot 9\text{H}_2\text{O}$  (also coded as L+S+F) was heated on top of zirconia (Figure A.13 and A.14).

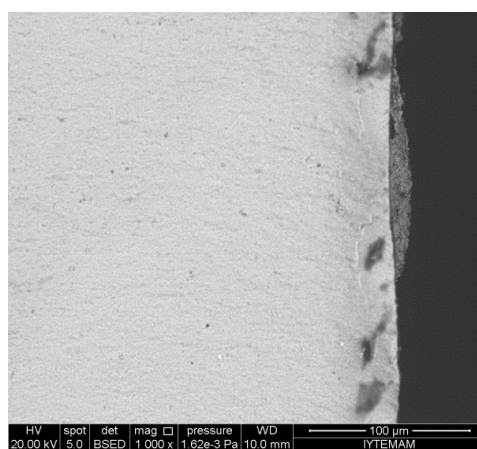


Figure A.13. SEM image of the interface between  $\text{La}(\text{NO}_3)_3 \cdot 6\text{H}_2\text{O} + \text{SrCl}_2 \cdot 6\text{H}_2\text{O} + \text{Fe}(\text{NO}_3)_2 \cdot 9\text{H}_2\text{O}$  mixture and Zirconia pellets after heat treatment.

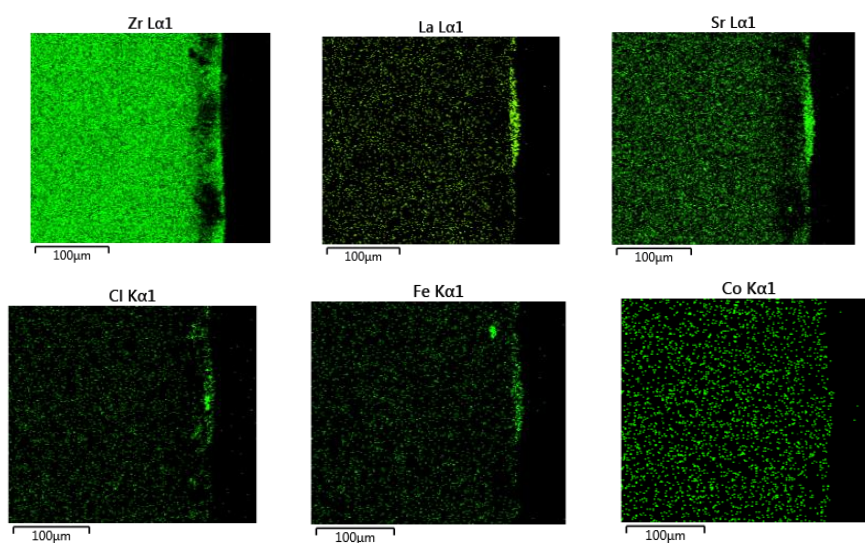


Figure A.14. Mapping analysis of interface between  $\text{La}(\text{NO}_3)_3 \cdot 6\text{H}_2\text{O} + \text{SrCl}_2 \cdot 6\text{H}_2\text{O} + \text{Fe}(\text{NO}_3)_2 \cdot 9\text{H}_2\text{O}$  mixture and zirconia pellets after heat treatment.

## APPENDIX B

### SEM-EDS RESULTS OF MIXTURES HEATED ON TOP OF CGO SUBSTRATE

Some results of experiments which are not given in Chapter 4 are given in this section of thesis.

The first pair studied was  $\text{La}(\text{NO}_3)_3 \cdot 6\text{H}_2\text{O} + \text{Co}(\text{NO}_3)_2 \cdot 6\text{H}_2\text{O}$  mixture (L+C) heated on top of CGO. The distribution ratio of La was higher than Co into the substrate (Figure B.1 and B.2).

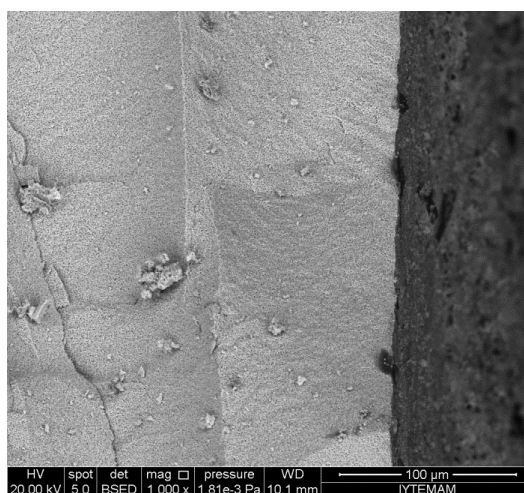


Figure B.1. SEM image of the interface between  $\text{La}(\text{NO}_3)_3 \cdot 6\text{H}_2\text{O} + \text{Co}(\text{NO}_3)_2 \cdot 6\text{H}_2\text{O}$  mixture and CGO pellets after heat treatment.

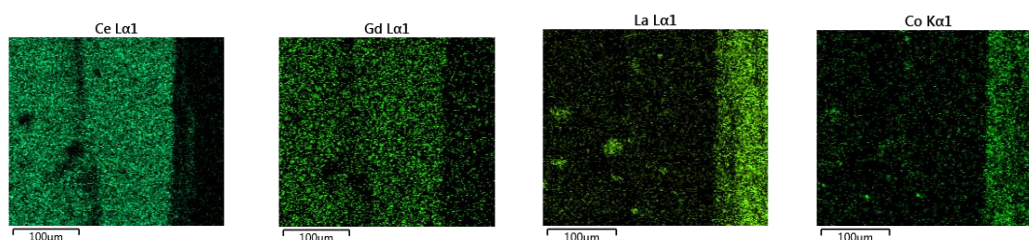


Figure B.2. Mapping analysis of the interface between  $\text{La}(\text{NO}_3)_3 \cdot 6\text{H}_2\text{O} + \text{Co}(\text{NO}_3)_2 \cdot 6\text{H}_2\text{O}$  mixture and CGO pellets after heat treatment.

The second pair studied was  $\text{SrCl}_2 \cdot 6\text{H}_2\text{O} + \text{Co}(\text{NO}_3)_2 \cdot 6\text{H}_2\text{O}$  (S+C) mixture heated on top of CGO (Figure B.3). Co ion diffuse meanwhile Sr had a quite low distribution ratio into the substrate (Table 4.2).

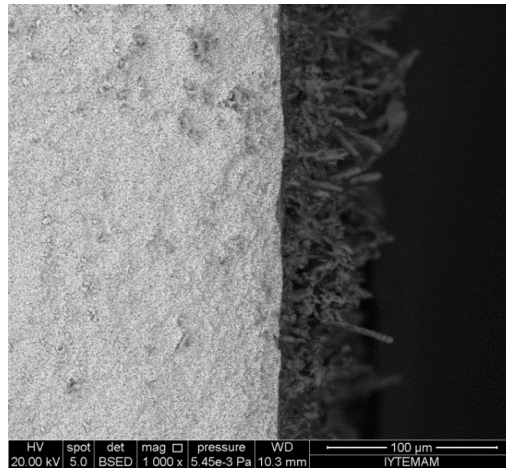


Figure B.3. SEM image of the interface between  $\text{SrCl}_2 \cdot 6\text{H}_2\text{O} + \text{Co}(\text{NO}_3)_2 \cdot 6\text{H}_2\text{O}$  mixture and CGO pellets after heat treatment.

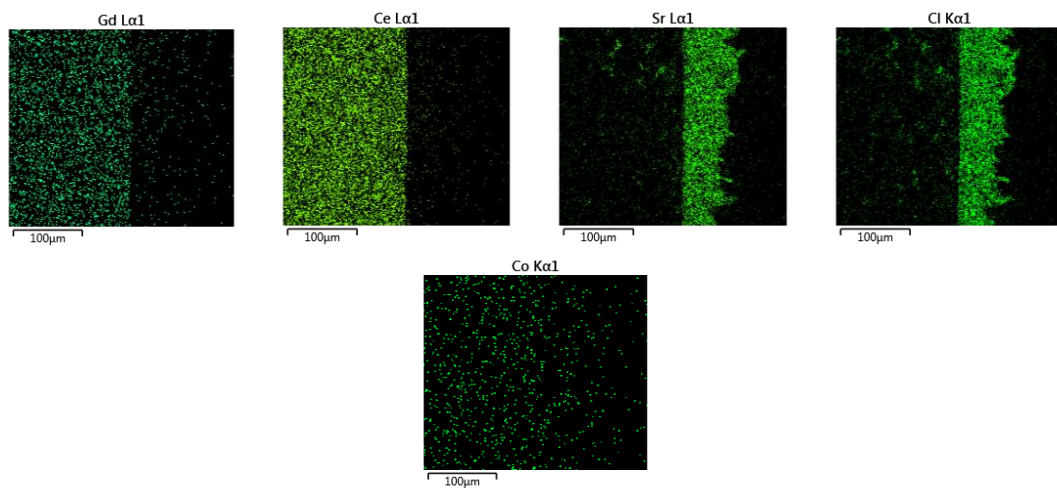


Figure B.4. Mapping analysis of the interface between  $\text{SrCl}_2 \cdot 6\text{H}_2\text{O} + \text{Co}(\text{NO}_3)_2 \cdot 6\text{H}_2\text{O}$  mixture and CGO pellets after heat treatment.

The third pair studied was  $\text{Co}(\text{NO}_3)_2 \cdot 6\text{H}_2\text{O} + \text{Fe}(\text{NO}_3)_3 \cdot 9\text{H}_2\text{O}$  (C+F) mixture heated on top of CGO (Figure B.5 and B.6). According to EDS analysis, even though Fe elements did not diffuse into the CGO substrate, Co elements significantly diffused into the CGO substrate (Table 4.2).

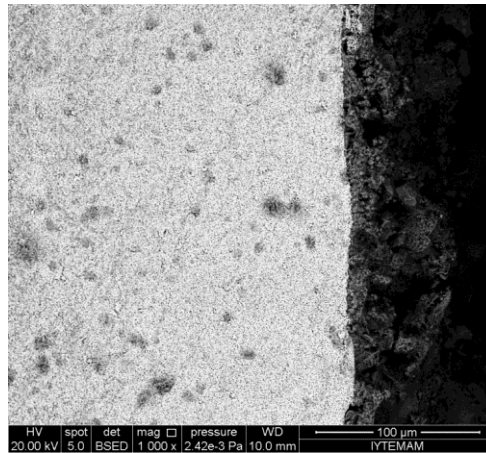


Figure B.5. SEM image of the interface between  $\text{Co}(\text{NO}_3)_2 \cdot 6\text{H}_2\text{O} + \text{Fe}(\text{NO}_3)_3 \cdot 9\text{H}_2\text{O}$  mixture and CGO pellets after heat treatment.

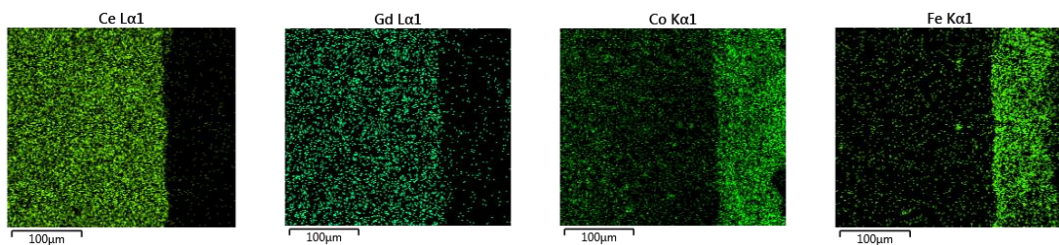


Figure B.6. Mapping analysis of the interface between  $\text{Co}(\text{NO}_3)_2 \cdot 6\text{H}_2\text{O} + \text{Fe}(\text{NO}_3)_3 \cdot 9\text{H}_2\text{O}$  mixture and CGO pellets after heat treatment.

The mixture of  $\text{La}(\text{NO}_3)_3 \cdot 6\text{H}_2\text{O} + \text{Fe}(\text{NO}_3)_3 \cdot 9\text{H}_2\text{O}$  (L+F) heated on top of CGO (Figure B.7 and B.8). There was no diffusion of La (0.00) and weak diffusion of Fe (0.01) elements from cathode layer into the substrate layer according to Table 4.2.

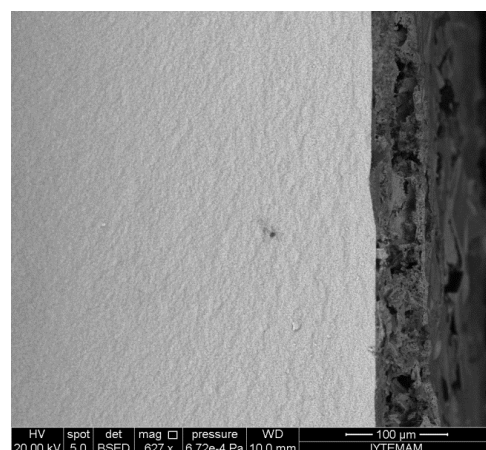


Figure B.7. SEM image of the interface between  $\text{La}(\text{NO}_3)_3 \cdot 6\text{H}_2\text{O} + \text{Fe}(\text{NO}_3)_3 \cdot 9\text{H}_2\text{O}$  mixture and CGO pellets after heat treatment.

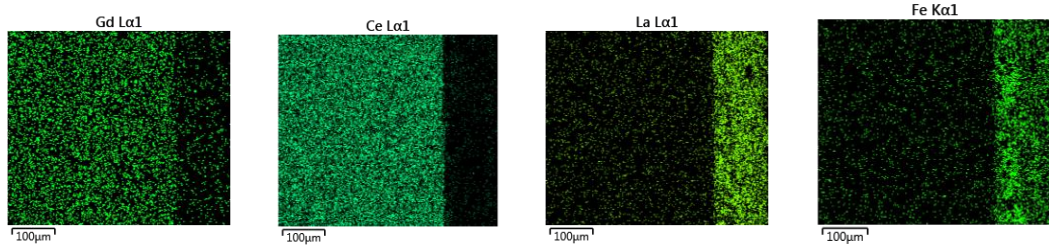


Figure B.8. Mapping analysis of the interface between  $\text{La}(\text{NO}_3)_3 \cdot 6\text{H}_2\text{O}$  +  $\text{Fe}(\text{NO}_3)_3 \cdot 9\text{H}_2\text{O}$  mixture and CGO pellets after heat treatment.

$\text{SrCl}_2 \cdot 6\text{H}_2\text{O} + \text{Fe}(\text{NO}_3)_3 \cdot 9\text{H}_2\text{O}$  mixture heated on top of CGO. Distribution ratio of Sr (0.06) and Fe (0.07) was close to each other (Table 4.2 and Figure B.9).

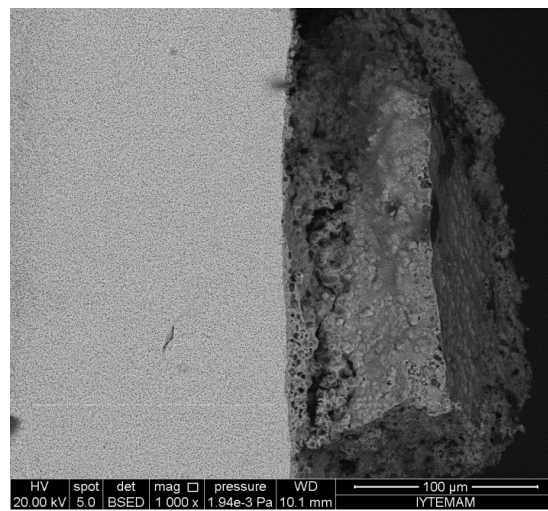


Figure B.9. SEM image of the interface between  $\text{SrCl}_2 \cdot 6\text{H}_2\text{O}$  +  $\text{Fe}(\text{NO}_3)_3 \cdot 9\text{H}_2\text{O}$  mixture and CGO pellets after heat treatment.

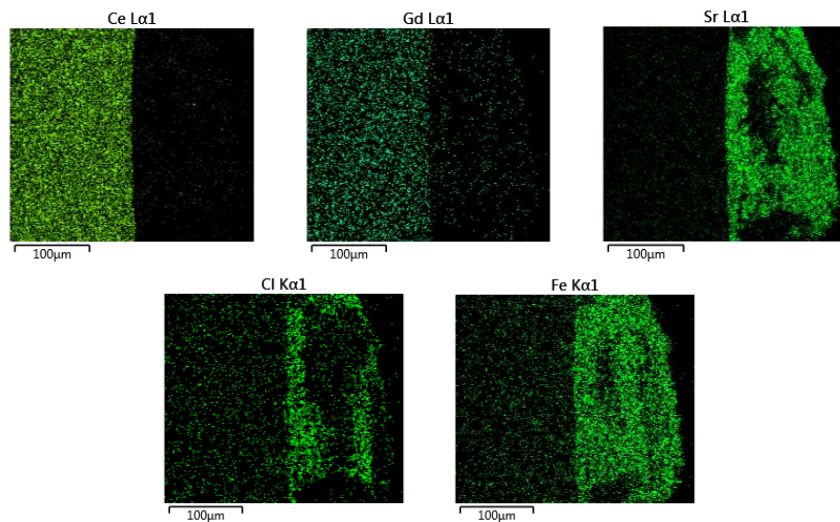


Figure B.10. Mapping analysis of the interface between  $\text{SrCl}_2 \cdot 6\text{H}_2\text{O}$  +  $\text{Fe}(\text{NO}_3)_3 \cdot 9\text{H}_2\text{O}$  mixture and CGO pellets after heat treatment.

The mixture of  $\text{SrCl}_2 \cdot 6\text{H}_2\text{O} + \text{Co}(\text{NO}_3)_2 \cdot 6\text{H}_2\text{O} + \text{Fe}(\text{NO}_3)_3 \cdot 9\text{H}_2\text{O}$  heated on top of CGO. Distribution ratio of Fe (0.03) and Co (0.03) into the substrate were higher than Sr (0.02) in Table 4.2 (Figure B.11 and B.12).

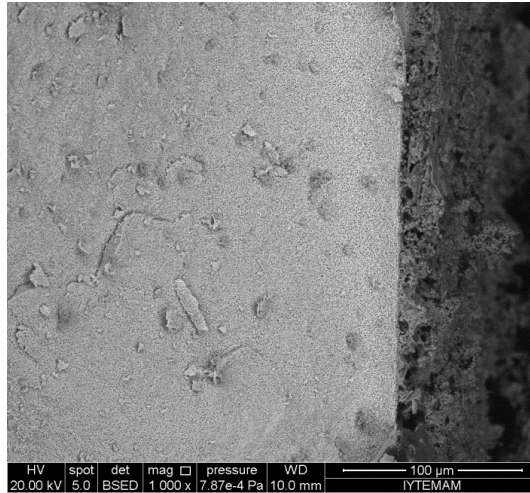


Figure B.11. SEM image of the interface between  $\text{SrCl}_2 \cdot 6\text{H}_2\text{O} + \text{Co}(\text{NO}_3)_2 \cdot 6\text{H}_2\text{O} + \text{Fe}(\text{NO}_3)_3 \cdot 9\text{H}_2\text{O}$  mixture and CGO pellets after heat treatment.

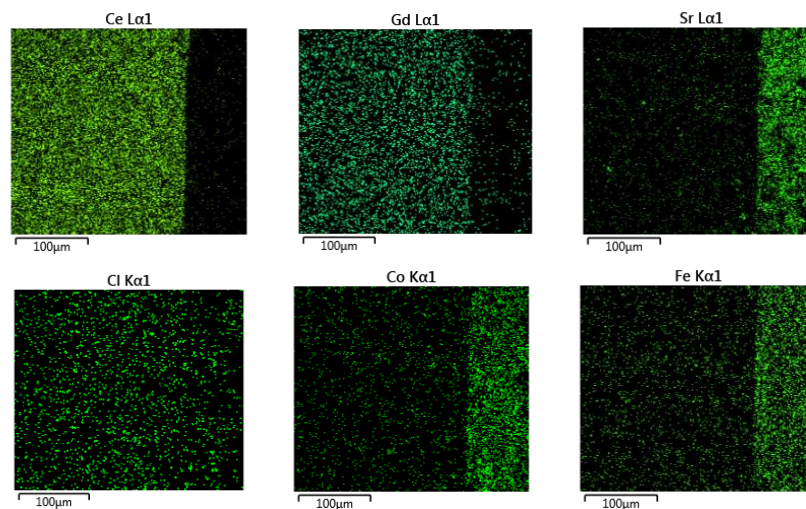


Figure B.12. Mapping analysis of the interface between  $\text{SrCl}_2 \cdot 6\text{H}_2\text{O} + \text{Co}(\text{NO}_3)_2 \cdot 6\text{H}_2\text{O} + \text{Fe}(\text{NO}_3)_3 \cdot 9\text{H}_2\text{O}$  mixture and CGO pellets after heat treatment.